DESIGN FOR RELIABILITY IN MICROOPTELECTROMECHANICAL SYSTEMS (MOEMS)

by

ABIODUN ADEKUNLE FASORO

Presented to the Faculty of the Graduate School of

The University of Texas at Arlington in Partial Fulfillment

of the Requirements

for the Degree of

DOCTOR OF PHILOSOPHY

THE UNIVERSITY OF TEXAS AT ARLINGTON

MAY 2008

Àwá yín Ọ

ACKNOWLEDGEMENTS

Just like man's journey through life, all journeys, short or long, start with a step and surely come to an end someday! The euphoria of celebrating the end of the journey, we often lose sight of things that are important. One thing that we should never forget to do is to express gratitude to those that made the journey a possible. As the African proverb goes, it takes a village to raise a child! I am indeed grateful to many people that I have had the honor of being associated with over the years. First and foremost, I would like to thank my dissertation supervising professor, Prof. Dan Popa who has been a mentor, model and constant source of inspiration to me. I thank you for the moral and financial support of the past three years. Likewise, I thank Prof. Dereje Agonafer most especially for his financial support during the early part of my program as well as his advice and encouragements throughout my program. I also want to thank my committee members, Prof. Kent Lawrence, Prof. A Haji-Shiehk and Prof. Tory Chen for their guidance and support towards the completion of this dissertation. My appreciation also goes to Prof. Harry Stephanou, the director of the Automation & Robotics Research Institute (ARRI) for the financial support of his Institute from January 2005 till the end of my program and also for creating at ARRI, an environment that is highly conducive for first class and cutting edge research.

I owe a special note of gratitude to the past and present students, faculties and staff of ARRI. The students helped create a fun and exciting place for all and I wish to

thank the members of the Next Generation Systems (NGS) Research Group at ARRI especially, Rakesh, Aditya, Jartuwat, and Muhammad as well as other graduate students working at ARRI including Mohammad Mayyas, Praveen, Smitha, Peter, Rachita and others. You all succeeded in making my stay at ARRI a most enjoyable one and for that, I am grateful. I am also grateful to past and current students and staff of the Electronics MEMS & Nanoelectronics Systems Packaging Center (EMNSPC) including M Hossain, A. Patil, Abhijit, Nikhil, Mullay, and Sakeet. I also thank Woo Ho, Jeongsik, Mason, Eileen, Raul and Heather. These are ARRI faculty members that I had turned to at one time or the other for advice, suggestions, or assistance. My time at ARRI has been wonderful because of the efforts and love from many ARRI staff including Kathleen, Norm, Ricky, Sara, Dana, and Jessica. I mostly want to thank Ricky for being such a wonderful person and a source of inspiration. My day at ARRI is hardly made without seeing Ricky. By his actions and attitude, he constantly reminds me of the two earliest lessons from my dad; first, there is dignity in labor and secondly, what ever you do, do it well.

Words cannot adequately express the depth of my appreciation to my family. I am blessed with a loving, caring and supportive family. I thank my lovely wife, Lanre who has been with me through thick and thin. In spite of your busy schedule yourself you took care of me, Olu, and Lolade. I really appreciate you. I also thank Oluwaponmile, my son. You are a constant reminder of me. Thank you Olu for being a wonderful brother to your little sister, Lolade. I thank my parents for raising a wonderful son in me. I also thank my siblings (Layo, Funke, Segun, Yemisi, Bimpe,

and Ayo) and their families for their love at all times. Finally, I will like to express my gratitude to my uncles Bodunde and Ayodele for their support, and advise at various times.

December 11, 2007

ABSTRACT

DESIGN FOR RELIABILITY IN MICROOPTELECTROMECHANICAL SYSTEMS (MOEMS)

Abiodun Adekunle Fasoro, Ph.D.

The University of Texas at Arlington, 2008

Supervising Professor: Dan O. Popa

Microelectromechanical systems (MEMS) is an enabling technology for miniaturization. MEMS consist of micron-size moving mechanical structures and electronics fabricated on a suitable substrate such as silicon. MEMS has found applications in virtually every aspect of human life, ranging from the automobile to the aerospace, and from the telecommunications to the consumer electronic industries.

Technology integration has led to several subsets of MEMS e.g. microoptoelectromechanical systems (MOEMS), radio-frequency MEMS (RF MEMS), etc. Together with these added functionalities, by way of technology integration come

additional issues and challenges never before experienced by packaging engineers. MEMS and MOEMS package requirements vary widely with the application, but they generally involve protecting the device from the damaging effects of the environment, such as moisture, dust, vibrations or thermal shock.

In this dissertation, we applied Design for Reliability (DfR) principles to MOEMS packaging especially at the process development stage of product actualization. DfR provides a unique approach to MOEMS packaging with reliability as the focal point. Such an approach is desirable for several reasons. First, it reduces the cost and time for product development by departing from the "build-test-rebuild" approach. Secondly, it provides better understanding of the process input-output relationship, so the practitioner is better able to make informed design decisions. Lastly, it can lead to enhanced product quality, performance and reliability.

The DfR framework for MEMS packaging was demonstrated in demanding applications consisting of two MEMS based optical switches and a micropump for implantable drug delivery. The reliability requirement for the optical switches are stringent - namely, a shelf-life of 25 years or more, hermetic sealing through the use of metal seals, and no organic compounds inside the package. The reliability requirement for the micropump is also stringent: efficient dissipation of heat for implantation inside the human body, no fluidic leaks, and the use of biocompatible packaging materials.

In the case of the optical switches, numerical simulation and experiments were used systematically in order to guide the process design for the different packaging processes discussed in this dissertation. These processes include fluxless die-to-carrier

attachment, optical fiber-to-carrier attachment, and hermetic lid sealing. Results show that our approach is very helpful in determining adequate process windows using only a small number of reliability experiments, leading to a shorter production development cycle for the MOEMS devices.

In the case of the micropump, numerical simulation and experiments were used systematically in order to guide the package design. We show that packaging greatly influences the performance of the micropump, and therefore design optimization is necessary. A reduced order model for the micropump and package was created, and was found to be accurate enough to capture the heat dissipation trends in the micropump within a 6% error from a Finite Elements baseline model. However, it only requires fraction of simulation time compared to the full fledged FEA analysis. Using this model, we modified the package materials and geometry in order to ensure a safe operating temperature for the micropump implanted in the human body. Our approach can be used for the analysis of packaged electrothermal MEMS actuators in general.

TABLE OF CONTENTS

LIST OF ILLUSTRATIONS

LIST OF TABLES

CHAPTER 1

INTRODUCTION

1.1 Overview of MEMS

Microelectromechanical systems (MEMS) consist of micron-size moving mechanical structures and electronics that may be used for sensing or actuation. MEMS employ novel microfabrication technologies such as photolithography, etching and release techniques to form tiny structures on a substrate material such as silicon. Most of these processes are adapted from and are similar to those used in the "already established" semiconductor industry. The past two decades has witnessed tremendous growth in MEMS technology and this growth is expected to continue for the foreseeable future. The growth of MEMS may be attributed in part to the extensive knowledge base on semiconductor fabrication processes, the development of new and novel processes, its potential for miniaturization, and the massive funding into MEMS research.

According to Bogue [1], one of the publications that paved the way for the emergence of MEMS is a 1960 publication titled "Piezoresistance Effect in Germanium and Silicon," [2] in which the author described certain stress sensitive effect in silicon and germanium. The effect described in the paper is known as piezoresistance which is the changing electrical resistance of a material due to applied mechanical stress

[3]. Micromanufacturing technology history dates back to the mid 1960s to the early 1970s with a number of concepts currently used in micro-manufacturing such as high resolution positional feedback and differential thermal expansion being originally precision engineering concepts [4].

Although the use of the acronym MEMS was formally coined less than twenty years ago [5], most of the essential microfabrication technologies behind MEMS such as lithography and etching have been in use for a much longer time. MEMS as we know it today has graduated from laboratory curiosity and ideas to an exciting research field and it has been described as an enabling technology for miniaturization leading to microsystems that impact us in so many ways [6-14].

An example of a MEMS device is the Digital Micromirror Device ™ (DMD) developed at Texas Instruments [15]. The DMD™ consists of micromirrors fabricated from aluminum. Figure 1.1a shows an array of micromirrors while Figure 1.1b is a close-up of two of these micromirrors. The micromirrors in Figure 1.1b are shown semi-transparent in order to make the structures below the micromirrors visible. The DMD™ is a highly sophisticated optical switching device consisting of up to two million tiny hinged reflective micromirrors. Each of these tiny micromirrors (size: 16 μm x 16 μm) has an underlying memory cell that controls the mirror's orientation or state via electrostatic attraction force due to potential difference between the mirror and the memory cell [15]. The ON state for each mirror corresponds to $+10^{o}$ mirror orientation while the OFF state corresponds to -10^{o} orientation as shown in Figure 1.1b. The primary application of the DMD™ is to digitize light as in the Digital Light

Processing™ (DLP) technology for projectors. The DLP™ consists of a light source, optics, color filters, digital processing and formatting, a DMD, and a projection lens [16]. The DLP™ technology makes possible, high quality digital gray scale and color reproduction [17]. Yet, even though the DLP™ has been a huge commercial success, its development cycle spanned nearly 20 years from concept to production, and it required overcoming many challenges related to hermetic sealing and reliability.

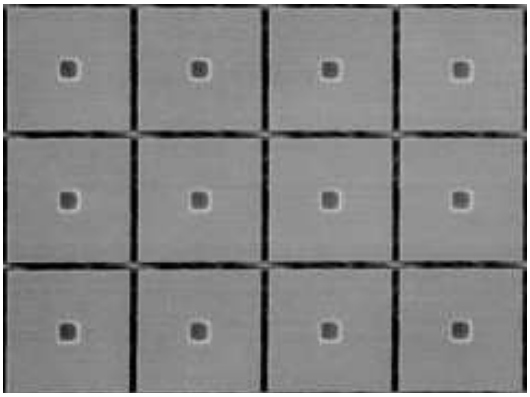

(a)

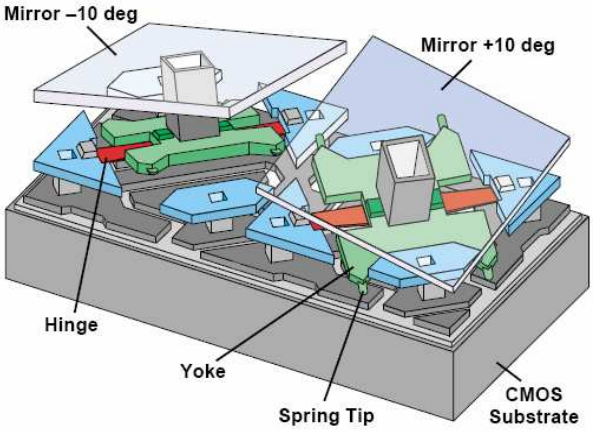

(b)

Figure 1.1 Texas Instrument's Digital Micromirror Device™ showing (a) array of micromirrors and (b) two semi-transparent DMD pixels [16].

As an enabling technology, MEMS has facilitated the development of other technologies that would otherwise have been difficult, impossible or impractical to achieve at the length scale predicted by MEMS. MEMS also offer a high level of technology integration such as radio frequency (RF), optical, and bio-MEMS and herein lies one of its greatest attractions.

One important characteristic of MEMS is the ease with which optics can be integrated into MEMS. The importance of the resulting technology i.e. microoptoelectromechanical systems (MOEMS), sometimes referred to as optical MEMS, continues to be on the rise due to the enhanced capabilities and potentials offered by the integration of optics. These enhanced capabilities enable the generation, transmission, guidance, and detection of light for information processing [9, 18] with applications that includes optical switches and projection. Wu [19] describes optics as an ideal application domain for MEMS technology because they are easier to actuate relative to other macro-scale objects.

A key aspect of MEMS and MOEMS is miniaturization. In fact, many people are unable to see MEMS as anything more than a way to miniaturize things. One of the reasons for the seeming attraction to MEMS is the ability to produce components at small length scales. Producing components at small length scales leads to reduced weight that makes high operating frequencies possible. This has led to substantial interests in MEMS based high speed switching devices. Of course, the advantages to miniaturizing are immense, including savings in materials, cost, size, footprint, etc., but

as noted by Kim et. al. [20], in addition to these drivers, the development of novel optics enabled functionalities is a key factor for the commercial success of MOEMS.

1.2 Applications of MEMS

As a result of the advantages of MEMS (e.g. miniaturization potential, material and cost savings, enhanced performance, etc.), there has been steady increase in research efforts into MEMS development as witnessed by the many MEMS based devices we interact with daily. MEMS technology can be found in many devices ranging from airbag deployment sensors used in automobiles, to microactuators for micropumps used in implantable drug delivery systems, primarily for sensing and actuation purposes. One would expect MEMS to continue to feature more and more in everyday devices as we continue to break packaging and reliability barriers to the commercialization of MEMS. The major application areas of MEMS include:

- Automotive
- Biomedical/health care
- Aerospace
- Communications

1.2.1 Automotive

The automobile industry is one of the major application areas for MEMS based devices. As today's automobile become "smarter" by way of electronic sensing and monitoring gadgets, MEMS technology feature prominently in many of these devices, leading to better consumer experience. As shown in Figure 1.2, today's modern automobiles are equipped with many MEMS sensors (e.g. tire pressure, oil level, fuel

pump pressure and fuel injection control, microaccelerometers used in air bag deployment systems, gyroscopes for navigation, etc.). The extremely hostile environment of the automobile (high underhood and exhaust temperatures, vibrations due to road conditions, etc.) presents formidable barrier to the use of MEMS in the automobile. Most of these issues are addresses and mitigated through novel packaging schemes.

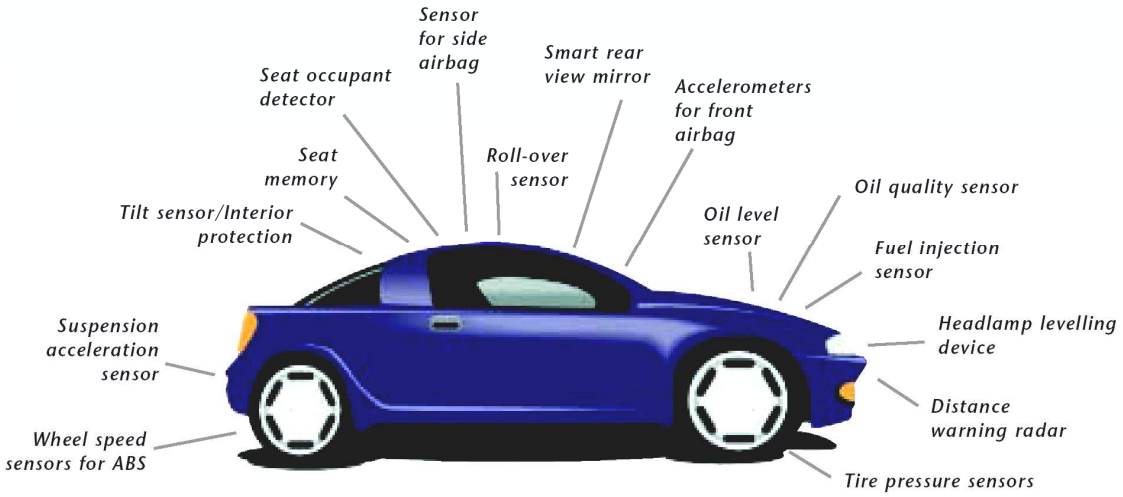

Figure 1.2 Sensors for various applications in today's automobile [21].

1.2.2 Biomedical/Health Care

MEMS technology has also found useful application in biomedical and healthcare industry. As focus in the medical community continues to shift towards better quality of human life, MEMS will continue to play prominent role in medicine. An example of MEMS based medical devices is the EndoSure Wireless AAA Pressure Measurement System developed by CardioMEMS. This implantable medical device is

shown in Figure 1.3. It measures blood pressure in people with abdominal aortic aneurysm [22].

Other examples of MEMS based medical devices include disposable blood pressure transducer (DPT), intrauterine pressure sensor (IUP), implantable drug delivery systems (IDDS) for diabetes and cancer treatments, etc. [23]. A crucial aspect of MEMS based implantable medical devices is the provision of appropriate device packaging that assures biocompatibility with the body, hermetic sealing, enhanced device performance and reliability. The package should also provide adequate and reliable system power.

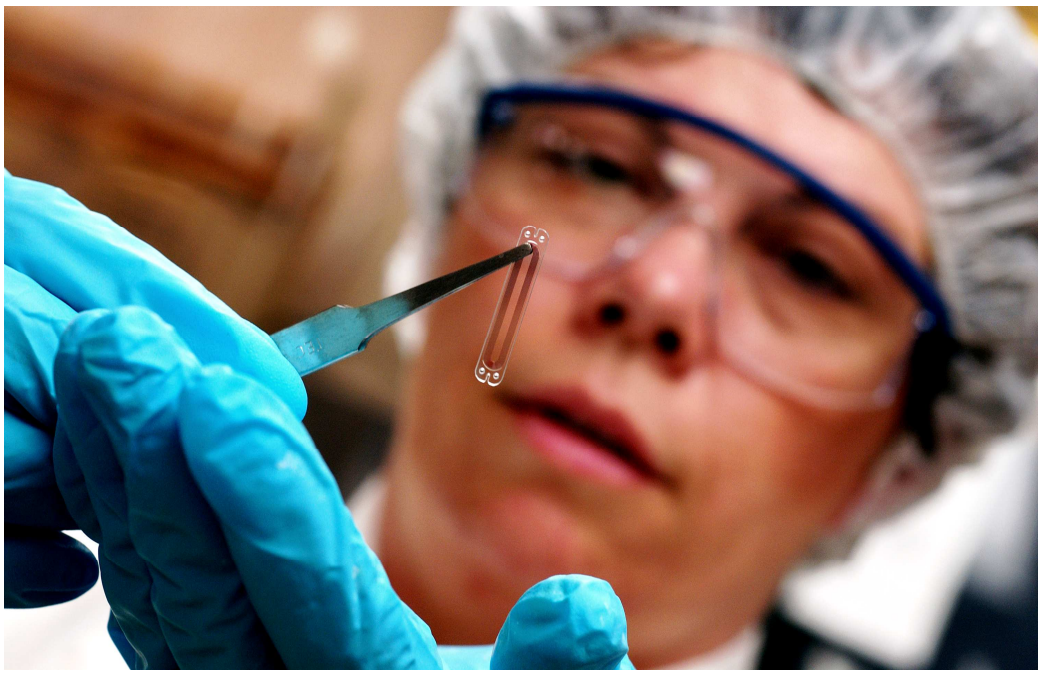

Figure 1.3 The EndoSure Wireless AAA Pressure Measurement System used for measuring blood pressure in people with abdominal aortic aneurysm [22].

1.2.3 Aerospace

Sensors and Actuators are used extensively in aerospace vehicles for gathering information about altitude, speed, cabin and tire pressure, temperature, fuel consumption and quantity, outside environmental conditions, etc. Figure 1.4 shows a commercially available MEMS based pressure measuring instrument manufactured by BF Goodrich Company. This device is used in an aircraft and offers about a quarter of the size and weight of similar non-MEMS based devices which is attractive for aerospace applications [24].

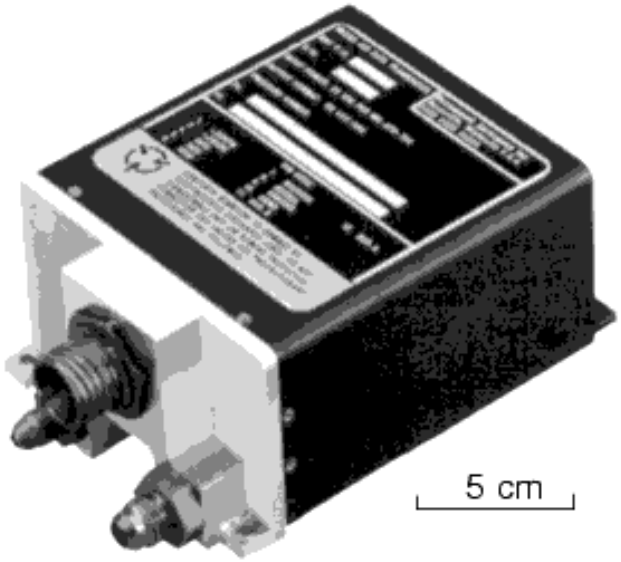

Figure 1.4 Commercially available MEMS based Micro-Air Data Transducer used in an aircraft [24].

1.2.4 Communications

MEMS have found great use in the telecommunications industry as optical switches, fiber optic components, and resonators. The small length scales achievable

through MEMS technology coupled with ability to produce small displacements at high frequencies makes them ideally suited for micromechanical and optical switches, tunable capacitors, and RF resonators. A major driver for the interest in optical MEMS is the increasing growth of communications traffic, with optical fiber communications providing the highest communication capacity [25].

1.3 Motivation for this Thesis and Problem Statement

Many of our critical use devices such as the air bag crash sensor, implantable medical drug delivery systems for diabetes and cancer treatments, and optical switching devices used by the military are now based on MEMS technology. This trend is expected to continue as we continue to gain better understanding of MEMS packaging and reliability. However, we realize that reliability presents a major challenge to the development of MEMS [26, 27].

Traditionally, reliability is not considered upfront during product development phase of MEMS. Instead, it is assessed using life tests, accelerated tests and other techniques after a product is manufactured [28]. By so doing, rather than designing for reliability, we are mostly characterizing or qualifying the product to ensure that it meets criteria based on some agreed standards.

More recently, reliability is being treated as a performance characteristic and current attitude is to design for reliability as you would other performance characteristics. Some of the skills and knowledge necessary for achieving reliable products includes statistical analysis, reliability predictions, engineering based physics of failure, failure modes/effects/criticality analysis, and failure analysis [29-30].

The goal of design for reliability (*DfR*) is to be proactive by introducing reliability early in product development, so that reliability concerns are identified and their effects are assessed starting from the conception stage to product obsolescence [31-32]. By so doing, aside from the more obvious advantage of addressing reliability concerns at the early stages of product development, we will be better able to understand how and to what extent both controllable and uncontrollable factors affect the reliability of products or systems. *DfR* can be used to predict reliability (e.g. by fitting life models) and also to design a robust system or process in the presence of environmental factors that promotes failure.

There is limited information in the literature on the application of *DfR* to MEMS and MOEMS packaging process development. One reason for this is the fact that MEMS is still an emerging technology that is yet to fully mature. Also, many companies involved in MEMS packaging consider their processes as trade secrets which are not to be shared willingly.

As a result of the low- to medium-volumes order usually encountered in many MEMS application areas, traditional packaging process development methods do not directly apply. In standard semiconductor or integrated circuits (IC) industry, the large-volume order justifies committing large resources (time, effort, samples, etc) to studying packaging process development and reliability. As a result, a MEMS packaging process development is often lacking, while process parameter settings are arrived at mostly by trial and error until acceptable results are obtained. One reason for

this approach is the absence of basic understanding about these processes, as they cannot be described by mechanistic models that engineers are so often accustomed to.

Later in this dissertation, using an implantable micropump as an example, we discuss the use of reduced order modeling and FEA model approximations as an aid to MEMS package design. We found this useful in the analysis of complex multiphysics (e.g. coupled electrothermomechanical) problems at the device level involving structures at different length scales. For these set of problems, analytic solutions do not exist, making numerical approximations attractive.

We summarize the problem statement for this research work by posing the following questions:

- Considering that a huge subset of MEMS devices requires low to medium volume orders rather than large volumes typical of the IC industry, how can we minimize the resources devoted to process development through experimentation and simulation while at the same time, extracting as much information as we can about the process? We conjectured early on in this thesis work that it should be possible to systematically reduce development time and materials cost for MOEMS, while at the same time, enhance yield and reliability.
- Design for reliability (DfR) has been used by many in the past to enhance the reliability of many products. Enhanced reliability is desirable for MOEMS especially those that requires extended shelf life. Can we implement the use of DfR framework in MOEMS packaging?

- Another problem that is addressed in this thesis is the use of numerical simulation as an aid in process design for determining suitable values for process parameters in packaging processes (e.g. in determining laser heating requirements for laser soldering). Can we use such simulation models that are experimentally validated to optimize package design or process parameters?
- Lastly, the detailed analysis of MEMS packages is difficult due to the different length scales of parts (for instance, μm size oxide layer and cm size metal or ceramic carriers), and also due the multiphysics nature of the analysis. The use of full fledged or detailed FEA models incorporating coupled field analysis is usually expensive and sometimes, impractical when the goal is to use simulation for design. Can we build simpler, yet accurate reduced order models to tune package parameters efficiently?

1.4 Contributions

In today's highly competitive market place where high emphasis is placed on reliability and cost effectiveness, MEMS and MOEMS packaging strategies needs to be carefully evaluated. This dissertation will present arguments for MEMS and MOEMS process development with enhanced product reliability, involving resource planning and allocation while utilizing minimum number of samples for process and product development processes. This is important for the following reasons: MEMS reliability is regarded as a major deciding factor with regards to the commercial success or viability of a product. We therefore need a framework or methodology through which we can build reliability into our products right from the product conceptualization stage,

thereby eliminating the costly "build-test-rebuild" approach used conventionally. Furthermore, because of the small batch order typical of many MEMS devices as well as the high costs of MOEMS components, it is difficult to commit a lot of experimental resources for MOEMS packaging process development.

The following is a summary of research activities undertaken during this dissertation:

- The determination of the process windows for different process parameters (or factors) necessary for packaging a MEMS based optical switching device. The packaging of this optical switch consists of challenging processes such as optical fiber-to-carrier attachment, MEMS die-to-carrier attachment, and lid sealing. For instance, for the fluxless fiber-to-carrier attachment via indium solder, 20W laser power in nitrogen gas ambient environment with less than 250 parts per million (ppm) of oxygen was found to be adequate.

- The use of numerical simulation to determine the temperature distribution on carrier package due to laser heating. This thermal model was used to determine the time and heating duration requirement necessary for laser soldering. The model was also used to estimate the effect of carrier redesign (involving surface property and geometrical modifications) on the thermal dissipation of the package. The simulations reveal that it is impractical to perform soldering by shinning a diode laser directly on the original gold carrier surface.

- Tests to assess reliability of the packaging attachment processes have been performed. These include the fiber pull test, the die shear test, and the optical leak

test. The fiber pull test is used to assess the joint strength of the fiber-to-carrier attachment. This was done by constraining the movement of the carrier and pulling on the free end of the fiber until failure occurs. The average bond strength for the fiber pull test was 5.02MPa, which was adequate for the application.

- The development of compact or reduced order models for a MEMS based micropump. The micropump consists of parts that are of different length scales and different coupled physics (e.g. thermal and structural). Our approach in simplifying the problem was: (i) reduce the complexity of the model geometry, and (ii) decouple the physics of the problem. Results show that the package reduces the operating stroke of the pump by around 50%.

The contributions of this thesis to the existing body of knowledge in MEMS packaging were as follows:

- Novel fluxless soldering processes for the packaging of MEMS based optical switching device with expected long shelf life. These processes involved (i) the use of attachment materials that are amenable to fluxless soldering (e.g. indium solder and gold bearing solder alloys), (ii) the use of laser heating in order to localize the heating effect on the carrier, (iii) the use of an inert or reducing gas environment to slow down the growth of surface oxides during the soldering process, and (iv) the removal of preexisting surface oxides prior to commencing the soldering process. We determined optimum process parameters through a combination of experimentation and simulation.
- The redesign of appropriate metal carrier package for the optical switch. This design has the advantage of improved thermal dissipation during the packaging

process (fiber-to-carrier attachment) using laser energy. The improved thermal dissipation of the carrier results in lower laser heating power and reduced heating duration.

- Design for reliability (DfR) applied to MOEMS packaging. Simulations and experiments using statistical methods are used to develop package and processes that results in reliable MOEMS device that passed the MIL-STD 883 requirements for reliability.

- Validation of novel reduced order models for a MEMS-based implantable drug delivery system (micropump). This involves the use of compact modeling and decoupling of the physics of the device thus simplifying the problem. The loss of accuracy is less than 10% with one to two orders of magnitude reduction in the computational time. The model was used to determine the effect of packaging on the device operation and to ensure that the critical requirement for implanting this device (outer carrier temperature no more than 4 ^{o}C above normal human body temperature) is achieved. The modeling insight can be applied to the analysis of packaged thermal MEMS actuators in general.

1.5 Dissertation Outline

This dissertation consists of nine chapters. The organization of this dissertation is as follows:

Chapter 1 provides an overview of MEMS including a brief history of MEMS. This chapter also presents the major application areas of MEMS such as telecommunications and aerospace, together with examples of typical application

devices for each of these application areas. Design for reliability concepts are also introduced in this chapter. The chapter ends with statements on the motivation, importance, and the contributions of this dissertation to the body of knowledge.

Chapters 2 through 4 presents background information from the literature on MEMS fabrication, packaging, and reliability. Chapter 2 starts with a brief introduction to MEMS and MOEMS packaging including a comparison of semiconductor packaging and MEMS packaging, the hierarchy, and the role/function of MEMS packaging at each hierarchy level. Other topics presented in this chapter include MEMS packaging materials and the properties that make them suitable for MEMS packaging, as well as issues and challenges in MEMS packaging. The chapter ends with an overview of current trends and developments in MEMS packaging such as 3D and wafer-level packaging.

Chapter 3 presents an overview of the classification of MEMS microfabrication techniques such as surface and bulk micromachining methods. These are mainly front-end microfabrication processes like dry and wet etching, photolithography, oxidation, etc. This chapter also presents pertinent information on current practices in MEMS fabrications involving both front- and back-end packaging processes. The chapter also addresses the use of design of experiments and other statistical methods in developing MEMS packaging processes. The fabrication of the MEMS dies used as test vehicles in this research work were mostly performed at the University of Texas at Arlington's NanoFab and Stanford's NanoFabrication facilities.

In Chapter 4, we relate reliability to MEMS, emphasizing how packaging affects reliability. We also discuss the major MEMS failure modes and mechanisms (e.g. stiction, fatigue and material degradation) as well as some of the relevant test methods and procedure employed in assessing reliability for both product qualification (e.g. the MIL-STD 883F) and reliability modeling.

Chapter 5 presents a description of the proposed framework for applying design for reliability to MOEMS packaging as it applies to processes such as die attachment, wire bonding, and seam sealing.

Chapter 6 describes the application devices (MOEMS switches and implantable micropump) used as case studies for applying design for reliability to MEMS packaging as well as detailed descriptions of the packaging processes, process conditions and parameters used in the packaging activities and the reliability tests presented in this research work.

In Chapter 7, we present the results of finite element analysis (FEA) used to obtain estimates of processing parameters for fiber-to-carrier attachment. This attachment process was performed using laser soldering which is a contactless, localized heating method. FEA (using ANSYS®) was also used to obtain estimates of the laser absorption on gold surface. This value was used to calculate the amount of laser power for heating the carrier during the fiber attachment process. The results obtained from the FE analysis suggested that carrier geometrical and surface property modifications are necessary in order to increase laser absorption of the carrier. This chapter also presents the results obtained from the reduced order modeling of a

packaged implantable micropump for the controlled release of drugs. Using numerical simulations, we established that performance of the micropump's microactuator is affected by the package and also that the problem is simplified by using reduced order modeling without much loss in accuracy.

Chapter 8 presents the results of mechanical reliability tests carried out on our test vehicles. These tests include die shear test, fiber pull test, and hermetic tests.

The dissertation's conclusions and recommendations for future work are presented in Chapter 9.

CHAPTER 2

BACKGROUND: MEMS AND MOEMS PACKAGING

2.1 Introduction

MEMS has witnessed tremendous growth over the past two decades, evolving from a research topic to finding numerous commercial applications. MEMS technology has served as an avenue for adding value to existing technologies such as sensors, actuators and inkjet printer heads.

Some of the attractions to MEMS are derived from its ability to miniaturize components. Additionally, the ability to seamlessly integrate MEMS with CMOS means that MEMS devices are equipped with further functionalities. As consumer preferences continue to shift toward smaller form factors and extended functionalities, the need to integrate MEMS technology (e.g. RF-MEMS) in everyday devices such as cell phones increases as well. In spite of the boom in the demand for MEMS based devices, relatively little effort is being channeled into MEMS packaging and this explains why only a fraction of conceptualized MEMS devices eventually make it to the market.

The literature has enumerated how the packaging of MEMS and MOEMS products serves both as a barrier and a limiting factor to the full commercial exploitation of MEMS [33-35]. The cost of MEMS and MOEMS packaging is high, accounting for 30 to even 90% of the total device cost [35-38], depending on its

complexity and design requirements. MEMS and MOEMS packaging requirements, though often application specific [39-41], include protecting the device from the damaging effects of the environment such as moisture, dust and heat that could lead to performance degradation, stiction of moving parts, corrosion, or outright failure.

Some other requirements of MEMS packaging are: providing mechanical support and protection, and providing interconnection paths e.g. electrical, microfluidic, and optical. There is no single set of requirements for a package to meet but rather, each package is designed based on its unique usage environment, operational and application specifications [36].

2.2 Packaging Hierarchy

It is generally regarded that packaging is critical to the successful outcome of any MEMS product. To better understand packaging, we present a brief overview of MEMS packaging hierarchy and the role of packaging at each hierarchical level. This overview is presented because MEMS packaging functions typically are not the same at every level as will be discussed shortly.

The study of MEMS packaging cannot be complete without some mention of semiconductor packaging from which most of the ideas and techniques used for MEMS packaging are derived. Semiconductor (IC or microelectronics) packaging provides certain functions and roles depending on its hierarchy including:

- Providing mechanical support
- Providing electrical interconnection from one layer to the other
- Protecting the chip during processing, handling and operation
- Thermal management

- Providing power

The four main levels (or hierarchy) of packaging recognized in semiconductor packaging are shown in Figure 2.1 [9]. At the package first level (also called L1 or chip and module level), the silicon chips (with integrated circuit) are packaged into modules. At the package second level (L2), several modules (level 1 packages) are mounted and interconnected on a common (usually organic) substrate to form a printed circuit board (PCB). The assembly of several PCBs forms a level 3 package on the mother board, and the assembly of several level 3 packages forms the entire system (level 4). Another packaging level that is also recognized is the zero level packaging which consists of interconnection of transistors and gates to form the IC on the chip.

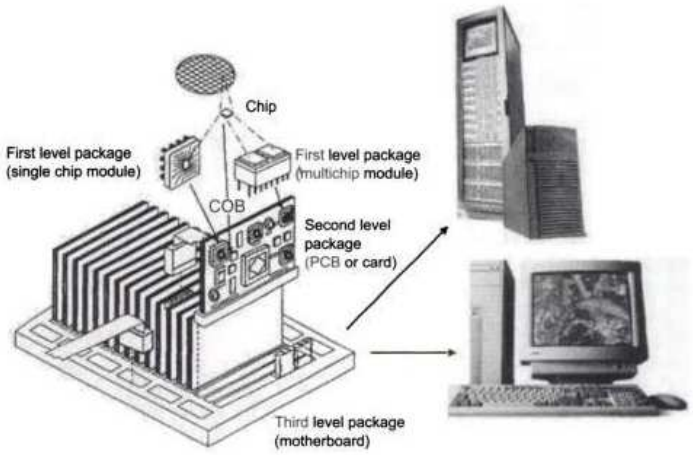

Figure 2.1 The four level hierarchal structure of semiconductor packaging [9].

MEMS packaging on the hand has a four level hierarchal structure: wafer level (L0), die level (L1), device level (L2), and system level (L3). Figure 2.2 illustrates the relationship between these three hierarchal levels. The die level package in MEMS

corresponds to level 1 and level 2 packaging of semiconductor ICs. System levels packaging in MEMS are similar to levels 3 and 4 semiconductor packaging. Unlike L1, L2 and L3, which are considered "back-end" packaging processes, the wafer level of packaging (level 0), is still part of the front-end manufacturing cycle. It consists of protecting the released MEMS devices by capping them with another wafer inside the fab cleanroom. Level 0 packaging is also slowly making its way into the IC industry, by allowing for vertical integration of semiconductor wafers using through-wafer electrical interconnects.

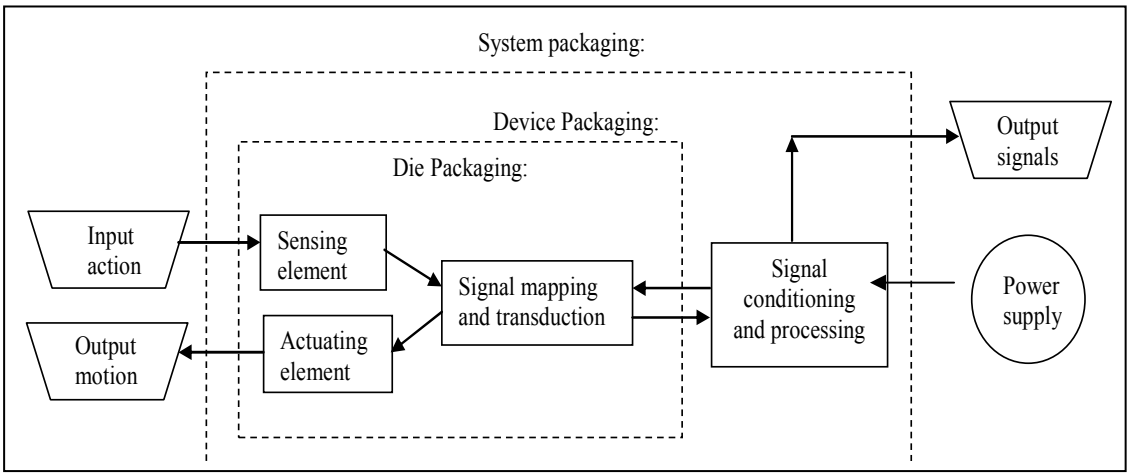

Figure 2.2 Three level hierarchal structure in MEMS packaging consisting of die, device and system level packing [42].

At the die level, the role of packaging includes [42]:

1. Protection of the MEMS die and the delicate mechanical microparts e.g. diaphragms and cantilevers.
2. Providing electrical and mechanical isolation for the MEMS microparts.
3. Providing interconnection using wire bonding or vertical via interconnects.

4. Packaging at this level also provides embedded sensing elements e.g. piezoresistors for the pressure sensor die as well as associated circuitry.

Figure 2.3 illustrates die level packaging for a MEMS based pressure sensor [42]. The sensor consists of silicon diaphragm for sensing, dies electric layer, piezoresistor, etc., housed in a metal carrier as shown in Figure 2.3a or encapsulated in plastic as shown in Figure 2.3b. This sensor has an opening through which pressurized medium is introduced. As shown in Figure 2.3a, the die attach is attached to the base material (Pyrex glass) to provide rigidity to the die by constraining it while electrical interconnection to the device level is obtained via wire bonding to the electrical feedthroughs.

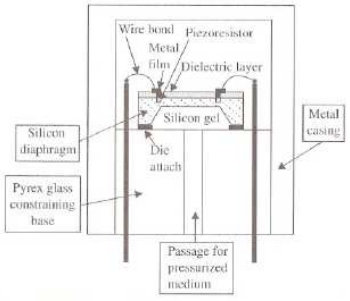

(a)

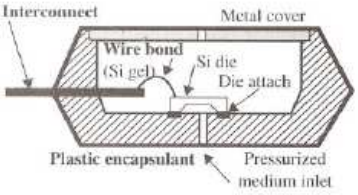

(b)

Figure 2.3 Die level packaging of pressure sensor (a) with metal casing, and (b) with plastic encapsulation [42].

At the device level, adequate signal conditioning and processing are provided. Also, provision is made for the interfacing of the MEMS die and the outside environment. Figure 2.4 illustrates the device level packaging of a micro inertial sensor [42] with two microaccelerometers for measuring in both the horizontal (x) and vertical (y) directions. We observe that both microaccelerometers share a common substrate with signal and processing units. The substrate size is about 3 x 2 mm^2. At the system level, packaging involves the interconnection of the die with primary signal circuitry. An example of system level packaging is shown in Figure 2.5 for a micro pressure sensor.

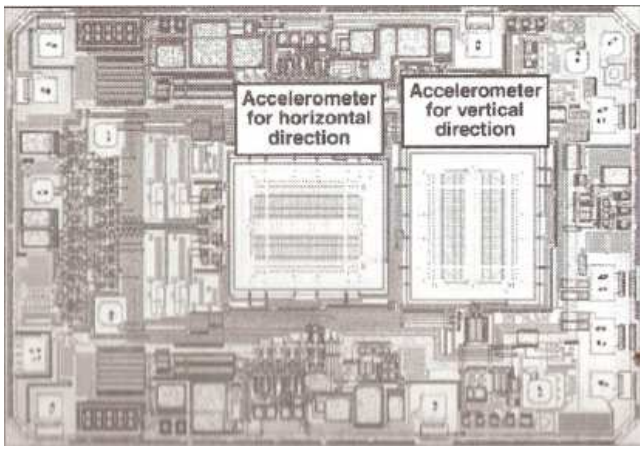

Figure 2.4 Device level packaging of Analog Device's inertia sensor [42].

2.3 IC Packaging vs. MEMS Packaging

Packaging is an essential aspect of both IC and MEMS product development. IC packaging and MEMS packaging share several attributes as is evident in the similarities between IC and MEMS packaging techniques and materials. In fact, most of the techniques for MEMS packaging such as die bonding, wire bonding, etc., are imported

from the acquired knowledge from the "more matured" IC packaging. Table 2.1 compares several attributes of IC and MEMS packaging. We observe from Table 2.1 that MEMS and IC share many packaging processes (e.g. die and wire bonding).

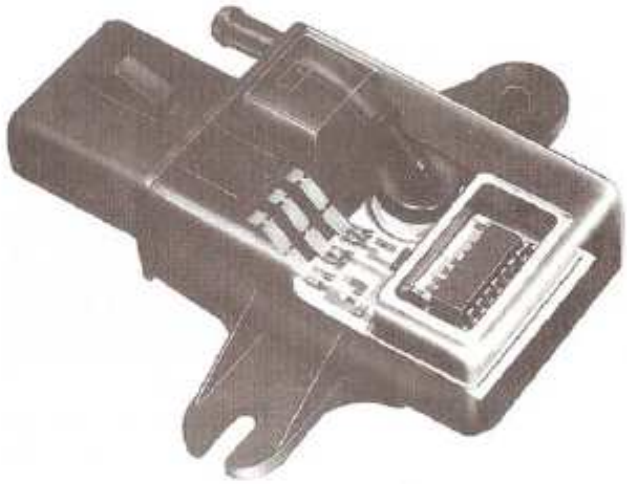

Figure 2.5 System level packaging of pressure sensor [42].

Table 2.1 Comparing IC and MEMS packaging [43].

	Item	IC Packaging	MEMS Packaging
1	Capping		✓
2	Dicing	✓	✓
3	Die Bonding	✓	✓
4	Wire Bonding	✓	✓
5	Pre-molding		✓
6	Post molding	✓	
7	Hermetic	✓	✓
8	Wafer Bonding		✓
9	Testing	✓	✓
10	Stiction	✓	✓
11	Reliability	✓	✓
12	Standard	✓	✓
13	Cost	✓	✓

Although MEMS packaging shares many attributes with conventional microelectronics packaging, it is nevertheless, different in several respects and is generally more complex. For instance, the use of high quality optical surfaces for MOEMS applications, such as the digital micromirror used in the DLP® technology, requires a hermetic seal and/or a use of getters to protect optical surfaces from contamination and degradation from moisture [44]. In addition to the complexity of MEMS packaging, the integration of optics with MEMS (e.g. the introduction of optical access requiring the use of anti-reflection coated window [45] or an optical waveguide transversing a leak tight boundary), adds another layer of complexity to MOEMS packaging.

The ability to seamlessly integrate different technologies such as optics, radio frequency, fluidic, biological, etc., is a key aspect of MEMS. This high level of integration presents packaging challenges in terms of communicating and interfacing with different media types. This contrasts with semiconductor packaging in which the communication mode with the outside is often only through electrical signals [46]. In the semiconductor industry, the integrated circuit (IC) chip is often encapsulated with an underfill material for mechanical reliability purpose [47-49]. However, in general, the use of underfill will not be appropriate in MEMS because of the need to interface with the environment and also the need for hermetic packaging which cannot be achieved using organic underfills.

2.4 MEMS Package Types

The MEMS package (carrier) serves several purposes including protecting the device from humidity and contaminations from the ambient. This is especially important

in optical MEMS, in which there are high quality optical surfaces that easily degrade in the presence of moisture. The package also provides a means of fixturing the MEMS die so it does not move. It also provides heat dissipation paths (if needed) as well as intra and inter level interconnection path. The choice of appropriate package type for MEMS is a critical step in MEMS packaging because of the need for adequate protection of the device. Typical package types include metal, ceramic, and plastic packages. These package types are discussed briefly below:

2.4.1 Metal Packages

Metal packages are good choice when hermetic sealing is required for the MEMS device because most metals are considered to be hermetic. Processing methods for metal packages includes machining, metal injection molding, and pressure casting. Examples of metal packages are shown in Figure 2.6 [50]. Both package types have electrical interconnection pins exiting the package. In Figure 2.6a, the pins exit the package from the bottom wall of the package while in Figure 2.6b, the pins exits through the side walls. Metal packages typically have low I/O counts. Metal feedthroughs (from the sides or from the bottom) are attached to the metal package via glass sealing.

Metal packages possess excellent heat removal properties due to typically high thermal conductivities. They also possess excellent electromagnetic radiation shielding, making them ideal for RF MEMS packaging [51]. The drawback to metal carriers for packaging of MEMS is the CTE differential between most metals and silicon. The two common metal alloys used extensively for MEMS packaging that has CTE values close to silicon are Kovar and Invar. In order to provide corrosion resistance to the metal

package and also to provide solderable surface for die attachment, metal packages are usually coated with a thin layer of gold.

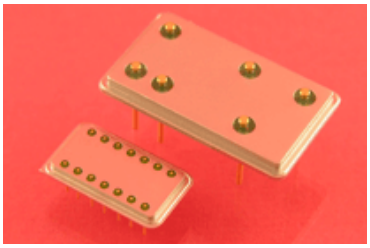

(a)

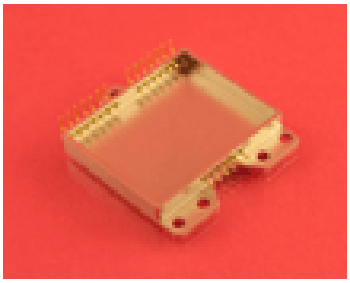

(b)

Figure 2.6 MEMS carrier with interconnection pins exiting the package from (a) bottom, and (b) sides [50].

2.4.2 Ceramic Packages

Ceramic packages are light weight, and relatively low cost packages capable of ensuring hermetic environments [52]. Two types of ceramic packages are co-fired and pressed ceramic packages. In co-fired ceramic packages, ceramic tapes (with cermet conductive ink patterns and printed-through vias) are stacked in layers such that the metalized layers are connected through the vias. These undergo a sintering process at elevated temperatures to produce a monolithic package. Several materials are available for co-fired ceramic packages (e.g. alumina). These are mixed with other materials (e.g.

binders, plasticizers, solvents, etc.) in specific proportions [52]. Co-fired ceramic packages with certain unique characteristics can be produced for desired purposes. Examples of Amkor's flat pack and ball array ceramic packages are shown in Figure 2.7 [53].

In pressed ceramic packages, mixture of ceramic and binders are molded into shape followed by sintering process at elevated temperatures. By sandwiching a metal leadframe between two sintered ceramics, a pressed ceramic package is obtained. The assembly is held together with glass frit at 400-460 ^{o}C to complete the process.

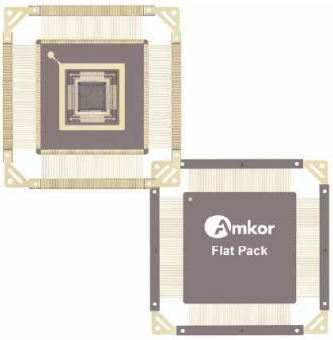

(a)

(b)

Figure 2.7 Amkor's ceramic packages: (a) Flat Pack and (b) Ball Array Ceramic [53].

2.4.3 Plastic Packages

Metal and ceramic packages are by far superior to plastic packages because the latter lack the hermetic capability of the former. Plastic packages are however desirable for packages that do not require full hermetic packaging or for low-cost prototypes. In addition to cost consideration, plastic packages are ideal where package weight is important as they generally weigh about half that of ceramic packages [54]. Plastic packages are categorized as pre-molded and post-molded. Pre-molded packages have a hollow cavity for the MEMS die and a lid for sealing as shown in Figure 2.8, while in post-molded package type, the die is first attached to the lead frame, followed by wire bonding. This assembly is then loaded into a mold cavity and then, the package body is molded on the assembly.

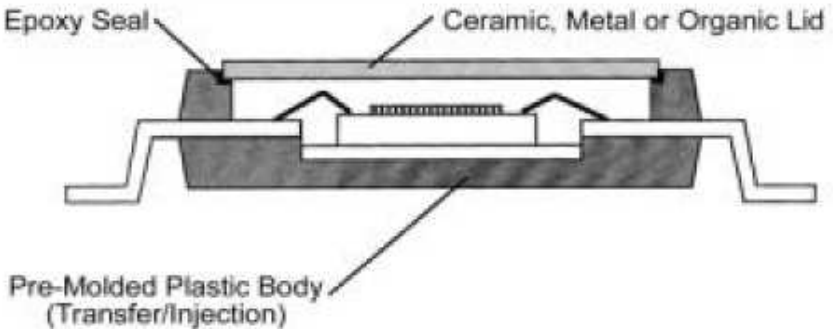

Figure 2.8 Pre-molded cavity package [55].

2.5 MEMS Packaging Materials

Materials always play central role in manufactured components and as fundamental research continue to provide basic information about materials, engineers continue to look for ways to develop novel “engineered” materials with desirable

properties for various applications including MEMS packaging. We are no longer limited to conventional materials as there is abundance of knowledge on how to develop materials with tailored (custom) properties so that their best attributes may be utilized.

By far, silicon remains the single most widely used substrate material in both the semiconductor and the MEMS industries. However, there are several other crystalline semiconductor materials available for use as substrate materials such as Ge and GaAs. In addition to MEMS substrate materials, other materials used for MEMS packaging include thin film materials (e.g. Au, SiO_2, Ni, Al, etc) serving as either conducting layers (e.g. Au) or insulating layers (e.g. SiO_2). Anti-stiction layers (e.g. polycrystalline silicon carbide) are also used for MEMS. Hsu [56] matched some common MEMS components (e.g. substrate, insulators, and interconnects) with frequently used materials for these components. A summary of these components vs. materials match is presented in Table 2.2. Though silicon is the most common material choice for die/substrate, we see from Table 2.2 that GaAs and other materials may be used for this purpose as well.

Table 2.2 Material choice for MEMS components (adapted from [56]).

Component	Material
Die/Substrate	Silicon, GaAs, polycryatalline silicon, cramics, quartz, polymers
Insulators	SiO2, Si3N4, quartz, polymers
Constraint base	Glass, quartz, alumina, silicon carbide
Die bonding	Solder alloys, epoxy resins, silicone rubber
Wire bonds	Gold, silver, copper, aluminum, tungsten
Interconnect pins	Copper and aluminum
Headers and casings	Plastic, aluminum, stainless steel

In the following sections, we discuss the properties of materials used for die and device level packaging. Examples of components used for die and device level packaging are includes the substrate, die attachment, interconnect, carrier, and lid. These are discussed briefly in the following sections.

2.5.1 Substrate Materials

MEMS substrate materials include silicon, gallium arsenide (GaAs), quartz, glass, and polymers. MEMS microfabrication processes takes place on the substrate material. In addition to this, it provides signal transduction, converting energy from one form to another. Because of the ability to change the electrical conductivity of semiconductor materials (e.g. by doping), they are commonly used as MEMS substrate materials. Silicon is the most widely used MEMS substrate material. The oxide of silicon is extremely stable and has high dielectric-strength suitable for insulation [57]. Silicon also has good thermal conductivity (124 – 148 W/mK) and excellent mechanical properties (flexural strength: 62 MPa, Modulus of elasticity: 109-190 GPa, poisson's ratio: 0.28, density: 2330kg/m^3).

2.5.2 Attachment Materials

MEMS die attachment materials are used to temporarily or permanently bond and secure the substrate in place during processing, storage, transportation, and operation. The bond strength of the die attachment material is critical in ensuring adequate fixturing of the substrate. Examples of MEMS die attachment materials are eutectic metal solders, glasses, and epoxies. The mechanical (e.g. shear strength, fatigue strength, creep properties, ageing behavior), thermal (e.g. melting point, curing temperature, and thermal

conductivity), and electrical (e.g. resistivity) properties of die attachment materials are important in choosing a die attachment material.

2.5.3 Electrical Interconnection

The provision of first and second-level interconnection paths is one of the essential functions of MEMS packaging. Several methods are available for these interconnections such as through wafer via, flip chip, and wire bonding to provide electrical connection between the bond pads on the MEMS die and the package. Wire bonding typically uses 25 micron diameter gold or aluminum wire. The two types of wire bonding available are ball and wedge bonding, with ball bonding accounting for about 90% of all bonds [57]. Ball bonding process consists of the following steps: formation of the first bond on the die; formation of wire loop; and, formation of second bond on the substrate. Figure 2.9 shows an example of stacked die with wire bond interconnects.

Figure 2.9 Forward ball bonding loops in stacked die applications [57].

2.5.4 Carrier and Lid Materials

The chip carrier and lid provides housing for the MEMS die, shielding it from contaminations e.g. dust and moisture. It also provides feedthroughs (electrical, optical, or fluidic). Lid-to-carrier sealing may be achieved using soldering, seam sealing, or glass. Lid and carrier materials should be similar in order to reduce the CTE mismatch between the two. The choice of carrier, lid and lid seal material determines the hermeticity of the package. Some factors to consider in choosing the seal material includes the permeability to moisture, mechanical properties, process temperature, CTE, and resistance to corrosion.

2.5.5 Capping

Wafer level chip scale packaging (WLCSP) makes use of capping methods to protect the MEMS device. Often, silicon is used as the capping material to ensure good CTE match between the die and the cap. MEMS capping presents a method by which hermetic packaging may be achieved at the die level. The MEMS die-to-cap sealing may be achieved using metal solder, glass frits, or epoxy materials. Other sealing methods used for MEMS die capping include anodic bonding, and direct silicon bonding. The cap die may simply serve as a dielectric cap in which case it does not contain MEMS structures or interconnects, or, it may be used for signal routing and electrical interconnection as illustrated in Figure 2.10.

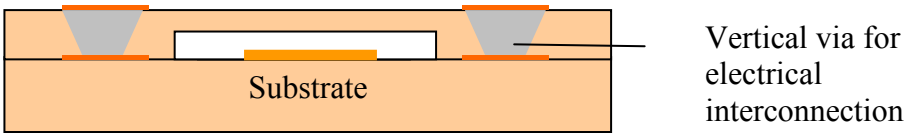

Figure 2.10 Capped MEMS die with vertical electrical interconnect via.

2.6 Fluxless Soldering

An appropriate packaging solution for a MEMS device should offer accurate component placement, attachment, sealing, protection and various interconnects, including electrical and optical [58-60]. MOEMS assemblies used for certain mission critical applications are expected to have long shelf lives and require hermetic sealing [61-63]. The package sealing can be obtained using a variety of materials including epoxies and solders [64]. However, the degradation and outgassing of organic materials such as those contained in fluxes and epoxies could result in the contamination and stiction of the moving microparts leading to reliability problems [61-66]. Because of the long shelf-life requirement for these devices, all attachment and sealing processes, such as MEMS die-to-package, fiber-to-die, glass cap-to-die, and fiber-to-carrier, must be done without the use of organic materials (e.g. fluxes and epoxies). Hence the need for fluxless attachment methods like fluxless soldering and seam sealing.

Fluxless soldering covers a broad range of techniques that either reduce the formation of surface oxides or prevent surface oxidation prior to and during the reflow process [67]. A necessary condition for successful fluxless soldering is the prevention of oxide formation or the removal of the oxide in a reducing environment throughout the reflow process. Fluxless soldering employs techniques such as controlled atmosphere soldering, thermo-mechanical surface activation and metallization [67]. Controlled atmosphere soldering is performed in a controlled environment such as vacuum, inert gas or reducing gas environment to prevent or reduce oxide formation on the solder and the substrate by excluding oxygen from the soldering environment. Furthermore, the presence of a reducing gas environment, e.g. hydrogen, helps to remove pre-existing

oxides by reducing the oxide to its native metal. An example of the thermo-mechanical surface activation is ultrasonic vibration, which provides a mechanism to mechanically remove surface oxides by cavitation and implosion [68]. The presence of high melting temperature oxides on solder and substrate surfaces inhibits wettability and prevents the solder from flowing. For MOEMS applications requiring hermetic sealing and reliable operation over 20 to 30 years period, fluxless soldering is desirable.

In addition to metal solder and epoxy, another material used for package sealing is solder glass [69-70]. However solder glass has the disadvantage of possessing poor mechanical shock and impact properties [71]. Also, the melting point for solder glass is typically high (above 350^{o}C) limiting its use in step soldering.

Reliable solder joints for MOEMS assemblies require that the surfaces to be joined be clean and free of multiple kinds of contaminations, mostly organics and oxides [72]. While it is usually easy to remove organics from the surface by using a solvent, it is more difficult to completely remove oxides from a surface. To remove the oxides, one needs to etch the surface in a chemical (etchant) long enough. However, if the surface is not immediately passivated and/or transferred into an oxygen free environment, a new layer of oxide will form on the surface in the presence of oxygen.

2.7 MEMS/MOEMS Package Design

Apart from the traditional functions of semiconductor packaging shared by MEMS packaging such as power and signal distribution, thermal management, and protection of the device from environmental influences [39, 73], they are expected to meet reliability criteria that would allow for enhanced device life under various envisaged working conditions based on the specific application needs and requirements.

MOEMS package design usually requires knowledge of electromechanical, thermomechanical, materials, fabrication, testing and assembly processes. Considerations for package requirements includes the die size, device working temperature range, device failure mode, the environment under which the device is to operate, mechanical robustness, thermal management, lead-free requirements, processing requirements, and costs [74]. MOEMS package design requires an understanding of the device, application and reliability requirements and is performed using experimental, numerical and analytical methods.

Though MEMS/MOEMS packaging is usually application specific, it is valuable to present details on some aspects of MEMS/MOEMS package design, such as mechanical and materials considerations. Mechanical considerations for MEMS/MOEMS package design include residual stresses both during device fabrication and operation. The residual stresses induced during fabrication can be addresses by the choice of materials and processing method while the induced stresses during operation is an important design factor that should be addressed via package optimization and choice of package materials. It is essential to ensure that induced stress levels during fabrication and operation are within levels that does not affect the package performance. Material selection is a critical aspect of MEMS/MOEMS package design. MEMS/MOEMS packaging materials includes the materials for the carrier, lid, metallization, wire bonding, and attachments.

The choice of packaging materials are influenced by the hermetic, stiction, and outgassing reliability requirements imposed on the package, as well as the thermomechanical properties of the material. The need for hermetic packaging usually

requires the use of a metal carrier and lid as well as the use of solder for the attachment processes rather that plastics and epoxies. Furthermore, it is essential that the choice of metal for the carrier be such that the CTE mismatch between the carrier and the MEMS die is minimal. Also, for long term reliability, it is essential to ensure that carrier does not form brittle or corrosion-prone intermetallics with the solder metal used for attachments. The low melting temperature and good fatigue properties of indium-based solder alloys for example, make them suitable for MEMS/MOEMS attachment processes.

2.8 Challenges in MEMS and MOEMS Packaging

2.8.1 General MEMS Packaging Requirements

MEMS and IC packaging share some basic roles such as mechanical protection and provision of electrical interconnection paths. The packaging of MEMS and IC's are however different in the sense that while MEMS typically have moving microparts, IC's do not. Therefore, MEMS packaging have to account for the packaging of these moving microparts or deflecting membranes. For instance, a MEMS device with moving microparts e.g. microresonator requires free-space environment. The performance of this device may be affected by air damping, making the need for vacuum and hermetic packaging design necessary.

Another requirement for MEMS packaging is to provide an environment that prevents the contamination of the MEMS device. Contamination may be in the form of dust from outside of the package, moisture ingress, particles from the degradation of packaging materials, residues from the decomposition of attachment materials, etc. Dust particles from the outside and particles from residues which are typically of similar size order as the MEMS structures may cause mechanical failure, while moisture ingress into

the package may lead to metal corrosion and stiction of moving microparts. Additionally, MOEMS devices often contain micromirrors and microlenses with high surface qualities which may be degraded by moisture inside the package.

MEMS packages unlike IC packages, often requires direct access to the outside environment. For instance, a MEMS device for gas pressure sensing may require a package that allows gas to enter and be sensed by a silicon micromachined diaphragm. At the same time, the packaging scheme should protect the diaphragm from damage from the high gas pressure. Therefore, the packaging in this case is expected to provide material sampling and force sensing capabilities. MEMS packages (especially those with applications in critical areas such as the automobile air bag deployment system) are expected to have high quality and reliability over the life of the device. The long term reliability of MEMS is not yet fully understood at this time.

The packaging of MEMS devices requiring stringent hermetic packaging poses big challenge to the packaging engineer. This is especially the case where interconnection paths (electrical, fluidic, optical, etc.) are required to cross sealed boundaries.

2.8.2 MOEMS Packaging Requirements

A unique feature of MOEMS is that signal transmission is optical in nature. This may be through optical transmission medium such as an optical fiber or sometimes, via free space. There are various application areas for MOEMS among which optical MEMS switches is one. In general, the key components of a MOEMS system consists of a light source (e.g. laser or LED), optical transmission medium (e.g. optical fiber or free space), optical elements (e.g. lenses), light detector (e.g. photocells), and coupling elements [75]. A common example of MOEMS device is optical MEMS switch which enable the

routing of optical data signals without the need for conversion to electrical signals [76]. Optical MEMS switch implementation can be classified as free-space or guide-wave [76-77]. In free space designs the moving structures i.e. mirror, grating beams, etc., interact with light in the free space propagation (radiation) mode [78], while in the case of wave-guide design, light is confined to optical waveguide [78], as shown in Figure 2.11a-b.

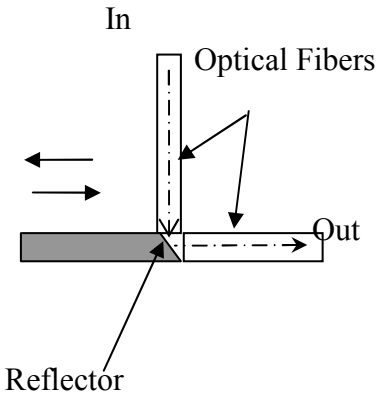

(a)

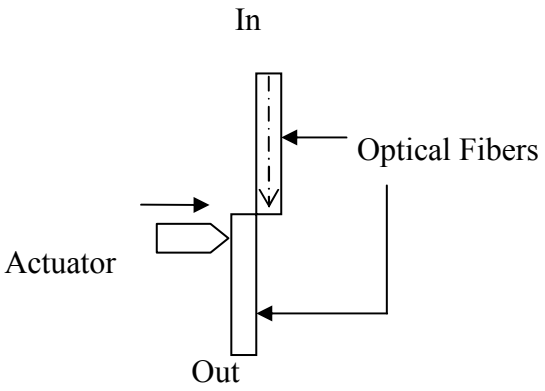

(b)

Figure 2.11 Schematics of (a) movable reflector and (b) movable waveguide optical switch.

One of the major challenges in MOEMS packaging is the requirement for hermeticity in the presence of signal lines/conduits such as optical fibers that pass through sealed boundaries. A hermetic environment that ensures vacuum environment and prevents mass transfer across a sealed boundary has been shown to impact mechanical reliability and performance (dynamic response) of MEMS devices, for instance microaccelerometer, microresonators, and RF-MEMS [79-83].

Another challenge in MEMS packaging relates to packaging materials and their properties such as the coefficient of thermal expansion (CTE). The choice of the substrate for instance should be such that the CTE is close to that of the die and the solder attach material in order to minimize stresses due to both local and global thermal mismatches. In addition, the processing steps for packaging should be compatible with the device intended. Other MOEMS packaging challenges includes stiction, corrosion, provision of a contamination free enclosure, and reliability enhancement.

2.9 Trends in MEMS Packaging

There is a certain general trend to the evolution of MEMS packaging driven in part by factors such as size, performance, weight, costs, materials, process compatibility, reliability, etc. Figure 2.12 [84] illustrates the evolution of MEMS packaging starting with the more conventional metal can and ceramic assemblies e.g. thin outline (TO) package, to novel thin film encapsulation and 3D packaging technologies. Today, the objective is no longer to obtain a “workable” package, but to use the package to enhance device yield, performance and reliability, reduce size, weight and costs.

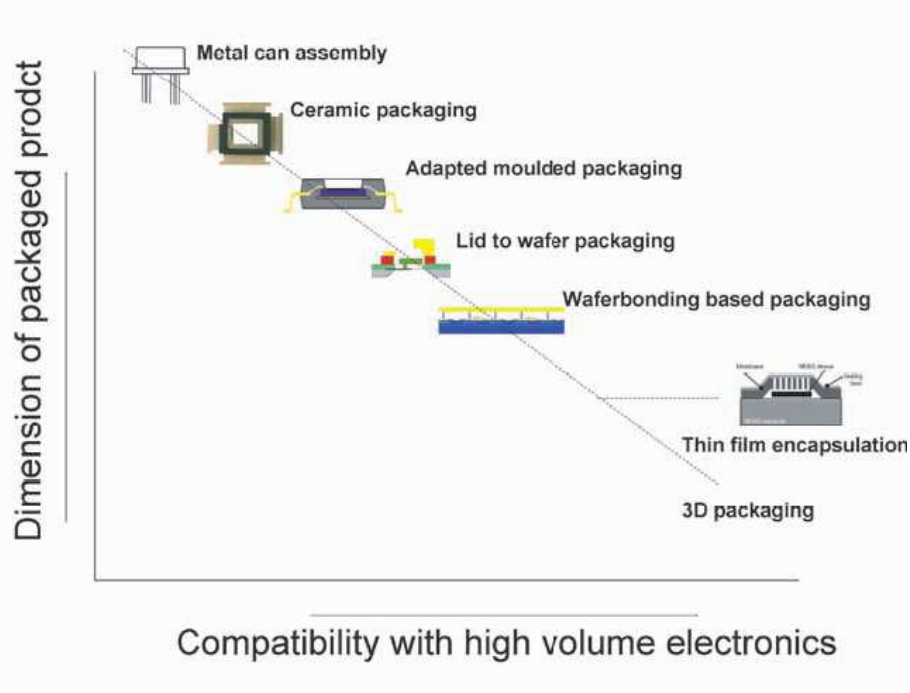

Figure 2.12 Evolution of MEMS packaging [84].

Metal can and ceramic packages are used when hermetic packaging is important such as for MOEMS. MEMS packaging in this case takes place at the back-end, involving assembly and attachment of device components via a die attach material using pick and place systems.

Wafer scale packaging is the case in which the wafer is covered before dicing to protect the MEMS device. All processing including level 1 electrical interconnection are done at the front-end prior to dicing. This packaging method requires wafer bonding technology such as anodic bonding to attach the cap wafer to the MEMS wafer.

The ability to fully integrate CMOS technology with MEMS, thereby enabling additional functionalities is one of the attractions to MEMS technology. This has resulted in hybrid MEMS in which the MEMS and CMOS are on separate dies and monolithic

integration in which both the MEMS and CMOS are on same die. 3D packaging is enabled through a hybrid concept whereby each die is stacked on top of each other using appropriate die bonding solutions.

CHAPTER 3

BACKGROUND: MEMS FABRICATION AND PACKAGING PROCESS DEVELOPMENT

3.1 MEMS Fabrication Methods

Many of MEMS fabrication processes (e.g. photolithography, thin film deposition, and bulk micromachining) are different from those used in conventional manufacturing in the "macro world" (e.g. milling, stamping, and casting). This is largely due to the small feature size of MEMS structures (typically micron size). Most MEMS fabrication processes can be classified as surface micromachining, bulk micromachining, or molding processes [85-86]. Other MEMS microfabrication processes include LIGA and laser micromachining. These MEMS fabrication processes make use of mechanical and chemical treatment of surfaces to produce desired microstructures. In the following sections, we briefly describe two of the common MEMS fabrication processes.

3.1.1 Bulk Micromachining

Bulk micromachining is a MEMS fabrication process that uses material removal processes to form desired three dimensional MEMS microstructures on the bulk substrate. The material removal process (or etching process) may involve the use of chemicals (e.g. diluted hydrofluoric, HF acid solution or potassium peroxide, KOH solution) or stream of positive-charge-carrying ions [87]. The former is

known as chemical or wet etching, while the latter is called dry or plasma etching. Chemical etching rates depends on the material to be etched, concentration of the etchant and temperature [86]. To perform the etching process, the substrate is covered at locations where etching is not desired with a material that is not affected by the etchant such as photoresist or SiO_2. In an actual etching process, after prolonged exposure to the etchant, the etchant attacks the substrate areas adjacent to the protective photoresist.

Unlike chemical etching that requires a liquid medium, dry etching does not involve the use of liquids. Rather, dry etching makes use of reactive gases at high temperature. Examples of dry etching methods include reactive ion etching (RIE), plasma and ion milling. In RIE etching process, several gases are introduced into a reactor and plasma is generated via an energy source such as radio-frequency (RF) source. The plasma breaks the gas molecules into ions which accelerate towards the material to be etched. These ions chemically react with the substrate to form a gaseous mater. Additionally, if the ions are energized enough, they will knock off atoms from the surface of the material to be etched without the previously explained chemical reaction taking place [88].

3.1.2 Surface Micromachining

While bulk micromachining is a subtractive process involving the removal of materials from the substrate to form 3D MEMS structures, surface micromachining on the other hand, is an additive process involving the addition of thin material layers forming structural or sacrificial layers. Surface micromachining consists of deposition and etching processes and a typical flow process is shown in Figure 3.1 [85], where

alternating layers of polysilicon, oxide, and aluminum are deposited, followed by patterning and etching of the poly layer and then deposition and etching of aluminum layer. Finally, the sacrificial oxide layer is removed to obtain the free standing structure shown in the figure.

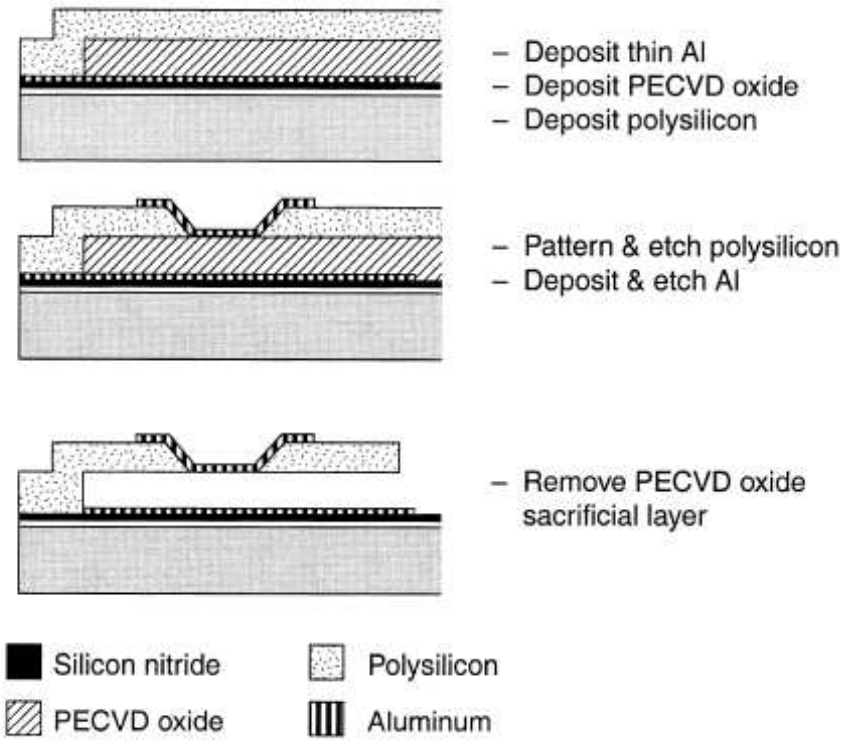

Figure 3.1 Typical process flow for surface micromachining [85].

3.2 Current Practices in Semiconductor and MEMS Manufacturing

Manufacturing is the process by which raw materials are transformed into finished products [89-90]. Manufacturing includes all intermediate processes involved in the finished product. In the semiconductor industry, the term "fabrication" is often

used in place of manufacturing [89]. Semiconductor fabrication consists of a number of process steps or sequence of processes (e.g. oxidation, photolithography, diffusion, etching, and deposition) that transforms a semiconductor wafer material such as silicon to an IC used in electronic devices.

Modern semiconductor manufacturing is a highly complex, volume-oriented process, consisting of hundreds of sequential individual processes that need to be executed almost perfectly as the yield at one stage will affect the overall yield attained. Semiconductor fabrication may be classified as front-end and back-end processes. As shown in Figure 3.2 [91], front-end fabrication processes are carried out in the Wafer Fab and they include oxidation, photolithography, etching, diffusion, ion implantation, and deposition processes for IC fabrication on the wafer.

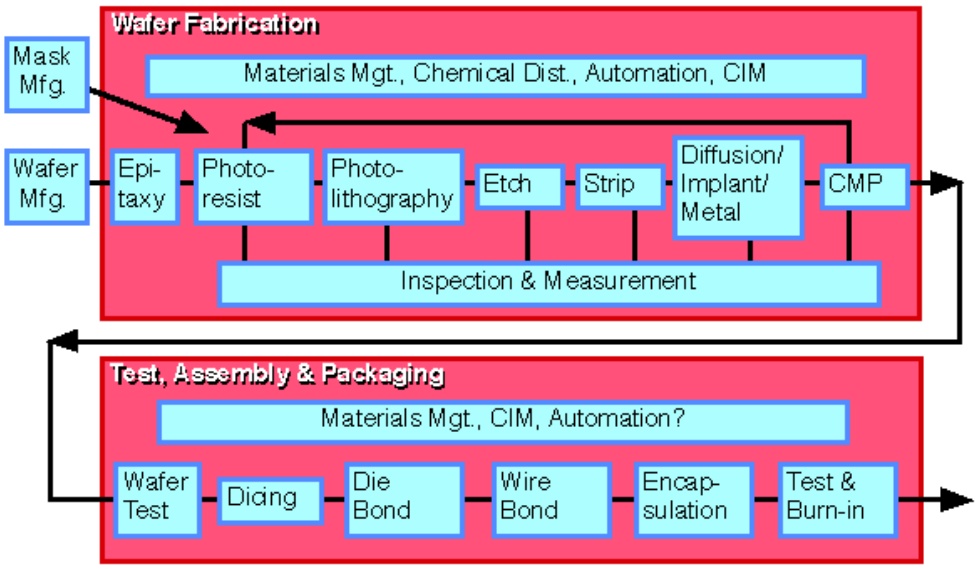

Figure 3.2 Chip making process consisting of front-end processes such as etching, diffusion, and epitaxy, and back-end processes such as dicing, die bonding and encapsulation [91].

Once the wafer fabrication process is complete, the wafers are diced into dies (or chips), assembled and packaged. The processes that take place after wafer fabrication are called back-end processes.

May [89] outlined three abstraction levels over which the semiconductor manufacturing process may be defined. The first level is referred to as unit processes which consist of inputs, outputs and specifications. These individual processes are linked together to form a process sequence. At various points on these links, we have inspection points from which information (measurements) are extracted in order to ensure product quality. On another abstraction level, we have information flow and utilization. The goal here is high yields, high quality, and low cycle time using Computer Integrated Manufacturing of Integrated Circuits (IC-CIM). The information obtained is used for equipment and process control. The last level of abstraction is process organization with the goal of maximizing product flow efficiency and yield.

In modern semiconductor manufacturing, inspection and testing are two key ingredients for ensuring high quality devices. Inspection and testing are done both on the wafer and the equipment used for the fabrication using statistical process control (SPC) methods. SPC is a collection of tools that are used to monitor manufacturing processes. One such tool is the control chart (also called the Shewhart control charts, named after Dr. Walter Shewhart that developed it) shown in Figure 3.3 [92]. It is used to detect variations in process performance. The control chart consists of a centerline representing the process mean, an upper control limit (UPL) and a lower control limit

(LCL). The process is said to be under statistical control when nearly all the sample points plots between the upper and lower control limits.

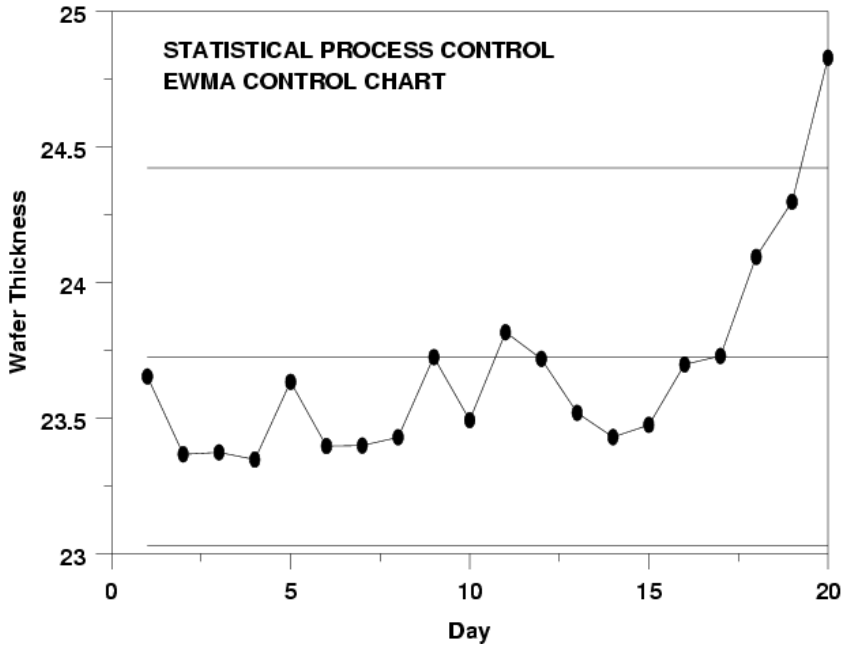

Figure 3.3 Example of a control chart for wafer thickness analysis [92].

The rest of this section is devoted to discussing the tools and methods for semiconductor fabrication. Our discussions on this subject will be limited to IC fabrication, design, and packaging. Several process simulators are available to describe fabrication processes such as ion implantation, annealing (diffusion and dopant activation), etching, deposition, oxidation, and epitaxy. These types of simulation tools are also called Process CAD. IC fabrication processes such as oxidation are well understood because the underlying physics is known. Silicon thermal oxidation for example can be represented as:

$$Si + O_2 \rightarrow SiO_2. \tag{3.1}$$

Using the Deal-Grove model, the time t required to grow an oxide film of thickness X_0 on a silicon surface at constant temperature is:

$$t = \frac{X_0^2}{B} + \frac{X_0}{B/A}. \tag{3.2}$$

Models such as this are solved using programs such as INTELLISENSE®, Stanford University Process Modeling (SUPREM) program, ATHENA, PROMIS, PREDICT, and PROSIM.

On the other hand, design tools such as Simulation Program with Integrated Circuit Emphasis (SPICE) are used to simulate electronic circuits. Front-end packaging design can be accomplished same time with the device design using process CAD tools. Back-end packaging however, typically make use of conventional CAD tools. The reliability of the back-end packaging process is later verified using various test methods. Because of the similarities in the front-end processing of ICs and MEMS, similar CAD tools are used for both.

Back-end packaging process developments of ICs rely more on time-consuming old fashion experimental procedures to empirically determine the process window and settings that ensures robust processes. This experimental approach based on DOE and other related topics are time consuming but is the only process development method available in certain circumstances. Through DOE principles, the resources employed can be reduced while the process is designed for robustness.

3.3 Design of Experiments in Process Development

3.3.1 Design of Experiments

Design of experiments (DOE) is a widely used technique in manufacturing, in which the factors affecting a response (or output) variable are systematically changed in order to measure the effects of these factors on the response variables. Examples of the application of DOE in both product and process improvement can be found in Condra [93]. DOE is especially useful in systems or processes where direct mathematical models (mechanistic models) are difficult or impossible to obtain. For such systems, the use of empirical models obtained using DOE is useful in understanding the behavior of the systems. Additionally, progress on the analysis of data obtained via DOE, e.g. Analysis of Variance (ANOVA) and Response Surface Methodology (RSM) has proved useful in interpreting the data obtained through DOE.

Montgomery [94-95] visualized manufacturing process as a combination of components, materials, people, equipment, processes and other resources that function collectively to transform a set of inputs into outputs described by one or more response variables as shown in Figure 3.4.

A statistically designed experiment can be used to achieve several goals including [94]:

- Finding the variable(s) that has statistically significant effects on the response output(s).
- Finding how to chose the values (level) of the input variables that achieves a desired response output value.

- Finding the level of input variables such that the effect of the uncontrollable variables on the response is minimized (robust design).

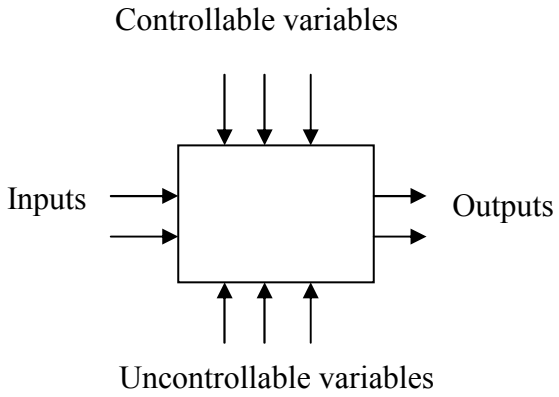

Figure 3.4 Input/output representation of a process.

3.3.2 Process Development Using Statistical Methods

Process development can be formally described in terms of determining factors that would affect measurable process response variables or quality characteristics of the process. The conventional method of doing this is called "one-factor-at-a-time" (OFAT) approach, in which each factor is varied at a time and its effect on the response is studied over a range of factor levels. Two drawbacks of OFAT are:

- The large number of resources that would be committed especially if there are numerous factors that potentially affects the response.
- The interaction effects of two or more factors cannot be estimated since only one factor is varied at a time.

3.3.2.1 Full Factorial Design

A method that would enable the estimation of two or higher factor interaction effects is full factorial, in which all possible factor combinations are used in the experiment. A 2^n full factorial can be modeled as:

$$E(y_{ij}) = \beta_0 + \beta_1 x_{i1} + \ldots + \beta_n x_{in} + \beta_{12} x_{i1} x_{i2} + \beta_{(n-1)n} x_{i(n-1)} x_{in} + \ldots$$
$$+ \cdots + \beta_{12\ldots n} x_{i1} \ldots x_{i(n-1)} x_{in} \qquad (3.3)$$
$$i = 1, \ldots, a; \quad j = 1, \ldots, b,$$

where (y_{ij}) is the j^{th} observation (j = 1, …, b) for the i^{th} treatment (i = 1, …, a) and the β's are unknown parameters defined such that β_0 is the general mean, β_1, β_2, …. β_n are the n main factor effects and β_{12}, β_{13}, β_{14}, …. , $\beta_{(n-1)n}$ are the two-factor interaction effects. A full factorial design described above potentially could require lot of resources (L^n experiments), where L is the number of factor levels (assumed to be same for all factors), and n is the number of factors.

3.3.2.2 Fractional Factorial Design

The full factorial design is not a realistic design for large values of n (even with L = 2) as the number of runs required increases exponentially. However, it is possible for us to select N treatments from L^n possible treatments that will estimate the factor effects with some degree of accuracy. This is called fractional factorial design and the degree to which we can accurately describe the factor main and interaction effects of course depends on the size of N. In a fractional factorial design, our treatment run is a fraction of the total L^n designs. If we are interested in the factor main effects and low-

order interactions effects (two-factor interactions), while assuming that high-order interactions effects (third order and higher) are negligible, our model reduces to:

$$E(y_{ij}) = \beta_0 + \beta_1 x_{i1} + \ldots + \beta_n x_{in} + \beta_{12} x_{i1} x_{2i} + \ldots \beta_{(n-1)n} x_{i(n-1)} x_{in} \qquad (3.4)$$
$$i = 1, \ldots, a; \quad j = 1, \ldots, b.$$

3.3.2.3 2-Level Fractional Factorial Design

The simplest form of factorial design is the two factor factorial design. Suppose we have two factors X and Y with *x* levels of factor X, *y* levels of factor Y, and *n* replications, then, the observed response when factor X is at the i^{th} level *(i=1,2,…,x)* and factor Y at the j^{th} level *(j=1,2,…,y)* for the k^{th} replicate *(k=1,2,…,n)* is y_{ijk}. The observations from this factorial design can be described using a linear statistical model in which the observed response assume a linear combination form of the model parameters. One such model that is commonly in use is the effects model described below:

$$y_{ijk} = \mu + \tau_i + \beta_j + (\tau\beta)_{ij} + \varepsilon_{ijk} \qquad (3.5)$$
$$\begin{Bmatrix} i = 1,2,..., x \\ j = 1,2,..., y \\ k = 1,2,..., n \end{Bmatrix}$$

In this model, μ is the overall mean effect, τ_i is the i^{th} level of factor X effect, β_j is the j^{th} level of factor Y effect, $(\tau\beta)_{ij}$ is the factors interaction effect, and ε_{ijk} is a random error component which includes all other sources of variability in the experiment such as the variability due to uncontrolled factors and background noise. In

the two factor factorial analysis, we could describe our problem in terms of determining the effect of say, factor X, factor Y, or the interaction effect of factors X and Y on the response. This would be equivalent to testing hypotheses regarding the factors main and interaction effects using the following statements:

$$H_0 : \tau_1 = \tau_2 = \cdots = \tau_x = 0 \qquad (3.6)$$
$$H_1 : at\ least\ one\ \tau_i \neq 0$$

$$H_0 : \beta_1 = \beta_2 = \cdots = \beta_y = 0 \qquad (3.7)$$
$$H_1 : at\ least\ one\ \beta_j \neq 0$$

$$H_0 : (\tau\beta)_{ij} = 0 \ \ for\ all\ i, j \qquad (3.8)$$
$$H_1 : at\ least\ one\ (\tau\beta)_{ij} \neq 0$$

3.3.2.4 ANOVA

If our factors (X and Y) are fixed, we readily apply statistical analysis of the fixed effect model and construct the analysis of variance (ANOVA) table to determine the main and interaction effects and then check for model adequacy using residual analysis. The ANOVA table is summarized in Montgomery [95] and the sums of squares presented below:

$$SS_T = \sum_{i=1}^{x}\sum_{j=1}^{y}\sum_{k=1}^{n} y_{ijk}^2 - \frac{y_{...}^2}{xyn} \qquad (3.9)$$

$$SS_X = \frac{1}{yn}\sum_{i=1}^{x} y_{i..}^2 - \frac{y_{...}^2}{xyn} \qquad (3.10)$$

$$SS_Y = \frac{1}{xn}\sum_{j=1}^{y} y_{.j.}^2 - \frac{y_{...}^2}{xyn} \tag{3.11}$$

$$SS_{XY} = \frac{1}{n}\sum_{i=1}^{x}\sum_{j=1}^{y} y_{ij.}^2 - \frac{y_{...}^2}{xyn} - SS_X - SS_Y \tag{3.12}$$

Where SS_T is total sum of squares, SS_X and SS_Y are the sums of squares of the main factors X and Y respectively, and SS_{XY} is the sum of squares of the interaction XY.

3.3.2.5 Screening Design

During the screening phase of experimental design process, factors that are known or thought to affect the response variable(s) of a process or system are identified and screened to determine their effects on the response variable(s). At this stage of the research, it is reasonable to identify many factors even though it is unlikely that all of these factors have significant effects on the response variable. A common principle that is adopted during the screening stage is that, in general, a large portion of the overall process variation is caused by a small portion of the process variables. This principle is also known as the Pareto or factor sparsity principle. The aim of the screening design therefore, is to identify the factors that have significant effects on the response variable.

Two level fractional factorial designs is a common experimental design used at the screening stage to determine which "few" experimental factors out of all the identified factors that have significant effects on the response variable. An advantage of screening design is that few experimental resources can be used to determine which variables have significant effects on the response variable. Therefore, screening designs

are often fractional, 2 level designs, encompassing the low to high regions of the process window for each factor.

3.3.2.6 Detailed Design

Once the factors that significantly affect the response variables have been identified, full factorial experiments may now be conducted on these few factors. It may be possible that one or more factors exhibit a quadratic effect which is not captured by a 2 level design. In such a case, a center point can be chosen for the factors and the design becomes a rotational or face-center composite design. Often times, experiments are unreplicated because of inadequate resources, leading to difficulties in interpreting the results obtained. If the design is unreplicated, we have no measure of the experimental error or variability in the process with respect to the factor effects, and it is difficult to conclude that a factor effect is significant. The analysis provided by Daniel [96] and others [97-98] provides a means of estimating the error in unreplicated experiments.

3.3.3 Regression Methods

It is often the case that several predictor variables (or process input factors) are related to the response variable (quality characteristic). Regression analysis provides an excellent technique for investigating and modeling the relationship between these predictor variables and the response variable. The use of regression analysis is widespread and it provides us with empirical models in complex and deterministic systems where exact and mechanistic models are difficult or impossible to attain. A linear regression model in which the response variable Y is modeled as a function of the regression coefficients (also called model parameters) $\beta_0, \beta_1, \beta_2, ..., \beta_k$ is represented as:

$$Y = \beta_0 + \beta_1 X_1 + \beta_2 X_2 + \cdots + \beta_k X_k + \varepsilon \,, \tag{3.13}$$

where $X_1, X_2, \ldots, X_k$ are the predictor variables. The regression problem essentially is that of finding the beta values that "best" satisfies the regression model. This is typically found using the least squares method – a technique that minimizes the sum of the squares of the errors, ε_i (of the model from the observed values) to obtain the beta values. If the i^{th} measurement is represented as:

$$y_i = \beta_0 + \beta_1 x_{i1} + \ldots\ldots \beta_k x_{ik} \tag{3.14}$$

The response equation can be represented in a matrix form as:

$$Y = X\beta, \tag{3.15}$$

where:

$$Y = \begin{bmatrix} y_1 \\ y_2 \\ . \\ . \\ y_n \end{bmatrix} \,, \tag{3.16}$$

$$X = \begin{bmatrix} 1 & x_{11} & x_{12} & \ldots\ldots x_{1k} \\ 1 & x_{21} & x_{22} & \ldots\ldots x_{2k} \\ . & & & \\ . & & & \\ 1 & x_{n1} & x_{n2} & \ldots\ldots x_{nk} \end{bmatrix} \,, \tag{3.17}$$

$$\beta = \begin{bmatrix} \beta_0 \\ \beta_1 \\ . \\ . \\ \beta_k \end{bmatrix} . \qquad (3.18)$$

The least squares equations are:

$$\sum_{i=1}^{n} y_i = -n\beta_0^{'} + \beta_1^{'} \sum_{i=1}^{n} x_i , \qquad (3.19)$$

$$\sum_{i=1}^{n} x_i y_i = \beta_0^{'} \sum_{i=1}^{n} x_i - \beta_1^{'} \sum_{i=1}^{n} x_i^2, \qquad (3.20)$$

which in matrix form has a solution:

$$\beta^{'} = (X^{'}X)^{-1} X^{'}Y = X^{\#}Y. \qquad (3.21)$$

($X^{\#}$ is the pseudo-inverse of matrix X).

3.3.4 Process Development for MEMS Packaging

In this section, we elucidate on a systematic approach to process development for MEMS packaging. The process described in this section applies mostly to situations encountered during the packaging of MEMS, where production is in low to moderate quantities. This is often the case for MEMS packaging process development or pilot production runs. Process developers finds it useful to understand what process factors affects their response variables the most while at the same time, committing as few resources as they possibly can.

The first step in applying designed experiments to process development under a situation described above is to determine what the goal is (i.e. factor screening, process modeling, process optimization, etc.). Next, process variables are identified. The

process variables include both the response (quality characteristics) and the input variables that affect the process response. While subjective or pass/fail criteria may be used as the response variable, quantitative or measurable variables such as flexural strengths should be used whenever possible. In the case of a MEMS die-to-carrier attachment for example, the process response could be the shear bonding strength between the die and the carrier while the process input variables could be the die attach pressure, the solder material, etc.

As part of a design for reliability methodology proposed in this dissertation, for our MEMS process development process, we followed a systematic method for developing the packaging process. First, process input variables whose effects we are not interested in are kept fixed. Next, using prior experimentation and experience, the range of values and levels for the process factors are chosen. The factor range (lower and upper limits) are often based on some prior knowledge or understanding of the process itself. The choice of level may be such that they are equi-space over the factor range; few levels at the extremities of the range but more at the mid-range; more values at the extremities of the range but less at the mid-range, or randomly assigned within the range. Experiments are then designed based on the factor ranges and levels identified above. Following this, values of the response variables are obtained and the results analyzed using appropriate statistical models to obtain the goal of the experiment.

CHAPTER 4

BACKGROUND: RELIABILITY

The Institute of Electrical and Electronics Engineers (IEEE) Reliability Society [97] defined reliability as "a design engineering discipline which applies scientific knowledge to assure a product will perform its intended function for the required duration within a given environment." Reliability may be considered a function of time and it is often denoted as *R(t)* which is the probability of survival of a device or product over a given time period *(0, t)* i.e. a time value is specified with reliability (e.g. 99.99% reliability at 5000 hours).

If we define the complement of reliability as the failure probability *F(t)*, we can then express reliability mathematically as:

$$F(t) = 1 - R(t). \tag{4.1}$$

F(t) is also called the cumulative distribution function of failure while its derivative with respect to time, *f(t)* is the failure density or probability density function (PDF). The PDF is simply the frequency of failures at time *t*. Mathematically, the PDF may be represented as:

$$f(t) = \frac{dF(t)}{dt} \tag{4.2}$$

Another important reliability concept is the failure rate *z(t)* which is the probability that a device a device that survived at time t will fail during the time interval $t+\Delta t$:

$$\text{i.e. } z(t) = \frac{f(t)}{1 - F(t)}. \qquad (4.3)$$

Any of these three reliability relations may be used as reliability measures. Reliability is best described in terms of products. If we say that a product is reliable, what we imply is that the product is able to perform its intended purpose under normal operating conditions for at least, the specified life time of the product. Thus, when a device malfunctions prematurely, we say that it is not reliable. A formal description of reliability requires that we specify the normal use condition as well as the life expectancy while under normal usage. Reliability addresses the following questions about a product:

- The probability that it will fail at a given time.
- The expected lifetime of the product.

4.1 MEMS Reliability

MEMS Reliability is critical because a lot of devices have applications in critical products such as the automobile safety air bags sensors, implantable medical devices, optical switches, etc. The consequence of unexpected failure or lack of reliability in these devices is often catastrophic as would be expected in the case of non deployment of a car safety air bag during a crash. The effect of reliability on MEMS products is profound, and lately, there has been more emphasis on research leading to understanding and improving reliability of MEMS products.

Being a relatively new technology that is just being applied to commercial products, there's still a lot to understand regarding MEMS reliability. However, we should mention that certain commercial MEMS products (e.g. MEMS based air bag accelerometers) have better reliability than their non-MEMS based precursors and they do outlive the vehicles they are installed in [99]. Also, MEMS based switches are known to have extremely long life cycles of several billions of cycles compared to the million of cycles for conventional mechanical switches [100].

As stated earlier, MEMS packaging fulfils several roles including protecting the device, enhancing device performance and reliability, or put simply, prevent device failure. In order to fulfill these roles and in view of the wide variation of MEMS application areas, we will examine some of MEMS failure mechanisms in order to understand how to use packaging to mitigate failure.

4.2 MEMS Failure Modes and Mechanisms

Several mechanisms that promote the occurrence of failure have been identified in MEMS. Failure may be due to mechanical, electrical or environmental effects leading to the following failure mechanisms: material degradation, excessive intrinsic stresses, packaging technique, environmental factors, etc. Our focus will mostly be on failure resulting from mechanical and environmental effects. Most MEMS devices include moving mechanical structures which are susceptible to mechanical failure.

Several factors promote mechanical failure in moving MEMS mechanical structures. Some of these factors are discussed below:

4.2.1 Cyclic Mechanical Fatigue

MEMS failure due to alternating mechanical loads at elevated temperature is a common occurrence in MEMS, especially those with tiny movable structural members fabricated from low melting materials e.g. aluminum. For example, in the early stage of development, one of the most significant failure modes in the Texas Instrument's DMD™ was hinge memory. This failure was associated with metal creep of the hinge material at the elevated operating temperatures of the DMD™ [101].

Creep failure is also found to be a major reliability failure mode in RF-MEMS switches with microparts made from aluminum material [103-104]. These RF-switches consists of suspended aluminum beams that are pulled down via electrostatic forces. When subjected to alternating mechanical loads at elevated temperatures, these beams may experience creep leading to failure at loads significantly below their yield strength or ultimate strength. Modlinski [105] proposed a method for increasing the creep resistivity of aluminum through a precipitation hardening process. Indium based solder and soft solders used for attachments and interconnection are also common sources of creep in MEMS. This may be avoided by using hard solders with reduced creep tendency e.g. eutectic 80Au-20Sn solder metal.

4.2.2 Excessive Stresses

Stresses in MEMS can be classified as either internal (or extrinsic) and intrinsic stresses. Extrinsic stresses are developed when a material is subjected to environmental excursions e.g. the thermomechanical stresses due to CTE mismatch during thermal cycling processes. Intrinsic stress in MEMS is associated with thin film microfabrication process methods (e.g. deposition and plating) and material property. Many MEMS

structures are fabricated by thin film additive processes (e.g. sputtering) involving several layers of materials on a silicon substrate. As a result of the elevated process temperatures of these processes and difference in material properties of the deposited thin film materials, thermal stresses are developed in these materials. These stresses remain unless they are relieved (e.g. through annealing process).

4.2.3 Stiction

As stated by Feynman [106], as we scale down in size, all things do not scale down proportionally. This may result in the domination of surface forces (e.g. capillary and molecular Van der Waals) over body forces (e.g. inertia). These attractive surface may result in stiction (static friction) failure in MEMS if they are of same order of magnitude as the actuation forces generated by the MEMS device. Two types of stiction are identified in MEMS. These are release stiction and in-use stiction. Stiction in MEMS result in reduced yield and reduced reliability.

Release stiction is a direct result of the release step of MEMS micromachining involving the use of liquid chemicals such as hydrofluoric acid (HF) to remove the sacrificial layer. As the liquid evaporates, capillary forces between MEMS microparts and adjacent surfaces pull them together. As the liquid between the microparts and surfaces evaporates, the liquid meniscus formed produces capillary forces that attract the MEMS part to the surface. The incidence of this type of stiction is reduced or eliminated by using super critical CO_2 drying, freeze sublimation, and the use of dry etching for the release step.

In-use stiction on the other hand, occurs after MEMS release step (e.g. during operation or storage). This type of stiction may occur as a result of intermolecular

attraction forces, absorbed or condensed moisture between adjacent surfaces of microparts. The incidence of this stiction type may be mitigated through hermetic vacuum packaging or the use of in-package moisture getters. The presence of moisture may also lead to MEMS failure through corrosion.

4.2.4 Material Degradation

Material degradation of polymers and organic materials is an important failure route for MEMS. Polymer based material such as benzocyclobutene (BCB) and polydimethyIsiloxane (PDMS) are increasingly being used in MEMS due to cost considerations and their desirable properties such as resistance to chemical attack and good adhesion properties. The drawback to the use of organic materials in MEMS is the degradation of these materials over time via ageing and thermal decomposition, leading to release of gas (outgassing) and loss of material compliance.

4.2.5 Environmental Factors

The performance and reliability of many MEMS devices are impacted by the environment including both the environment inside and outside of the package. For instance, vacuum environment is desirable for MEMS resonators while it is important to prevent the ingress of moisture and particles for optical switches. Two of the primary causes of MEMS failure are stiction of the moving microparts due to moisture from environment and particulate contamination due to the degradation of organic materials in the device.

4.3 Accelerated Testing for IC and MEMS

Ideally, reliability testing for microelectronics and MEMS would involve subjecting the device to operating and environmental conditions typical of normal usage.

The obvious disadvantage of this is the time it will take to complete such a test regime. Accelerated life tests are series of tests that are carried out at higher that normal stress levels or stress cycle frequency to predict the long term reliability of a device. The applied stress could be mechanical loading (such as compressive, tensile, or shear force), thermal (e.g. heat flux), electrical (e.g. current or voltage), or a combination of two or more of these load types. The choice of accelerated life test for a particular device is often based on the expected failure mode due to environmental or operating conditions. Accelerated life test may be used to reveal possible failure modes or mechanisms [107]. From the results of the accelerated life test, the long term reliability of the device may then be predicted. Examples of test conditions for accelerated life testing includes temperature (or thermal) cycling, power cycling, thermal shock, mechanical shock, drop tests, sinusoidal vibration tests, random vibration tests, voltage extremes, and high humidity.

There are different qualification standards and specifications available to qualify the reliability of packages and packaging processes. These test standards provides common testing basis for devices irrespective of the manufacturer or testing equipment. Since the intent of qualification standards and specifications is not necessarily to induce failure but rather to verify that the device will be able to meet certain criteria, it is obvious that device qualification does not provide much information about the mode or mechanism of failure, neither are they able to provide information about the probability of the occurrence of failure hence the need for accelerated life testing. It should be pointed out here that currently, there are no qualification standard and specifications for MEMS and that the current standards typically used for MEMS originate from

microelectronics. However, because of the similarities in their construction and failure modes, qualification standards and specifications for microelectronics are often adopted for MEMS as well.

Depending on the objective, accelerated life test may be classified as [107]:

- Product development/verification tests.
- Qualification (screening) tests.
- Accelerated life tests (ALT) and highly accelerated life tests (HALT).

Product development tests are generally destructive tests that are performed during the design, development and early stages of manufacturing of a product. The aim of these tests is to gain information on the limitation of product design, materials, and fabrication processes. The information obtained from these tests are used to make design modifications. Qualification tests are used to assess whether a device meets a specified level of reliability specification. Accelerated life tests and highly accelerated life tests are destructive tests used to identify the modes and mechanisms of failure in a device and to obtain statistical data regarding failure in a device.

4.4 Some MEMS Reliability Qualification Tests

4.4.1 Hermeticity Testing

The purpose of this test is to determine the hermeticity or lack thereof of a sealed package. The MIL-STD 883F test protocol outlines the basic equipment set up and testing methods for assessing the hermeticity of sealed packages. In this section, we discuss the Military Standard 883E testing method 1014 test condition C4/C5 for fine and gross leaks using optical methods. This test method utilizes an optical leak detector that is preset and properly calibrated for an equivalent standard leak rate sensitivity sufficient to

read measured Helium leak rates of 10^{-5} atm-cc/sec and greater for gross leak detection for test condition C4, and $5x10^{-9}$ atm.-cc/sec and greater for fine leak detection for test condition C5.

Since this test method involves subjecting a sealed package in the test chamber to vacuum and then, up to 30 psi of pressure, the maximum allowable pressure the device under test (DUT) may be safely subjected to must be known in order to prevent damage to the DUT as a result of excessive test chamber pressure or vacuum.

4.4.1.1 Lid Stiffness

The use of the optical leak test is valid for packages with relatively thin metallic or ceramic lids or other materials that meet the following lid stiffness requirements:

For condition C4 (gross leak):

$$R^4/ET^3 > 1.0\text{X}10^{-4}. \quad (4.4)$$

For condition C5 (fine leak):

$$R^4/ET^3 > 3.0\text{X}10^{-4}. \quad (4.5)$$

Where:

R = the minimum width of free lid (inside braze or cavity dimension in inches).

E = the modulus of elasticity of the lid material.

T = the thickness of the lid (inches).

4.4.1.2 Sensitivity

The test sensitivity is related to the extent of measurable deformation of the lid. The measurable deformation is increased by increasing the specific pressure differential

and the test time used. For a specific lid material and size the following formula indicates the minimum measurable deformation:

The leak rate sensitivity is provided by the following equation:

$$L = (-V_0 / k_2\, t) \times \ln (1 - D\gamma t / P_0 L_0), \qquad (4.6)$$

where:

L = The leak rate sensitivity of the test (atm-cc/sec),

V_0 = The volume of the package cavity (in3),

K_2 = The leak test gas constant (air = 1.0, He = 2.67),

t = The test duration time (seconds),

$D\gamma t$ = The measured deformation of the package lid (inches),

P_0 = The chamber pressure during the test (psig),

L_0 = The lid stiffness constant calculated from the package dimensions (inch/psi),

Note: L_0 is calculated using the Roark formula for stress and strain on a flat plate having a uniform load over the entire area. The formula for a rectangular lid is:

$$L_0 = \alpha \frac{b^4}{ET^3}, \qquad (4.7)$$

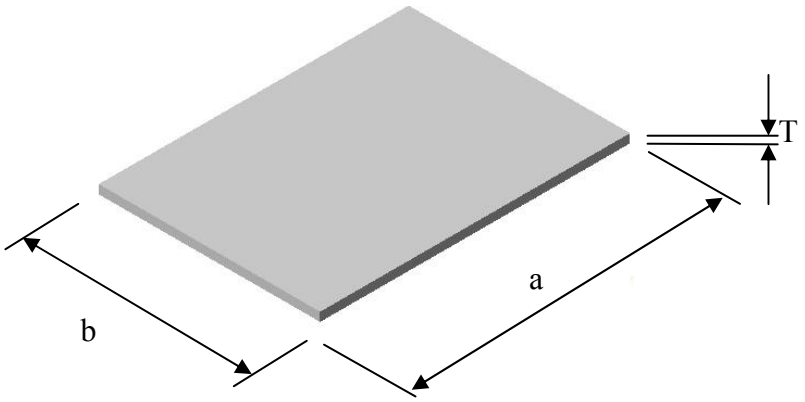

Figure 4.1 Flat plate with uniform load over the entire area.

where:

α = Aspect Ratio Constant determined by measurements *a and b* (See Military Standard 883E testing method 1014 test condition C4/C5 for typical values),

a = Lid length – measure of the longer side (inches),

b = Lid width – measure of the shorter side (inches),

E = Modulus of Elasticity for the lid material used,

T = Lid thickness (inches).

For a specific package lid thickness (T), and volume (V_0), the leak rate sensitivity (L) is improved by increasing the test time (t) and chamber pressure (P_0).

4.4.1.3 Retest

Packages are inspected within 30 minutes of their having been seam sealed or subjected to an elevated temperature bake. The package needs to reach ambient temperature before testing. Also, package retest is performed after at least 4 times the test time before retesting (for fine leak), to allow the package to return to ambient pressure.

4.4.1.4 Failure Criteria

The pass/fail criteria needs to be specified based on the customer's specification for gross and fine leak rate and sensitivity. Where this is not explicitly specified, the following threshold values are used:

Gross leak: 10^{-5} atm-cc/sec and greater

Fine leak: 5×10^{-9} atm-cc/sec and greater

4.4.2 Wire Bond Pull Test

The purpose of this test is to evaluate wire bond quality of gold and aluminum wire bonds. These test protocols can be used only when the loop height of the wire bond

is large enough to allow a suitable hook for pulling to be placed under the wire. These methods are destructive in nature and are appropriate for use in process development or, with a proper sampling plan, for process control or quality assurance. A typical test set up for wire bond pull test is shown in Figure 4.2.

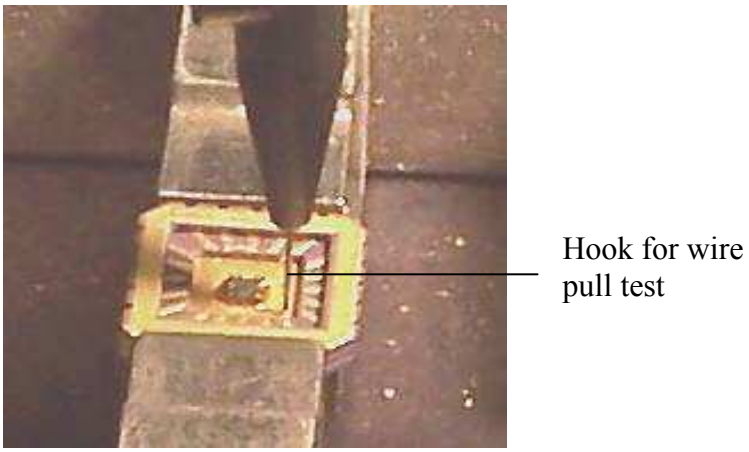

Figure 4.2 Test set up for wire bond pull test.

4.4.2.1 Summary of Test Methods

The device under test (DUT), with the wire bond to be tested is clamped using an appropriate fixture. A hook is positioned under the wire midway between the two bonds and a pull force applied in a direction approximately normal to the die or substrate surface. The hook is raised until the wire bond breaks. The force applied to the hook in order to cause failure of the wire bond and the failure category are recorded. For wire diameter or equivalent cross section greater than 0.005 inch, where a hook will not fit under the wire, a suitable clamp can be used in lieu of a hook.

4.4.2.2 Procedures

- Place the device having the wire bond to be tested in the device holder so that the plane of the device is horizontal.
- Position the microscope and light source and focus the microscope so that the wire bond to be tested is clearly seen in the microscope field.
- Position the device holder so that the wire forming the loop of the wire bond to be tested is under the rigidly mounted pulling hook.
- While viewing the wire bond through the microscope, maneuver the hook so that it is under the wire loop to be pulled, and adjust the hook so that it is midway between the two bonds and contacting the wire loop, as judged by eye.
- Activate the pulling mechanism while observing the wire bond and hook through the microscope. Continue pulling until there is failure.
- If the wire fails at the point of contact with the hook, record the test for that bond as invalid.
- Measure and record the force required for breaking the wire bond.
- Record the identification of the wire bond and the identification of the device (substrate).
- Examine the remaining parts of the bonds and the wire span at appropriate magnification to determine the nature and location of the failure.

4.4.2.3 Failure Criteria

Any bond pull which results in separation under an applied stress less than that indicated in Table 4.1 as the required minimum bond strength for the indicated test condition, composition, and construction shall constitute a failure.

Table 4.1 Minimum bond strength for wire bonding [107].

Test condition	Wire composition and diameter 1/	Construction 2/	Minimum bond strength (grams force)	
			Pre seal	Post seal and any other processing and screening when applicable
A	---	---	Given in applicable document	Given in applicable document
C or D	AL 0.0007 in AU 0.0007 in	Wire	1.5 2.0	1.0 1.5
C or D	AL 0.0010 in AU 0.0010 in	Wire	2.5 3.0	1.5 2.5
C or D	AL 0.00125 in AU 0.00125 in	Wire	Same bond strength limits as the 0.0013 in wire	
C or D	AL 0.0013 in AU 0.0013 in	Wire	3.0 4.0	2.0 3.0
C or D	AL 0.0015 in AU 0.0015 in	Wire	4.0 5.0	2.5 4.0
C or D	AL 0.0030 in AU 0.0030 in	Wire	12.0 15.0	8.0 12.0
F	Any	Flip-clip	5 grams-force x number of bonds (bumps)	
G or H	Any	Beam lead	30 grams force in accordance with linear millimeter of nominal undeformed (before bonding) beam width. 3/	

1/ For wire diameters not specified, use the curve of figure 2011-1 to determine the bond pull limit.
2/ For ribbon wire, use the equivalent round wire diameter which gives the same cross-sectional area as the ribbon wire being tested.
3/ For condition G or H, the bond strength shall be determined by dividing the breaking force by the total of the nominal beam widths before bonding.

4.4.2.4 Failure Category

When specified, the stress required to achieve separation and the category of separation or failure shall be recorded for external bonds connecting device to wiring board or substrate:

1. Lead or terminal break at deformation point (weld affected region).

2. Lead or terminal break at point not affected by bonding process.

3. Failure in bond interface (in solder or at point of weld interface between lead or terminal and the board or substrate conductor to which the bond was made).

4. Conductor lifted from board or substrate.

5. Fracture within board or substrate.

4.4.3 Fiber Pull Test

The purpose of this test is to evaluate the bond quality of an optical fiber bonded to a device, or a device carrier package using a solder material. These test protocols can be used only when the optical fiber has a free, unrestrained end. For ease of testing, the free length of the fiber should be at least 3 inches long. These methods are destructive in nature and are appropriate for use in process development or, with a proper sampling plan, for process control or quality assurance.

4.4.3.1 Summary of Test Method

The device under test (DUT) is clamped using an appropriate fixture. The free end of the fiber is clamped using appropriate padding and fixtures that ensures that the fiber is not damaged, while at the same time, ensures that the fiber does not slip from the clamp during pulling. With the package clamp stationary, the fiber clamp is gradually raised until failure occurs in the fiber bond to the package. In order to ensure that the fiber is subjected to pure axial loading, there should be no offset in the clamps holding the package and the fiber. When a failure occurs, the force causing the failure is recorded. If the fiber breaks at any point, the test is discarded and the test is invalid.

4.4.3.2 Failure Criteria

The failure criteria may be based on the ultimate tensile strength (UTS) of the solder material. The minimum pulling load is obtained by multiplying the solder UTS by the fiber area attached to the solder.

CHAPTER 5

METHODOLOGY: DESIGN FOR RELIABILITY (DfR) IN MEMS/MOEMS PACKAGING

A key objective of this research work is to formulate a framework for applying *DfR* principles to MOEMS packaging. This research work presents a unique approach to MOEMS packaging with reliability as the focal point. To demonstrate the use of *DfR* in MEMS packaging, two case studies involving the packaging of MOEMS switches will be undertaken. The packaging aspects presented includes die-to-carrier attachment, optical fiber-to-carrier attachment, wire bonding, and hermetic lid sealing. The framework adopted in this research work involves the following strategies:

- Problem definition
- Package design
- Process development
- Reliability studies
- Case study

Problem definition: The problem considered here is the development of reliable MOEMS back-end packaging. This includes an understanding of the back-end packaging processes to be undertaken, material choice, attachment methods, package design, failure mechanism, reliability considerations, identification of tools and equipments for packaging and reliability tests.

Package design: Once the problem scope has been defined, package design is implemented. This is basically to define packaging needs and requirements, and to ensure that these needs and requirements are met.

Process development: This involves a definition of all packaging processes (using tools such as computer simulation and experimentation) and sequence of packaging steps. A very important activity here is the packaging process definition in terms of parameter settings. Here, the alternative processing routes are examined, process windows for parameters are established, and the process parameters effects on reliability are examined by modeling the process.

Case studies: Two case studies will be implemented to demonstrate the application of *DfR* to MEMS packaging. These studies are concerned with the packaging of MOEMS switches with several components to be attached and sealed hermetically. Reliability tests and failure criteria will be developed for the packaging processes to be discussed.

This approach addresses reliability concerns at the early stages of product development, while at the same time, providing fundamental understanding of how and to what extent controllable and uncontrollable factors affects the reliability of products or systems. This dissertation introduces a layered approach which has been developed for implementing *DfR* for MEMS packaging. This approach is explained with the aid of the sketch on Figure 5.1 referred to as *"DfR iterative loop"*.

The first abstraction layer in this framework involves packaging conceptualization and definition whereby we sought to gain understanding of the packaging requirements. This occurs concurrently with the device conceptualization. Decisions are made at this time as to which packaging operations takes place at the front end (during device

fabrication) and which ones takes place at the back end (after device fabrication). Simulation is an important tool that may be used to examine the suitability of packaging solution proposed at this stage. It is also important to apply tools such as physics of failure and failure modes and effects analysis (FMEA) in making design decisions that affect the package and device reliability.

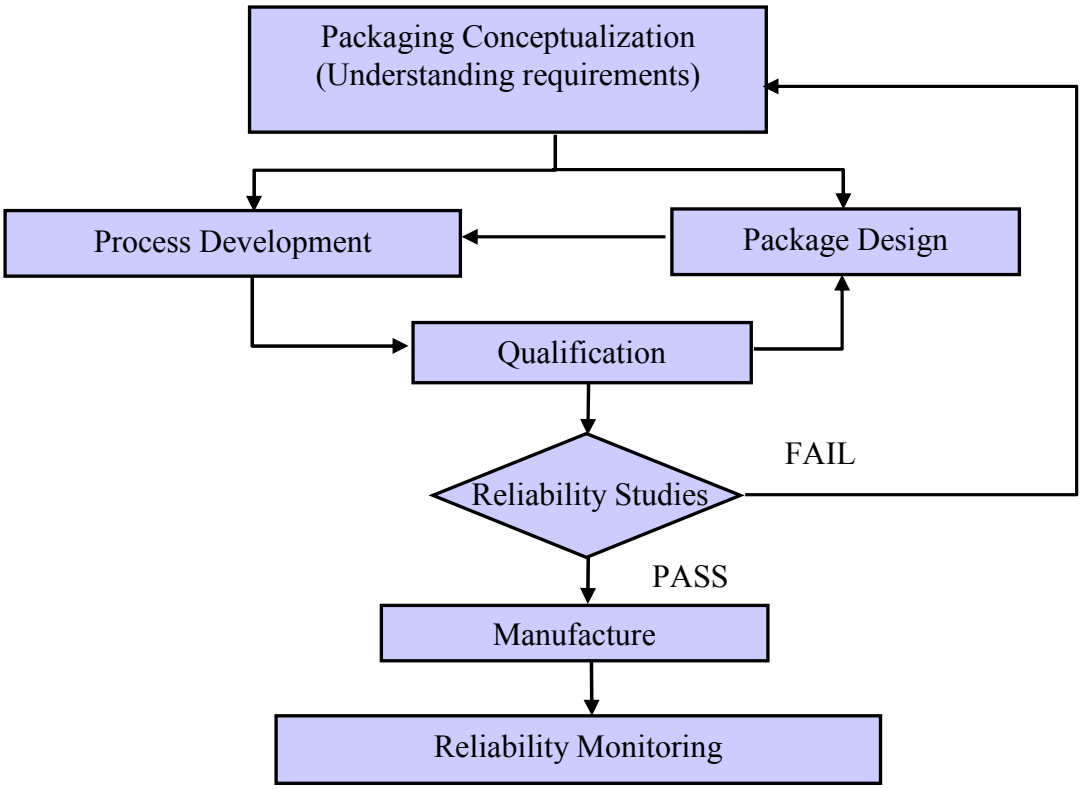

Figure 5.1 DfR Iterative Loop for MOEMS Packaging.

The next step involves concurrent detailed package design and process development. It should be noted that the process development process may be influenced by the package design and vice versa. Package design includes designs for the actualization of packaging functions such as protection from the environment, electrical

or optical interconnection. Process development involves definition in terms of parameter settings, evaluation of alternative processing routes, establishing process windows for parameters and determining process parameters that affect package reliability. Concurrent design, simulation, and reliability testing should be adopted to achieve optimal package design and processes.

The next layer involves package evaluation using qualification standards and specifications such as the die shear and wire bond pull test using the MIL-STD 883F. If qualification requirements are not met, we go back to tweak the package design and the process development. Finally, we carry out reliability studies using accelerated tests such as temperature and power cycling tests to examine the long term effect of the package on reliability. We observe in Figure 5.1 that even after manufacturing commences, and throughout product life, reliability monitoring of the device continues. This is necessary in order to validate assumed reliability models.

The *DfR* iteration loop is illustrated by applying it to demanding MOEMS applications that requires extended shelf lives of over 25 years. In these cases, process development allows for a limited number of experimental samples, due to cost constraints and part availability. The expected long life of this device requires hermetic packaging capable of passing the MIL-STD 883F for fine and gross leak tests, and the use of fluxless attachment and sealing methods to prevent reliability problems due to degradation of flux and flux residues.

5.1 Packaging Concept

Developing packaging concept is the first key consideration in the packaging of MEMS. This is carried out concurrently with device design. Two key aspects of MEMS

packaging are application area and reliability. It is sometimes difficult to decouple these two. Very often, the reliability requirements imposed on a MEMS device are dictated by the application area for the device. It is at the ***packaging concept*** stage that the packaging needs and requirements for a MEMS device are identified and ideas are generated on the packaging materials, architecture, processing, processing equipment, etc to use.

One of the devices described in this dissertation is a one time use MOEMS device with expected shelf storage time of up to 25 years. As a result of the long storage life requirement, and the use of optical components, it is desirable to provide corrosion resistant hermetic packaging without the use of organic materials. This may be achieved at the carrier level using custom machined, gold-coated Kovar® metal housing with a lid. The carrier material was chosen so as to reduce the CTE mismatch to the silicon die [33].

The order in which components are assembled also affects the choice of materials for sealing and attachment. In addition, these materials were chosen such that there is adequate wetting between solder metals and the parts to be soldered without the need for fluxing agents. The experiments described in this dissertation were carried out at UT Arlington's Texas MicroFactory™ cleanroom located at the Automation & Robotics Research Institute (ARRI), and at the Bennington Microtechnology Center (BMC) in Vermont, a startup MEMS packaging facility.

5.2 Package Design

Apart from the traditional functions of semiconductor packaging such as power and signal distribution, thermal management, and protection of the device from environmental influences [39, 73], MOEMS packages are expected to meet additional reliability criteria, consistent to mechanical and optical failure modes. Considerations for

package requirements includes the die size, device working temperature range, device failure mode, the environment under which the device is to operate, mechanical robustness, thermal management, lead-free requirements, and costs [74]. In order to enhance the reliability of this device, hermetic packaging using a metal or ceramic based carrier is required.

For this application, the MOEMS die containing electrothermal actuators must be packaged together with 4 optical and 8 electrical interconnects. The MEMS layout requires that 1′ long fibers be placed around the carrier as shown in Figure 5.2. Because of assembly constraints, the order in which components are added to the package is as follows: die & top chip attach, wire bonding, optical fiber sealing, and finally seam sealing of the top lid. One can easily see that any different assembly order is not feasible.

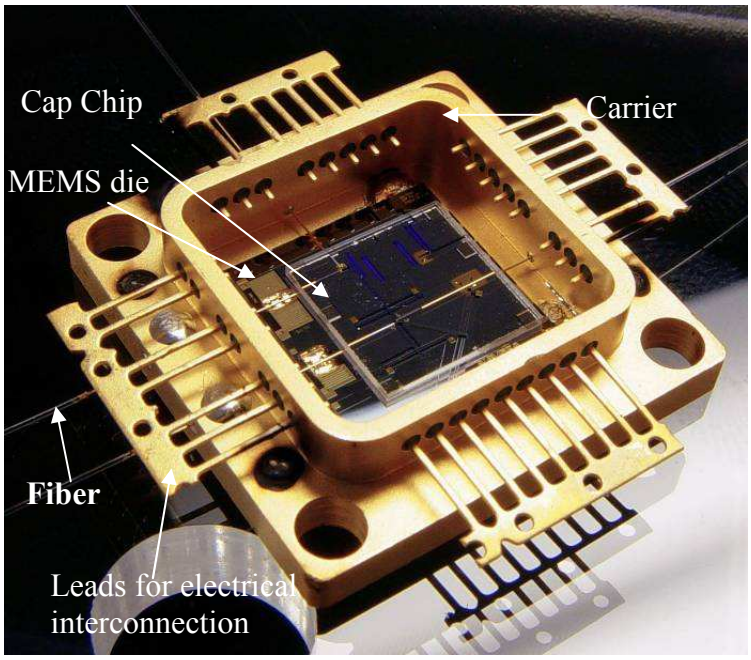

Figure 5.2 MOEMS application device showing the carrier, attached optical fibers, MOEMS die, and cap.

The leak routes for this package are the package lid and the fiber-to-carrier attachment joints. Hermetic lid sealing of the Kovar® carrier is obtained via lid seam sealing. MEMS die mechanical reliability is obtained through attachment to the Kovar® carrier using a metallic joint. A good candidate solder for this operation is eutectic SnAu. The reliability of SnAu solder joints is fairly well understood [108-109].

Sealing of optical interconnections is obtained via trenches microfabricated on the MEMS die via DRIE (Deep Reaction Ion Etching), [110-111] and attachment using fluxless soldering. Because of the order of assembly, the melting temperature of the optical solder joints should be less than the reflow temperature of the SnAu solder for die attach. In addition, this solder joint is based on using metallized fibers and liquid reflow of the joint through the Au-coated carrier side wall. A good candidate material, with well-known solder joint reliability to Au is indium. These solder joints can be formed via hot-plate global reflow, or individually via localized heating by laser energy. In order to reflow all 4 joints simultaneously, a complex fixture needs to be used. Furthermore, achieving appropriate indium reflow temperatures with a hot plate is time consuming and offers an increased chance for indium-oxide formation. Alternatively, localized heating using a semiconductor diode laser offers advantages such as: simplified fixturing, faster process time, and less chance for indium-oxide formation.

Protection of delicate MEMS structures on the die and the vertical (z) axis constraint of the optical fibers can be obtained by using a cap chip flip-chip bonded to the MEMS die. This step can be accomplished simultaneously to die-attach via Au-Sn solder pads on both surfaces.

With respect to the electrical interconnects, several form-factors can be used. In one, the leads exit the carrier from the side walls similar to butterfly packages (with glass seal between the carrier and the leads) while in the later version, the leads exit the carrier from the bottom wall as shown in Figure 5.3.

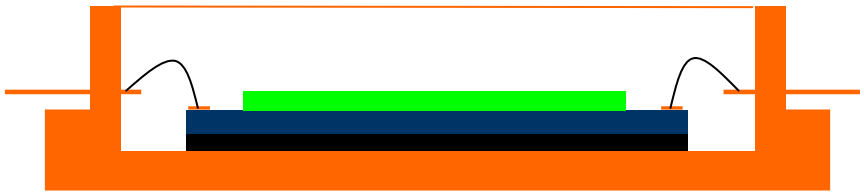

(a)

(b)

Figure 5.3 Package electrical interconnect pin configuration types
(a) butterfly and (b) plug-in packages.

5.3 Process Development

A useful tool in process development and improvement is statistically designed experiments. These are particularly useful in MEMS packaging because of the low to medium quantity order encountered, and higher component costs. As a result, fewer experiments are available for process development. By applying design of experiment

principles, we are better able to maximize information regarding the process input/output relationship such as the input factors that affect the process output/response and the sensitivity of the process output to the input variables. The key steps in applying DOE to process development include [112]:

- Determine the purpose of the experiment.
- Identify the process output whose effect is of interest.
- Identify the process input variables.
- Select an appropriate experimental design.
- Perform the experiments.
- Analyze the results.

The approach adopted in this research work is to

- Identify all the packaging steps required and the process flow.
- For each process, identify the process parameters and the response variable(s).
- For each process parameter, determine the process window.
- Use experimental design principles to construct efficient experiments to investigate the effects of process parameters (including materials, processing temperature, ambient environment, etc) on the response variable(s) (reliability of each of the packaging step involved in the packaging process). This is a screening design.
- Use the process parameters that are significant to construct a central composite design (CCD) for response surface modeling to obtain parameter optimization.

We will further explain this methodology using the following examples.

5.3.1 MEMS Die-to-Carrier Attachment

For a given carrier, die, and die attach material, assume that we are confronted with the task of attaching a MEMS die to a carrier housing and that we need to first identify the die attachment process parameters (or factors). These include the bonding pressure, the soldering environment, such as the oxygen level, the reflow temperature, the heating duration, etc. Next, we must identify the die attachment quality characteristics (or response factors) such as the die shear strength. Then, we determine the optimal die attachment process values for the task by constructing an appropriate experimental design and performing the designed experiments. The design is based on process parameters and quality characteristics already identified. Finally, analysis that identifies the significant process parameters, the sensitivity of the quality characteristics to the process parameters, and the levels of the process parameters that optimizes the quality characteristics are performed.

5.3.2 Fiber-to-Carrier Attachment

In the case of the optical fiber-to-carrier attachment, we proceed with a carrier design for housing the MEMS switch components. In this case, the heating source for solder reflow is a semiconductor diode laser. Therefore, we need to determine the carrier laser absorption at the laser operating wavelength by using inverse thermal analysis. We then construct a finite element (FE) thermal model to predict the carrier temperature distribution due to laser heating. Using the model, we estimate the laser power and heating duration requirement of the soldering process. In our case, we found that because of the high laser reflection on the gold surface of the carrier, not enough heat is delivered

to the carrier. We then carried out further FE analysis using modified carrier surface properties to reduce the amount of laser energy that is reflected from the carrier surface.

An additional analysis was carried out to investigate the effect of carrier geometry modification on the heat distribution in the package. Finally, we identified the fiber attachment process parameters such as the laser power density, heating duration, shielding gas, oxygen level, etc., and the quality characteristics such as the fiber pull strength, fiber damage (e.g. cracks), porosity/voids in solder joint, etc. Designed experiments were constructed to determine the significant process factors, their sensitivities and optimal levels of these factors that optimizes the quality characteristics.

5.4 Reliability Specifications for MOEMS Switch

5.4.1 Die Shear Strength

The strength of attached die is expected to meet the specification outlined in the MIL-STD 883G TM 2019.7 described in section 4.4.1. The required shear strength is given in Table 5.1.

Table 5.1 Die Shear Strength.

Attached Die Area (in^2)	Shear Strength (kg)
Larger than $64x10^{-4}$	2.5
Larger than or equal to $5x10^{-4}$	Obtain value from Figure
Smaller than $5x10^{-4}$	0.04

Our die sizes are typically about 10mm x 10mm, yielding attached area of $100mm^2$ ($0.155\ in^{-2}$). The required shear strength is therefore 2.5 kg.

5.4.2 Fiber Pull Strength

Ideally, failure at the fiber-to-carrier bond should be due to bulk solder failure as opposed to interfacial failure at the solder/fiber interface. The tensile load to cause bulk solder failure is obtained from the contact area of the fiber and the tensile strength of the indium solder. Assuming a fiber diameter of 125 μm and a tensile strength of 4.5MPa for indium, the tensile load is 7N.

5.4.3 Leak Test

The expected standard leak rate for the carrier-level MOEMS switch less than 5x10-8 atm cc/s.

CHAPTER 6

DESIGN FOR RELIABILITY APPLIED TO MEMS PACKAGING

In this chapter, we demonstrate the application of DfR to the packaging of two demanding MOEMS application devices. The chapter starts with the descriptions of the assembly, attachment, and packaging processes for these application devices. These application devices are MOEMS switches. As a result of reliability considerations, these devices require hermetic packaging in order to enhance their shelf lives. In the first application device, called carrier level MOEMS switch, hermetic sealing is achieved at the carrier level by sealing the lid and four optical fibers to the carrier while in the second application device, called die level MOEMS switch, hermetic sealing is obtained at the die level by sealing a top glass die to the MOEMS die.

Each MOEMS design presents unique assembly, packaging, and reliability challenges. Test vehicle samples were used in order to cut down the costs associated with the process development of the packaging activities presented in this research work. By using these test vehicles, the number of actual MOEMS components needed for process development and reliability studies were minimized. The test vehicles are similar in material, surface finish and construction to the components of the actual application devices.

In addition to the MOEMS switches, we also describe, a MEMS based implantable micropump for drug delivery. Our discussion in this chapter is limited to the design, operation, fabrication and packaging aspects of the micropump. Later in Chapter 7, we discuss the use of reduced order modeling and FEA as an aid in package design for this device.

6.1 Carrier Level MOEMS Switch

6.1.1 Description of Carrier Level MOEMS Switch

The carrier level MOEMS switch application device is schematically shown in Figure 6.1. It consists of Kovar® based carrier package and lid, metallized optical fibers fed through the carrier, silicon MEMS die with a glass cap, and wire-bonds for electrical interconnection. A description of the MEMS die, including its microfabrication processes and operation of the MOEMS device can be found in Deeds, 2004 [66].

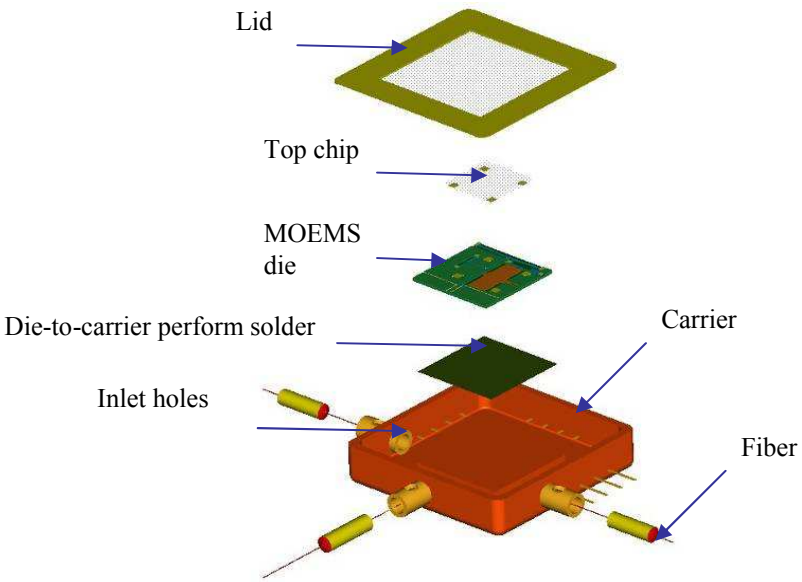

Figure 6.1 Schematics of the carrier level MOEMS switch consisting of Kovar based carrier, optical fibers, MOEMS die, top cap chip, and lid [courtesy Michael Deeds].

The carrier package is made of Kovar® metal with a 0.5 micron nickel and gold layer coating. The gold layer impacts corrosion resistance to the metal package and also promotes wetting of the solders used for the fiber-to-carrier, and the MEMS die-to-carrier attachment processes. The carrier package houses the silicon MEMS die and the glass top chip. It has four holes on the side walls for optical fiber insertion into DRIE trenches in the silicon MEMS die. The silicon MEMS die is the main component in this MOEMS switch. The glass top chip constrains the fiber in the z (vertical) direction.

6.1.2 Summary of Packaging Process

The process flow for the packaging of the carrier level MOEMS switch is illustrated in Figure 6.2.

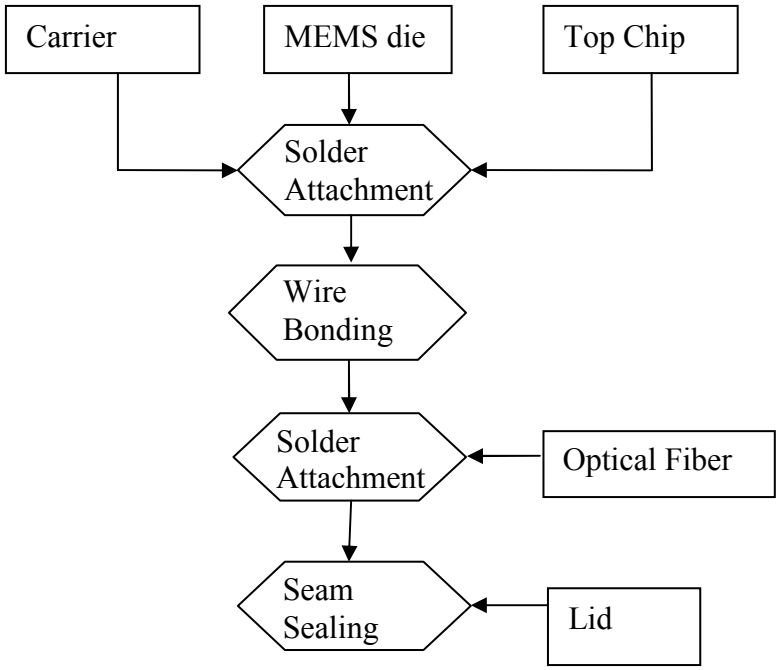

Figure 6.2 Packaging process flow for carrier level MOEMS switch.

The packaging of the carrier level MOEMS switch consists of the following three key attachment processes:

- Silicon die to carrier package attachment using a thin square 80%Au20%Sn eutectic solder preform.
- Glass top chip to silicon die attachment using Au-In solder bumps at the edges of the glass top chip and silicon die.
- Optical fiber to carrier package attachment using 99.999% indium preform.

The packaging process starts with die attachment consisting of two solder attachment processes taking place simultaneously – the die-to-carrier bonding and the top-chip-to-die bonding. This step is followed by wire bonding for the creation of electrical interconnection path from the MOEMS die to the carrier interconnection pins. The next attachment process is the optical fiber-to-carrier attachment for creating optical interconnection paths and finally, the carrier is sealed with a lid to protect the MOEMS die from the environment.

This carrier level packaging process starts with the pick up of a custom machined carrier from a precision machined parts tray. This carrier is placed at a pre-determined location on a hot plate. With appropriate fixtures and a positioning accuracy better than 25 μm, an 80%Au-20%Sn solder preform, a MEMS chip and a glass top chip are stacked sequentially onto the carrier package and bonded. The pick up and alignment operations were performed using M^3, a customized microassembly robotic system [62].

The next packaging step is the optical fiber to carrier package attachment. This operation is performed in a controlled environment inside a glove box, due to indium's high affinity to oxygen, forming surface oxides. The oxygen level inside the glove box was measured using an oxygen analyzer. The accuracy level of the oxygen analyzer is 1% of the flow sample and it operates in three measuring ranges of 0-2000 ppm, 0-200 ppm, and 0-20 ppm. Before using, it was calibrated with air to 20.9% oxygen.

A modular, easily reconfigurable microassembly cell with 13 degrees of freedom was assembled and fitted inside the glove box for manipulating the carrier, the optical fiber, the heating laser head, the solder material for the fiber attachment, and the overhead camera vision system. The heat source supply for the fiber-to-package attachment is a 0-60 W tunable semiconductor diode laser with 801nm wavelength. This laser system was supplied by Coherent Inc. This laser is capable of operating in both in pulsed and continuous modes. The fiber-to-package attachment process includes the mechanical alignment and insertion of gold coated optical fibers via the feedthrough holes on the carrier package side walls into the trench inside the silicon die as shown in Figure 6.3.

The package (with the die already attached), is placed on a center stage equipped with motorized 2D translational (x,y) and rotational (θ) micro-stages. The bottom surface of the carrier package is insulated in order to minimize the heat sinking effect of the center stage. A motorized camera equipped with zoom-microscope is placed directly above the package for visual feedback. The fiber is held at a

predetermined height with a fiber gripper mounted on a motorized translational (z) micro-stage.

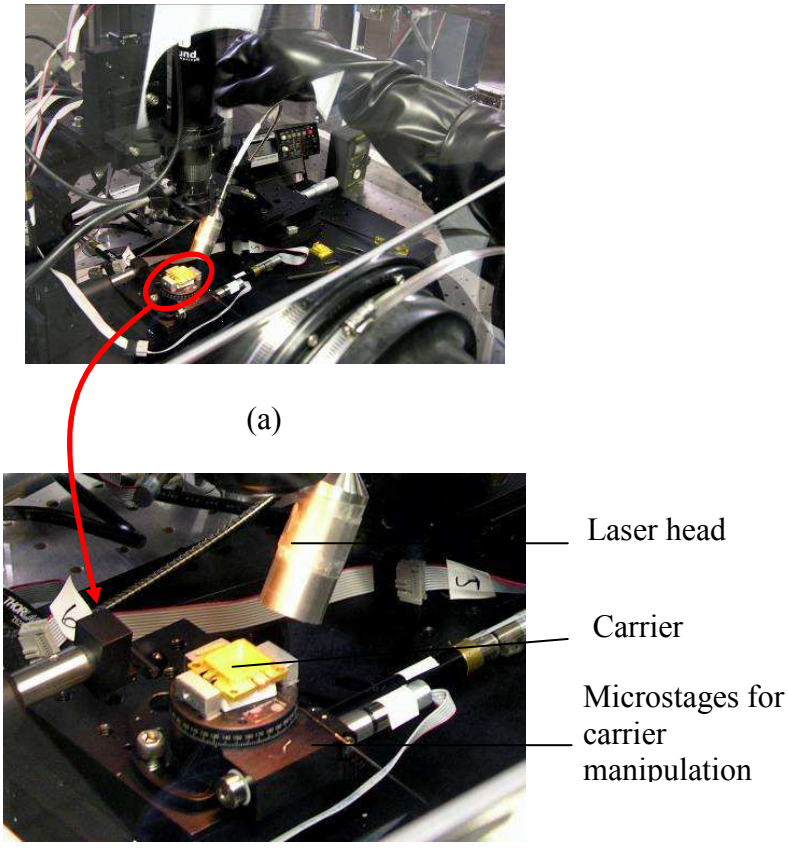

Figure 6.3 (a) Experimental setup for fiber-to-carrier attachment and (b) close up image of experimental setup. This setup comprise of 13 d.o.f. microassembly system for carrier, fiber, solder, laser head, and camera manipulation inside a glove box with controlled ambient.

Using the micro-positioning stages, the fiber is inserted through the feedthrough hole of the package into a DRIE trench inside the die. A solder preform micro-gripper mounted on separate x, y, z micro-stages positions indium preforms used to attach the fiber to the package. The preform which is made of 99.999% indium, is 4 mm long and

0.762 mm in diameter. Finally, a laser head, mounted on an additional x,y,z micro-stage is brought over to shine the laser aiming beam at a predetermined location on the package. After aiming, the laser is turned on to heat the package and melt the solder.

6.1.3 Summary of Process Parameters and Response Variables

A summary of the packaging processes, process parameters and the response variables are presented in Table 6.1. The process windows for most of the process parameters have been established using both experiments and simulations. The most important process parameters driving attachment reliability includes bonding pressure, reflow temperature, dwell time, cleanliness of solder and parts to be attached (including oxide films and organic contaminants), solder type, and soldering environment. Variability due to solder and parts cleanliness was minimized by using an aggressive cleaning procedure involving the use of 10%HCl, acetone, IPA, and plasma cleaning.

Table 6.1 Summary of process, process parameters and response variables.

Process	Factors	Response
MEMS die-to-carrier attachment	Bonding pressure, Reflow temperature, Hold time, Ramp up rate, Ramp down rate, Cleaning method	Die shear strength Voids
Top chip-to-MEMS die attachment	Bonding pressure, Reflow temperature, Hold time, Ramp up rate, Ramp down rate, Cleaning method	Die shear strength Voids
Optical fiber-to-carrier attachment	Laser power, Laser spot size, Reflow temperature, Shielding gas type, Oxygen level, Cleaning method, Heating time	Fiber pull strength
Wire bonding	Bonding pressure, Power, Heating duration, Temperature	Wire pull strength
Carrier lid seam sealing	Power, Force, Travel, Pulse width	Leak rate

6.1.4 Detailed Description of Attachment Processes

6.1.4.1 MEMS Die-to-Carrier and MEMS Die-to-Top Chip Attachment

The first packaging operation involves stacking of the MEMS die and glass top-chip, and their subsequent attachment. In order to obtain attachments with adequate bond strengths, it is essential that the parts to be bonded together be free of surface oxides, dirt, and other contaminants. Prior to die attachment, the carrier was cleaned using wet chemistry by immersing the carrier in acetone to remove organic contaminants, while the solder preform used for the attachment and the silicon MEMS die were cleaned using plasma etching to remove oxide films from the bonding surfaces.

The MEMS die was attached to the Kovar® carrier via a 25 micron thick, 80%Au-20%Sn solder preform, while the top-chip was attached to the MEMS die via multi-layer, thin film Au-Sn solder located on the edges of the MEMS die and the top chip. The solder preform, MEMS die and top chip pick-up and alignment were carried out using M³, a customized multi-scale microassembly robot [62]. In order to obtain enhanced bond strengths, slight static pressure (~20 psi) was applied on the top chip to drive out entrapped air between the carrier package and the silicon MEMS die during the reflow as shown in Figure 6.4. The hot plate is then turned on to start the solder reflow process using a controlled ramp temperature profile to 330+0/-10^{o}C peak temperature. The quality of the die bonding process was later assessed using the die shear test. The values of process parameters (based on prior experiments) are shown in Table 6.2.

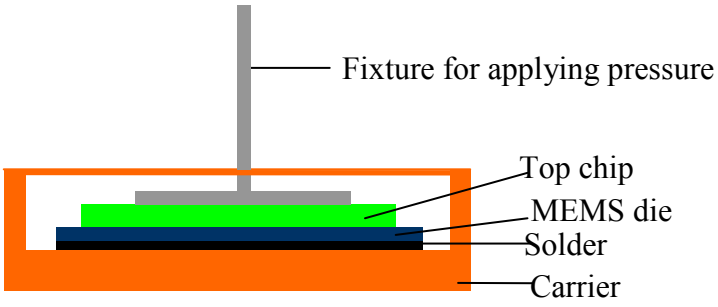

Figure 6.4 Illustration of laboratory setup for MEMS die-to-carrier and MEMS die-to-cap chip attachment showing fixture for applying bonding pressure applied to ensure intimate die contact.

Table 6.2 Test conditions for die-to-carrier attachment.

Bonding pressure	20 psi
Reflow temperature	Peak temperature of 330+0/-10^{o}C
Dwell time	5 minutes at or above solder eutectic temperature

6.1.4.2 Wire Bonding

Electrical interconnection path between a chip and carrier may be established using wire bonding, flip chip bonding or tape automated bonding (TAB). Because of the low I/O requirement of this device, wire bonding using 1mil gold wire was chosen as the electrical interconnection method for this device. This is accomplished using a thermocompression bonder located at Bennington Microtechnology Center. Prior to wire bonding, the packaged die is plasma cleaned in order to improve the wire bond strength [113]. The wire bonding process consists of attaching the carrier to the wire

bonder chuck, heating up the chuck to a specified temperature, configuring the bonder with process settings, and finally executing the bonds. The key process parameters for wire bonding include bonding pressure, power, heating duration, and temperature.

6.1.4.3 Fiber Attachment

The next packaging operation is the fiber-to-package attachment. A fluxless laser soldering process was developed for attaching metallized optical fibers to the Kovar® carrier package. Laser soldering is used in order to localize the carrier heating, preventing the reflow of the already bonded dice. This process consists of optical fiber alignment and insertion through the feed-through holes on the carrier package side walls into the trench inside the MEMS die. Computer controlled motorized high precision micro stages were used for the mechanical alignments using a set up similar to the one shown in Figure 6.5.

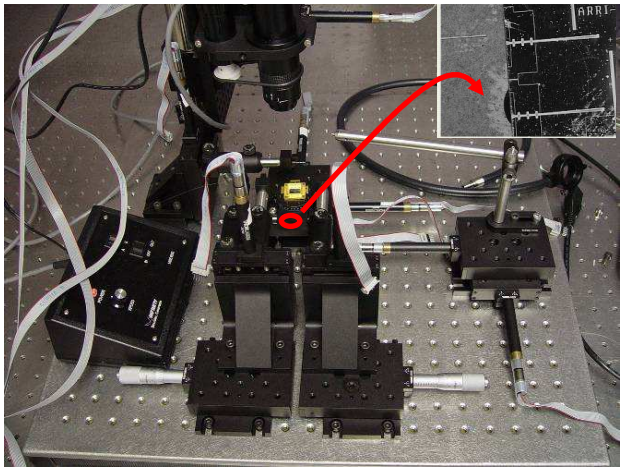

Figure 6.5 Experimental setup consisting of computer controlled microstages used for fiber alignment and insertion for fiber-to-carrier attachment.

Following the fiber insertion, fluxless attachment of the fiber-to-carrier is executed via laser heating. The carrier is fitted with a solder preform guide similar to one shown Figure 6.6 that prevents the solder from falling on its side during heating.

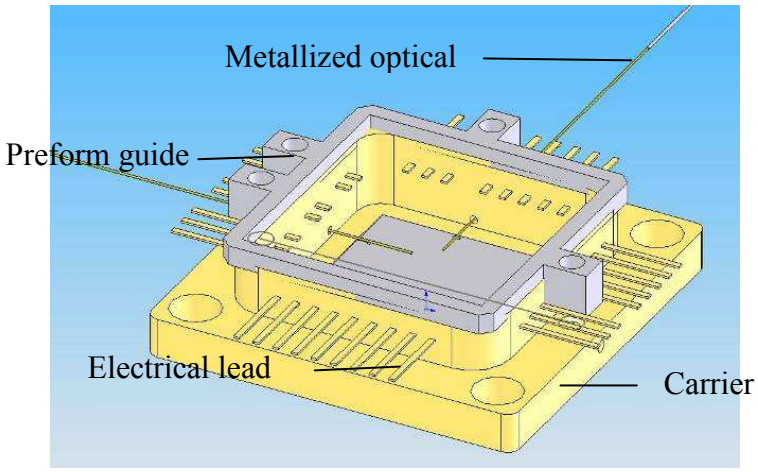

Figure 6.6 Schematics showing the carrier, metallized optical fibers, electrical leads exiting the carrier side walls, and solder preform guide for smooth solder feeding during fiber-to-carrier attachment.

The first fiber is held by a fiber gripper mounted on motorized translational micro-stages, and then inserted into a feed-through hole of carrier and into a DRIE micro-machined trench on the MEMS die. Cleaned indium solder preform is then dropped through the solder guide attachment and finally, the laser power is applied at a predetermined location on the carrier to heat the package. The laser power and heating duration requirements for melting the indium solder were determined using FEA methods as described in Chapter 7. The laser soldering parameters used are laser power: 20W, heating duration: 45s, and oxygen level: less than 250 ppm.

The indium solder used was cleaned prior to use in acetone, 10% hydrochloric acid, DI water and isopropyl alcohol (IPA) to remove organics and surface oxides. While developing the fluxless soldering technique used for the fiber-to-carrier attachment, we investigated the effect of oxygen-free soldering environment on fluxless soldering. The soldering gas environments used are industrial and ultra pure grade nitrogen and 95%Ni-5%H_2 gas mixtures.

6.1.4.4 Carrier Lid Sealing

The provision of adequate sealing is a big challenge in MEMS devices requiring hermetic packaging because of the need to provide electrical and optical interconnection paths to the device across the sealed boundary. The final packaging operation for our device is the package lid sealing for carrier-level hermetic packaging of the device using Miyachi Unitek's SM8500 parallel seam sealing system located at BMC's class 10000 cleanroom facility and shown in Figure 6.7.

Figure 6.7 Miyachi Unitek's SM8500 parallel seam sealing system.

To achieve the seal, a continuous train of energy (heat) pulses is delivered to the package while the package moves underneath a stationary electrode roller at a steady speed. The energy pulses and package speed are such that each nugget produced on the package is wide enough to overlap with the next. This is performed in a chamber that is continuously purged with nitrogen gas to maintain low oxygen and moisture levels. The key process parameters for the lid seal operation are the power, electrode force and travel speed while the sealed package obtained is shown in Fig. 6.8.

Figure 6.8 Sealed carrier package.

6.2 Die/Wafer Level MOEMS Switch

6.2.1 Description of Die/Wafer Level MOEMS Switch

In this section, we describe our second application device (die level MOEMS switch). For this device, hermetic sealing is achieved at the die/wafer level instead of at

the carrier level in the case described in section 6.1. Figure 6.9 shows the schematics of the application device for hermetic die/wafer level sealing. This consists of a lower silicon die (MEMS Si die) and an upper glass die (cap chip) to be bonded and sealed hermetically.

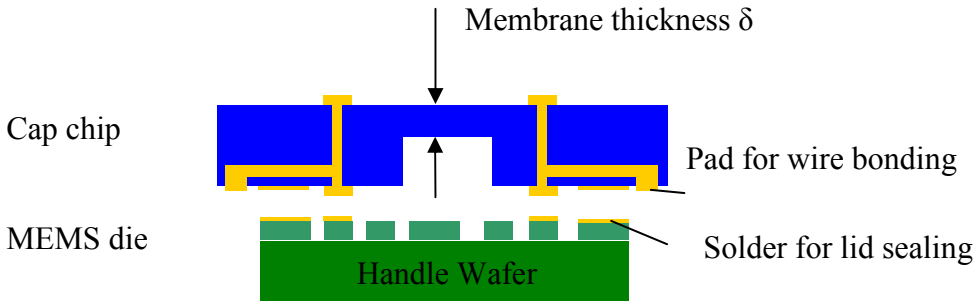

Figure 6.9 Schematics of Dies for Sealing Process
(diagram courtesy of Dan Jean and Michael Deeds).

Each bonding pair consists of a Si bottom die and a Pyrex glass top chip with solder material deposited around the square perimeter of the top chip for bonding and hermetic sealing purpose. In an actual device, the bottom silicon chip carries the MEMS device, while the top glass chip (cap chip) acts as the device lid. The test vehicles consist of Silicon on Insulator (SOI) bottom dies and Pyrex glass cap chips with solder metal patterned along the perimeter as shown in Figure 6.10. The solder sealing ring widths for the hermetic sealing were 0.5 to 2.0 mm and the interconnect dimensions for electrical testing, from 40 μm to 240 μm.

Since hermeticity is achieved at the die level, it is important that leak testing methodology be incorporated to the MEMS die design. The hermeticity of this device may be determined by observing the deflection of the cap chip membrane due to test chamber pressure modulation in an optical leak tester. The membrane thickness δ is therefore critical and it is obtained using finite element analysis such that a lid deflection of about 5.6 μm due to a test chamber pressure of 1 bar is achieved during package hermeticity testing. The MEMS die-to-cap chip attachment process parameters in the case are: bonding pressure, reflow temperature, hold time, ramp up rate, ramp down rate, and cleaning method.

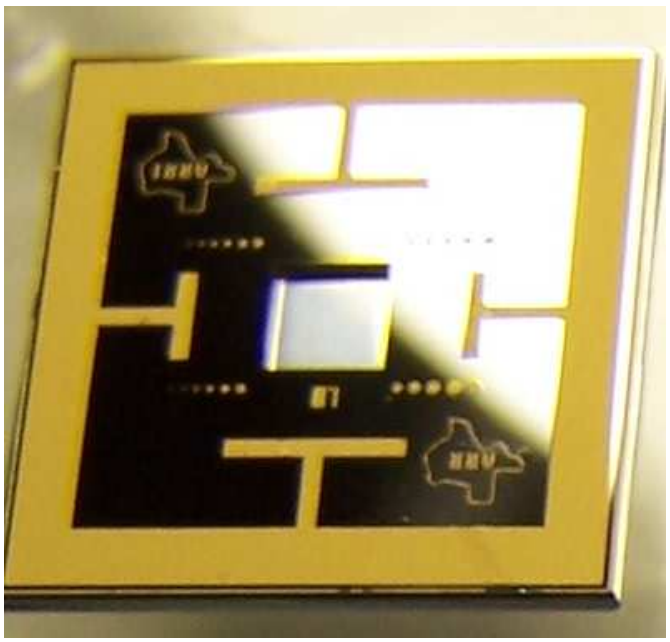

Figure 6.10 Cap chip for MEMS die-to-Cap chip sealing showing solder metal along the die perimeter and pads for electrical interconnection.

6.2.2 Fabrication Process for Test Vehicle Chips

The test vehicles used for the work described in this section were fabricated at Stanford Nanofabricaion Facility. The fabrication steps for the test vehicles used for the bottom die of the die level MOEMS switch are as follows:

- A layer of 7 μm thick Shipley SPR220-7 photoresist is spin coated, exposed, and developed to define the regions for base metal and solder metal deposition on a 4inch silicon or Pyrex wafer.
- A tri-layer metal deposition of 1000Å each titanium (Ti), platinum (Pt) and gold (Au) forms the forms the base metal. A thick layer of approximately 5μm thick solder, either as alternating layer of tin (Sn) and gold (Au), or 80%Au-20%Sn alloy is deposited using sputter deposition. A solvent liftoff leaves behind silicon/pyrex wafers with regions containing base metal and solder.

The fabrication steps for the test vehicles used for the top cap chip of the die level MOEMS switch are as follows:

- A layer of 7 micron thick Shipley SPR220-7 photoresist is spin coated, exposed, developed and baked to define the regions for DRIE on a 4inch silicon wafer.
- This patterned wafer then undergoes standard Bosch® process to etch 350 μm of silicon. RF plasma is used to strip the photoresist.

A second layer of 10 μm thick photoresist is spin coated, exposed and developed, leaving out regions for base metal deposition.

- A tri- layer base metal consisting of 1000Å each of Ti, Pt and Au is deposited using sputter deposition. A solvent liftoff leaves behind silicon wafer with DRIE structures and base metal.

In addition to specimens designed for sealing purpose, test vehicles were also designed and fabricated for electrical interconnections. Solder pads ranging in size from 10μm – 90μm were deposited on both the bottom MEMS dies and the top cap chips to form vertical electrical interconnections between the bonded. The bottom MEMS die provides a path for connecting the interconnection pads to contact pads for electrical continuity and resistance measurements.

6.2.3 MEMS Die-to-Cap Chip Attachment Process

This section summarizes experiments for the development of MEMS die-to-cap chip sealing and electrical interconnections for die level hermetic packaging of this device. A Laurier® M9 Flip chip bonder located at ARRI's Texas MicroFactory™ was used for the MEMS die-to-cap chip bonding. With this equipment, we were able to ensure tight control of the attachment process variables (e.g. bonding pressure, reflow temperature, and heating rates). The lower and upper bounds for the process parameters were based on the several factors including results obtained from prior experiments, information from literatures and vendors. The summary of the bonding process variables used are shown in Table 6.3. These process variables are the bonding pressure, X_1, peak bonding reflow temperature, X_2, and the hold time at the peak bonding temperature, X_3. Using the die bond strength as the response output, experiments were constructed to determine which process variables affects the bond strength the most,

and also obtain a linear regression model expressing the response variables to the input variables as discussed in Chapter 8.

Table 6.3 Summary of die sealing process parameter.

Process Parameter or Factor	Low Value	High Value
Peak Bonding Temperature (X_1)	320 (^oC)	340 (^oC)
Bonding Pressure (X_2)	50 Psi	300Psi
Hold Time at Peak Bonding Temperature (X_3)	5 min	20 min

6.3 Implantable In-Plane Micropump

In this section, we discuss packaging aspects related to a MEMS-based implantable drug delivery system (IDDS) for medical applications. This device is intended for the precise dispensing of drug dosages over time, as it is often necessary in the treatment of cancer.

6.3.1 Description of Micropump

The key elements that constitute the microactuator for this micropump are voltage pads, V-shaped chevron beams and a center shaft connected to the diaphragm through lever mechanism for stroke amplification as shown in Figure 6.111. The microactuator consists of six chevron beams on either side of the center shaft. The beams are 1200 μm in length with a cross sectional area of 12μm x100μm and a rib angle of 5.7^o. The pump diaphragm is 750μm in length, 100μm in height and 50μm wide. It also consists of 2000μm x100μm x100 μm (length x width x height) fluidic

channel along with a nozzle/diffuser arrangement for flow rectification. The dimensions are based upon detailed optimization studies [114-116].

The electrothermal actuator for this micropump is fabricated using a 500 micron thick SOI (silicon on insulator) wafer. A picture of fabricated substrates and Level-0 packaged prototypes are shown in Figure 6.12.

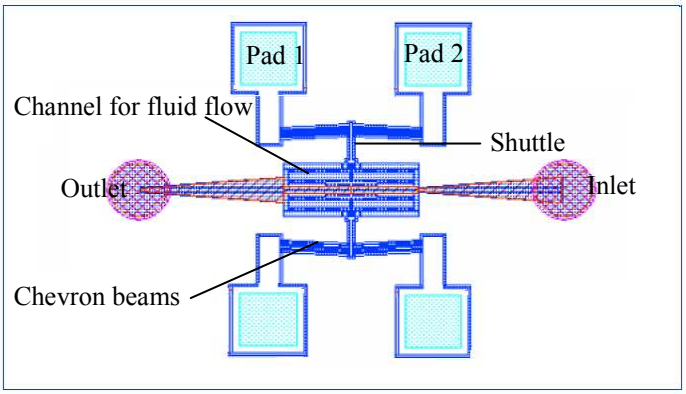

Figure 6.11 SOI MEMS layout of the in-plane pump [117].

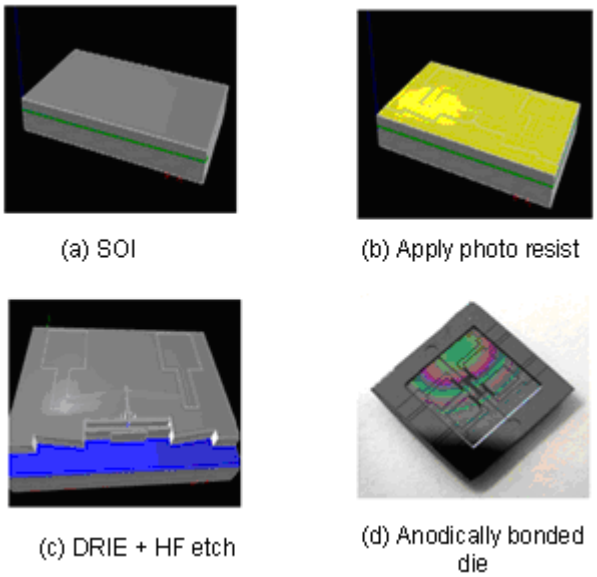

Figure 6.12 Fabricated SOI in-plane micropump, and a description of Fabrication and Level 0 Packaging steps [117].

In contrast to traditional peristaltic micropump designs, which use an out-of plane pumping diaphragm, the in-plane pump consists of the actuators, diaphragms, reservoir and I/O fluidic valves fabricated on a single layer. Joule heating of the V-beams and lever mechanism amplifies the stroke of the pump. The fluidic path is enclosed by anodic bonding of a Pyrex™ glass to the pump die, and the overall fabricated mask layout is shown in Figure 6.12. The targeted adjustable pump rate is 1-100 μl/min, but exact design values for prostate cancer will be determined as an outcome of a separate research work that studies the relationship between drug release rate, tumor oxygen levels and therapeutic outcome.

In addition to the MEMS die enclosed by Pyrex (Level 0 package), the pump must also be interconnected with electronics, power, and RF communication from inside the body. There are multiple levels of packaging, starting from Level 0 (SOI MEMS+Anodic Bonding of Pyrex), Level 1 (enclosing the pump inside a carrier, and providing appropriate fluidic and electrical interconnects), and Level 2 (adding electronics, power, and a reservoir).

6.3.2 Packaging of the micropump

In order to enhance the reliability of the micropump, the MEMS devices must be packaged appropriately. For the micropump, packaging provides electrical and fluidic interconnection paths; it provides a platform for component mounting and also protects the device from external damage caused by contamination, moisture and handling. It also ensures that adequate thermal solution is provided for heat removal. This is especially important for the IDDS because the surrounding temperature is

expected to heat up no more than 4°C. Equally important is ensuring hermetic packaging of the micro-pump to prevent drug leakage, and also, the choice of materials that ensure bio-compatibility.

Packaging consists of anodic bonding of the micro-pump die and a cap chip, attachment of the bonded dies to a 1mm thick Kovar plate of dimensions 1500x1500μm^2 via a 1mil thick thermal interface material (TIM). Wire bonding is used to provide electrical connections for the MEMS die. Lastly, the whole structure is sealed with Kovar metal cap. The schematic of the next packaging level for the die (Level 1) is shown in Figure 6.13.

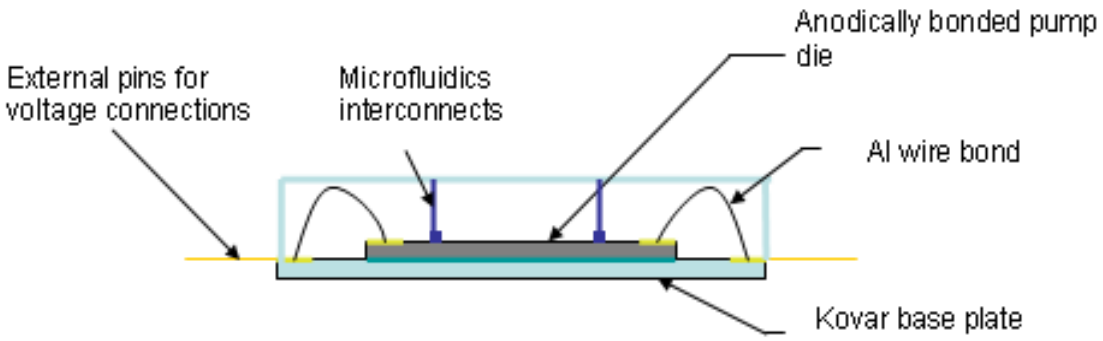

Figure 6.13 Schematic representation of the packaged pump die (Level 1 packaging) [117].

6.3.2.1 Level 0 Micropump Packaging

The first level of micropump packaging is done using anodic bonding of the MEMS die with a Pyrex glass chip. This ensures that the fluidic pathways in the pump are created. The technique of bonding silicon and glass under the influence of temperature and voltage is known as anodic bonding. The formation of the bond

involves the displacement of the sodium ions in glass by the applied field forming a depletion region at the surface. This highly reactive surface forms a strong chemical bond with the silicon. Anodic bonding requires very smooth and flat surfaces for bonding. It is also sensitive to contamination. The process conditions are temperature in the range of 200-500^{o} C and voltage of 700-1.5kV. The bond strength is affected by voids or bubbles formed during the bonding process. It has been determined that the bonding temperature plays a critical role in bonding. Bonding time, potential and load contribute weakly to the bonding strength but are key factors in influencing the speed of bond formation and the area bonded. The anodic bonding set up in our lab involves a hot plate, a pressure fixture and a high voltage source. Experiments were conducted to determine optimal process parameters, and an acceptable process window was found. The conditions for anodic bonding were temperature of 300-500 °C, and Voltage of 1-1.5 kV for 20-25 minutes, at low or no bonding force. The current flowing through the bonded region was monitored throughout the process and was found to be in the range of 9-20mA. The setup and bonded micropump dies are shown in Figure 6.14. In order to provide means for the interconnect through the Pyrex glass of 500 μm in thickness, holes were drilled in the Pyrex die prior to anodic bonding using diamond drill bits 650 μm in diameter to create holes in the range of 700-900 μm at a drill speed of 45,000 rpm. Experiments were conducted to determine acceptable micro drill process parameters and characterize the results. The drilling setup and resulting interconnect holes are shown in Figure 6.15.

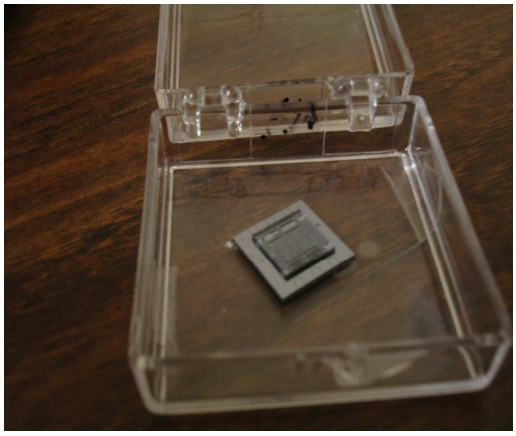

Figure 6.14 Anodic bonded samples to form the pumping chamber between SOI and Pyrex dies [117].

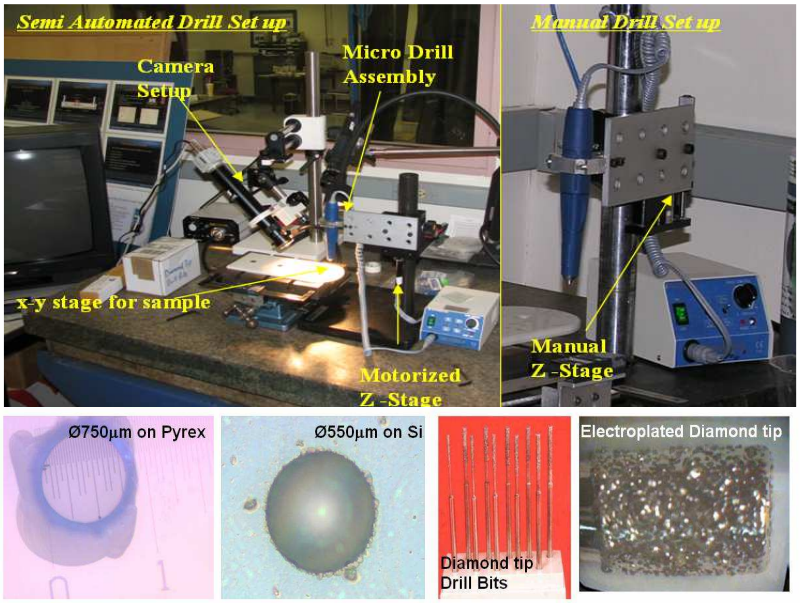

Figure 6.15 Pyrex micro drilling station and optical measurement of interconnect holes using a Veeco NT1100 surface profiler [118].

Finally, the fluidic path inside the pump must be contained inside the MEMS device. The SOI MEMS contains 2µm leak paths below and above the moving diaphragm in order to actuate, and therefore, it is necessary to contain the fluid flow

using a compliant polymeric membrane implemented in the shape of a tube. In order to achieve this, it was proposed that a tube made of Parylene should be embedded in the channel connecting the inlet and outlet of the micropump. The Parylene tube would be in contact with the diaphragm of the pump enabling the pumping of the fluid in the channel contained within the tube. The schematic drawing of the Parylene tube embedded in-plane micropump is as shown in Figure 6.16.

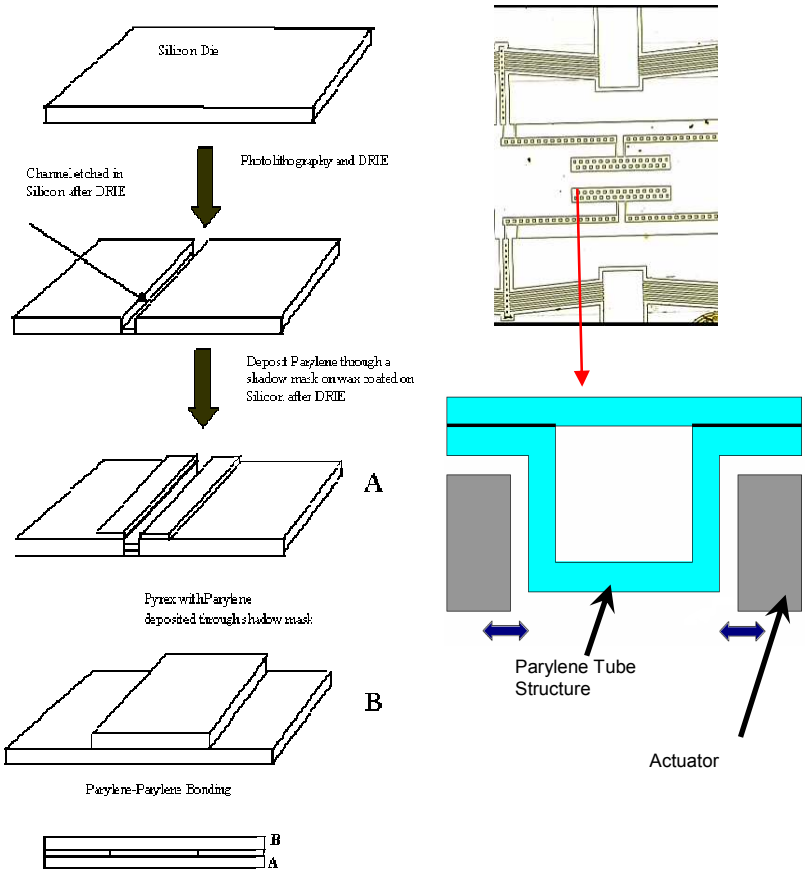

Figure 6.16 Schematic cross section of a Parylene tube inside the pumping chamber, and fabrication process [117, 119].

The process of forming the Parylene-Parylene bond is followed by dissolving the molding wax in Toluene to form the tube structure on the Pyrex. This is then aligned and anodically bonded to the SOI micropump die.

6.3.2.2 Level 1 Micropump Packaging

For obtaining a package similar to the diagram in Figure 3, fluidic and electrical interconnects must be fabricated. Fluidic interconnects out of the pumping plane are formed by using PEEK or glass capillary tubes with Silicone tubing. These are bonded to the Pyrex using a fast curing epoxy as shown in Figure 6.17. In addition, the die stack must be placed inside a carrier package. Because the actuation principle we use is based on a thermal MEMS drive, it is important to study the effects of heat dissipation in order to design the thermal mass of the package and ensure that during device implantation tissues are not exposed to more than 4 °C temperature increases.

Figure 6.17 Fluidic interconnects on the anodic bonded micropump die [119].

In this thesis, we carried out Level 1 Package thermal analysis using in-depth numerical analysis. This was performed in order to determine the impact of each variable (air gap, voltage etc) on the maximum device temperature. Analysis was performed using ANSYS® and the results presented in Chapter 7. In order to ensure package hermetic sealing and thus prevent medication leakage to the body system, brazing technology is used to attach the carried and the lid.

CHAPTER 7

PACKAGE DESIGN USING FEA AND REDUCED ORDER MODELING

7.1 Analysis of Laser Heating

Laser soldering offers the advantages of localized and non-contact heating. Because of the typically lower heating fluxes and the smaller heat affected zone involved (compared to welding), induced thermal stresses are generally not a concern with laser soldering. The optical fiber-to-carrier attachment process for our carrier-level MOEMS switch was done via laser soldering. One important motivation for using a laser for this process is the non-contact and localized heating nature of laser soldering.

Simulation (using ANSYS®) and experimental results indicate that modifications to the carrier design, heating method and carrier surface are necessary in order to reach indium reflow temperatures using a 40 W semiconductor diode laser heat source. The changes considered include:

- Pre-heating the carrier.
- Reducing the gold layer thickness.
- Modifying the package geometry to isolate the area to be locally heated.
- Modify the surface of the carrier with the goal of increasing its laser absorption.

In order to simplify the laser soldering process, substrate pre-heat is sometimes necessary to prevent the "heat sink" effect of the substrate. Pre-heating of the substrate would reduce the power requirements of the laser and also the temperature gradients in the package during soldering. This is especially important in the case of a gold substrate considering that the absorptivity of gold is low in the near infra red wavelength range of diode lasers. However, pre-heating requires extra tooling and could also lead to die shift due to reflow of already assembled MEMS die and cap chip. Reducing the gold layer thickness below the current 0.5 micron thickness could also compromise the corrosion protection offered by the gold layer. The purpose of the surface modification is to improve laser absorption into the carrier surface. The purpose of the geometry modification is to localize the heating effect of the laser by creating resistance path to the carrier heat diffusion.

At the diode laser operating wavelength, the reflectivity of gold is around 97.5% [120]. We used the combination of experimentation and numerical simulation to verify this value. This technique was also used to determine the reflectivity of black spot material used to modify the reflectivity of the carrier surface. Additionally, we used finite element (FE) simulations to evaluate the effect of changing the carrier geometry and surface material property (by increasing the laser absorption of the carrier surface) on the heat distribution on the package.

This chapter discusses the following four issues relating to the attachment of gold coated optical fibers to gold coated Kovar carrier housing for MEMS packaging.

- Optical absorption by a gold surface.

- Effect of surface modification.
- Effect of geometry modification.
- Effect of concurrent surface and geometry modifications.

7.1.1 Optical Absorption by Gold Surface

An inverse thermal analysis technique was employed to estimate the optical absorption of the diode laser (wavelength ~ 860nm) used for the optical fiber-to-carrier attachment. An inverse solution is used if a portion of the information (e.g. boundary condition, initial condition, source term or material properties) necessary to completely define a problem is not available [121-122]. In this case, the source term is missing since we want to determine the reflectivity and hence the power absorbed by the gold coated carrier package. In order to solve the inverse thermal problem, additional conditions such as the temperature at specified locations need are needed.

In determining the laser absorption of the gold coating on the carrier package, it is assumed the carrier material is opaque such that the incident radiation is either absorbed or reflected from the surface. To determine the laser absorption of the gold surface, laser radiation of known intensity was directed on the gold surface and the temperature response at certain nodes away from the laser beam spot measured at 5 seconds time interval for 90-120 seconds using a thermocouple.

The numerical analysis software ANSYS® was then used to construct a FE thermal model of the problem. Some of the small geometrical features on the carrier were simplified to avoid meshing problems. SOLID70, a 3-D solid element with a

single degree of freedom per node (temperature) was used. Figure 7.1 shows the ANSYS® thermal models used for this analysis.

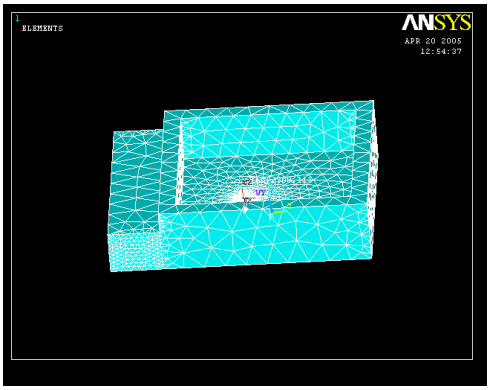

(a)

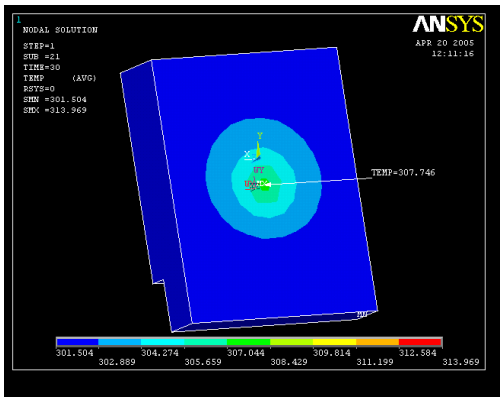

(b)

Figure 7.1 Models for obtaining diode laser reflection on gold surface
(a) meshed model and (b) thermal model.

The constant temperature material properties used are [123]: density = 8100 kg/m^3, thermal conductivity = 17 W/m-K, and specific heat = 460 J/kg-K. Adiabatic boundary conditions are applied to the bottom surface of the carrier package and

thermal heat flux applied on the laser heating spot. The rest of the surfaces of the carrier package are kept at natural convective boundary conditions of 10 W/m^2K. The surrounding ambient was kept at 296.3K. Heat flux was applied for a duration of 90 seconds.

This thermal model was used to obtain the laser intensity that will bring the material to the measured temperature values. We note here that the laser power obtained in ANSYS® has taken the surface absorptivity of the laser into account. Therefore, the ratio of intensities (i.e. the intensity obtained from ANSYS® and the intensity from the experimental set up), gives the absorptivity of the gold surface. This method works particularly well for materials that have low absorptivity values (such as gold at low laser power) because the surface temperature is small. At high temperatures, the absorptivity increases and may not be assumed to be constant.

In order to verify the consistency of this method, several experiments were conducted using different power intensities (8, 10, and 12 W) and the average 2.5% value obtained agrees with the literature [120]. Sample experimental data for the temperature response at a particular location on the package as measured by a thermocouple and the laser power density directed at the package is shown in Table 7.1. The table also shows the power density that will yield the same temperature response at that same location as predicted by ANSYS®.

7.1.2 Package Heat Distribution

Once the laser absorptivity on the carrier was determined, we modeled the laser heating of the carrier in order to estimate the power and heating duration necessary for

solder reflow. In order to determine optimal process parameters for laser soldering, detailed FEA thermal analysis simulation models were constructed for the package.

Table 7.1 Experimental and simulation results for laser reflection on gold surface.

	Experimental Data	Simulation results	Experimental Data	Simulation results	Experimental data	Simulation results
Initial temp	23.3	23.3	23.3	23.3	23.3	23.3
Final temp	34.5	34.75	32.8	32.84	30.9	30.93
Power	12W	12W	10W	10W	8W	8W
Heating time	30sec	30sec	30sec	30sec	30sec	30sec
Power density (W/m^2)	$1.53x10^7$	$3.82\ x10^5$	$1.27x10^7$	$3.18\ x10^5$	$1.02x10^7$	$2.55\ x10^5$
Absorptivity	2.497%		2.504%		2.5%	

Figure 7.2 shows the ANSYS® thermal model used for analyses presented in this section. This consists of a simplified geometry for the carrier that includes machined holes on the side wall for inserting fibers, holes on the top wall for feeding solder, and a laser heating spot on the top wall. Adiabatic boundary conditions are applied to the bottom surface of the carrier package and thermal heat flux applied on the laser heating spot. The rest of the surfaces of the carrier package are kept at natural convective boundary conditions. The surrounding ambient was kept at 296.3K. A heat flux equivalent to 40W laser power on 1.56mm spot size diameter was applied for duration of 10 seconds.

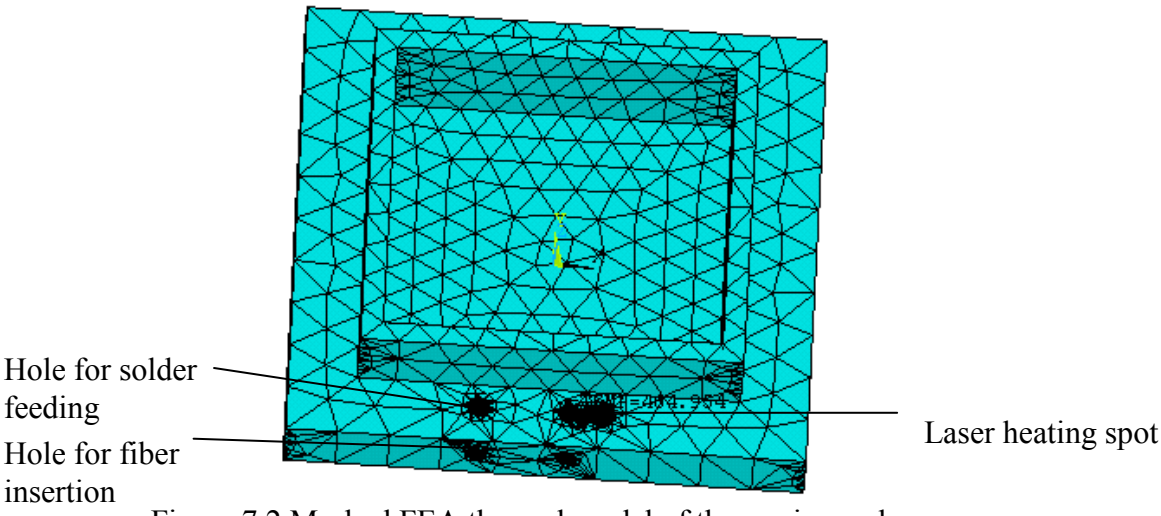

Figure 7.2 Meshed FEA thermal model of the carrier package.

The numerical simulation result shown in Figure 7.3 reveals that we cannot reach indium reflow temperature of 156^{o}C (~429K) using a 40W laser without surface and/or geometry modification to the package. We observe from this figure that the maximum temperature experienced by the carrier after 10s heating duration is 326K while the maximum temperature at the top carrier hole through which solder is inserted is merely 311K. We desire to have the temperature at this location be at least 470K in order to bring the solder to solution. We are therefore interested in determining the laser heating duration necessary to achieve the indium reflow temperature and the temperature induced at the nearest solder feed hole. The temperature at the nearest solder feedthrough hole must be kept below indium reflow temperature in order to ensure that the alignment of the fiber in the adjacent feedthrough is not compromised. The simulation results obtained with the geometry and surface modifications in place are shown in Figures 7.4 and 7.5. The surface modification consists of applying a black

spot on the surface of the package in order to increase laser absorption from 2.5% to 35%.

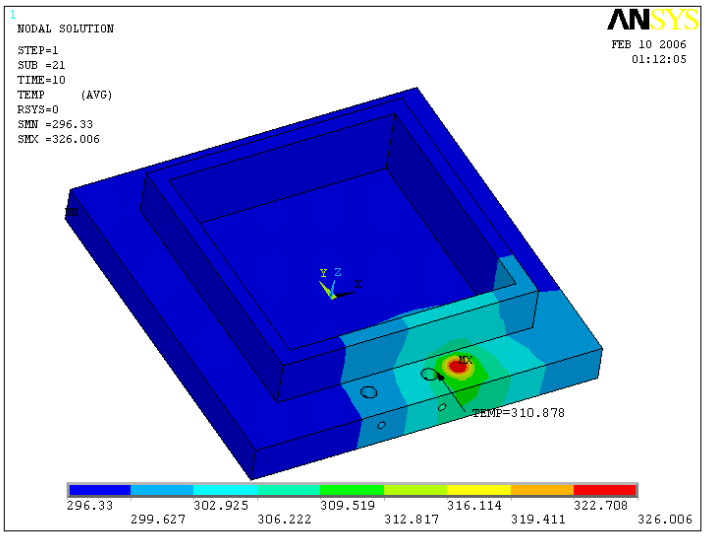

Figure 7.3 Temperature distribution in the Kovar carrier. Simulation conditions are 40 W power, 1.56 mm diameter spot size, 10 seconds heating duration and 2.5%.

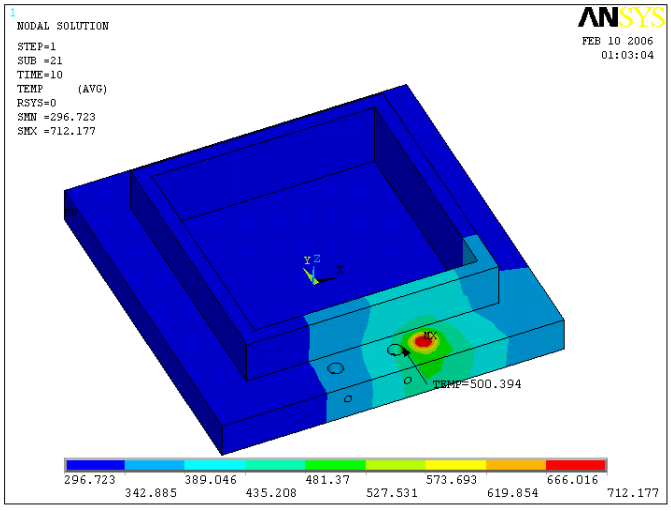

Figure 7.4 Temperature distribution in the carrier. Simulation conditions are 40W power, 1.56 mm diameter spot size, 10 seconds heating duration and 35% absorptivity.

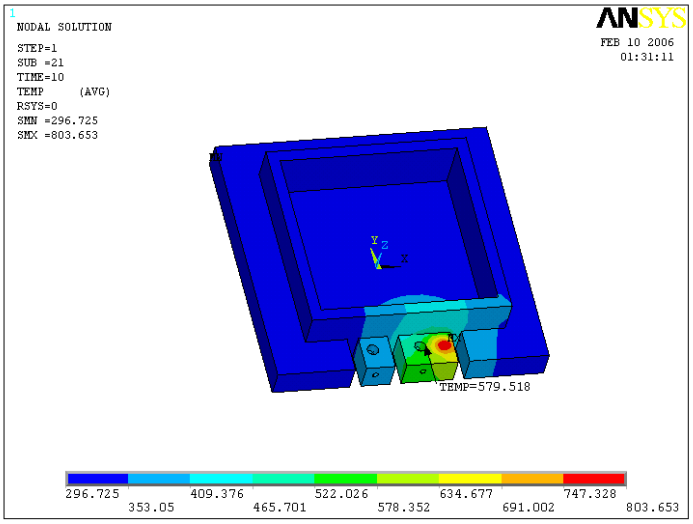

Figure 7.5 Effects of thermal isolation slot and absorptivity increase on temperature distribution in the Kovar® carrier. Simulation conditions are 40 W power, 1.56 mm diameter spot size, 10 seconds heating duration, and 35% absorptivity.

We note the effects of these modifications for a 40W laser power source as follows:

Effect of surface modification: By modifying only the package surface property, we increase the package temperature near the solder feed hole from 310.9K (37.9 ^{o}C) to 470.1K after 6.3s, and to 500K (227 ^{o}C) after a 10s heating duration. However, the adjacent solder feed hole is subjected to up to 347.2K (~74C) after 6.3s, and 372K (99C) after 10s as shown in Figure 7.6.

Effect of surface and geometry modifications: By modifying both the surface property and the surface geometry, we were able to increase the temperature of the solder feed hole to 470.1K after about 3s, and 579.5K (306.5 ^{o}C) after 10s. In this case however, the adjacent solder feed hole is subjected to up to 308K (~35C) after 3s, and 366K (93C) after 10s as shown in Figure 7.7.

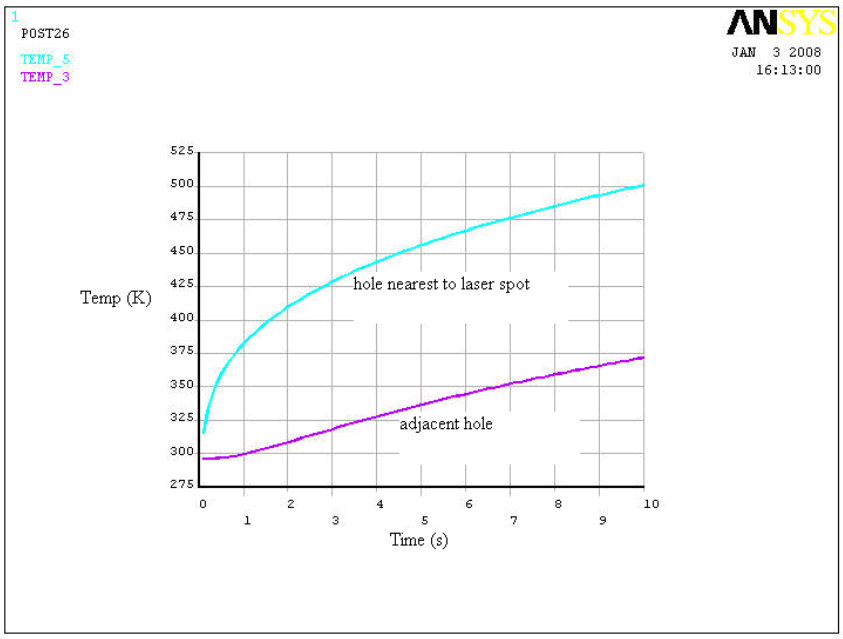

Figure 7.6 Effect of laser heating on adjacent carrier solder feed hole. Simulation condition is for 40W laser power, 1.56mm diameter spot size, and 35% laser absorption on carrier surface.

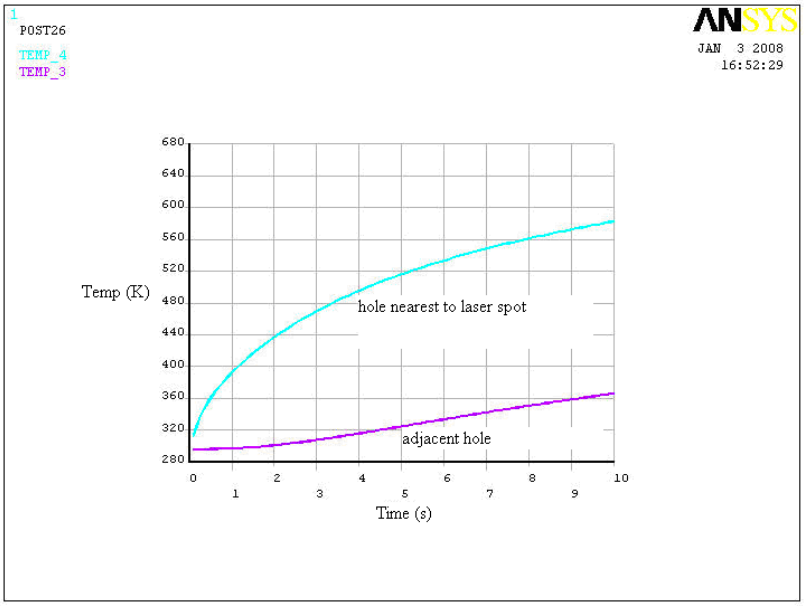

Figure 7.7 Effect of laser heating on adjacent carrier solder feed hole. Simulation condition is for 40W laser power, 1.56mm diameter spot size, and 35% laser absorption on carrier with geometry modification.

We observe in both cases that the temperatures obtained at the solder feed holes are well above the 429K (156 ^{o}C) liquidus temperature of indium, but in the second case, the necessary heating duration is reduced to 3 seconds instead of 6.3s. We ran this simulation for 10s in order to ensure that the solder is completed melted. We however note that at the 90 ^{o}C plus temperature of the adjacent solder feed hole, we run the risk of fiber shift by indium softening due to elevated temperature.

Figures 7.8 - 7.10 show simulation results for 20W laser power on 1mm spot size diameter. Results also indicate that we cannot reach the reflow temperature of indium solder without modifications similar to that described earlier.

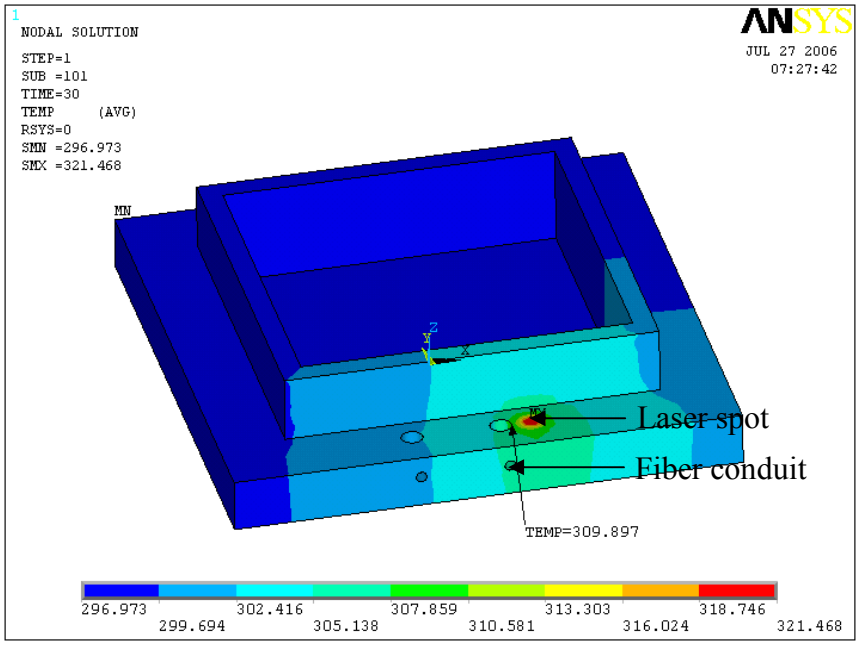

Figure 7.8 Temperature distribution in the Kovar carrier. Simulation conditions are 20 W power, 1 mm diameter spot size, 30 seconds heating duration and 2.5%.

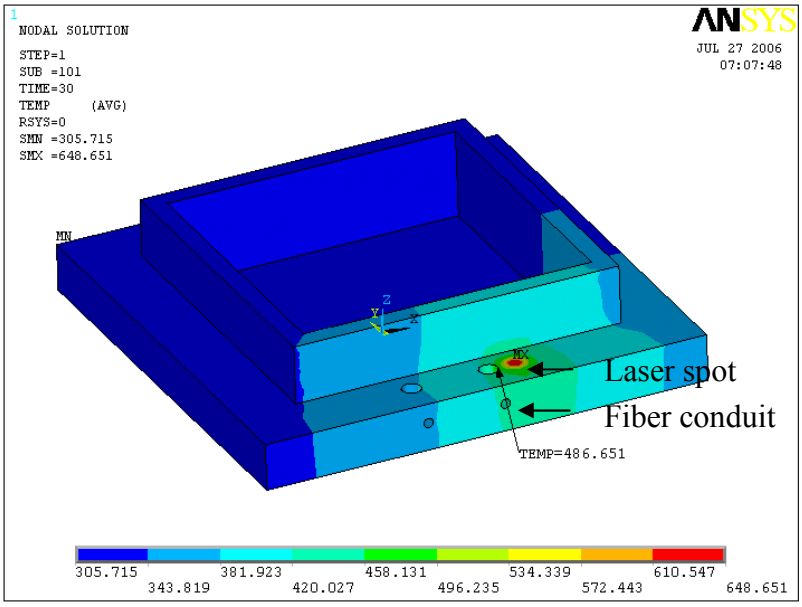

Figure 7.9 Temperature distribution in the Kovar® carrier. Simulation conditions are 20 W power, 1 mm diameter spot size, 30 seconds heating duration and 35% absorptivity.

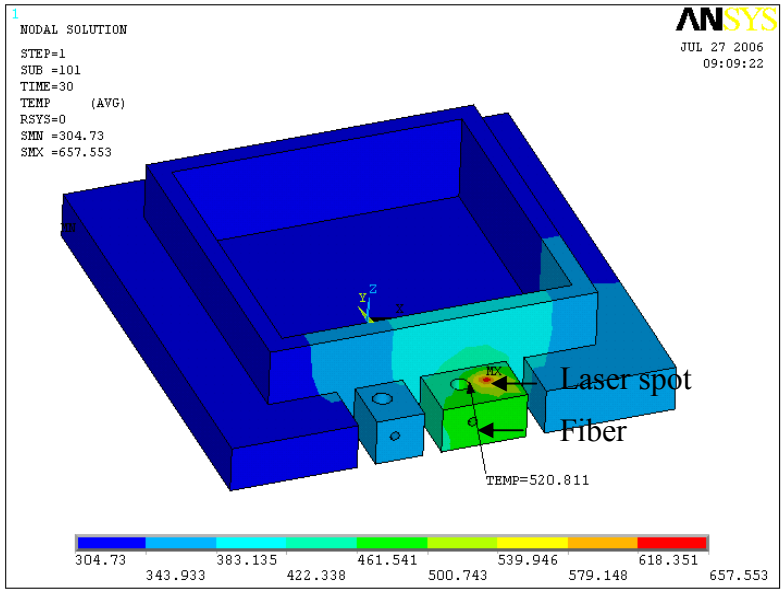

Figure 7.10 Effects of thermal isolation slot and absorptivity increase on temperature distribution in the Kovar® carrier. Simulation conditions are 20 W power, 1 mm diameter spot size, 30 seconds heating duration, and 35% absorptivity.

We note the effects of these modifications for a 20W laser power source as follows:

Effect of surface modification: By modifying only the package surface property, we are able to increase the package temperature near the solder feed hole from 310K (37^{o}C) to 470.1K after 22.3s, and to 487K (214 ^{o}C) after a 30s heating duration. However, the adjacent solder feed hole is subjected to up to 368K (~95C) after 22.3s, and 384K (111C) after 30s as shown in Figure 7.11.

Effect of surface and geometry modifications: By modifying both the surface property and the surface geometry, we were able to increase the temperature of the solder feed hole to 470K after about 10.6s, and 521 K (248 ^{o}C) after 30s. In this case however, the adjacent solder feed hole is subjected to up to 332K (59 C) after 10.6s, and 374 K (101C) after 30s as shown in Figure 7.12.

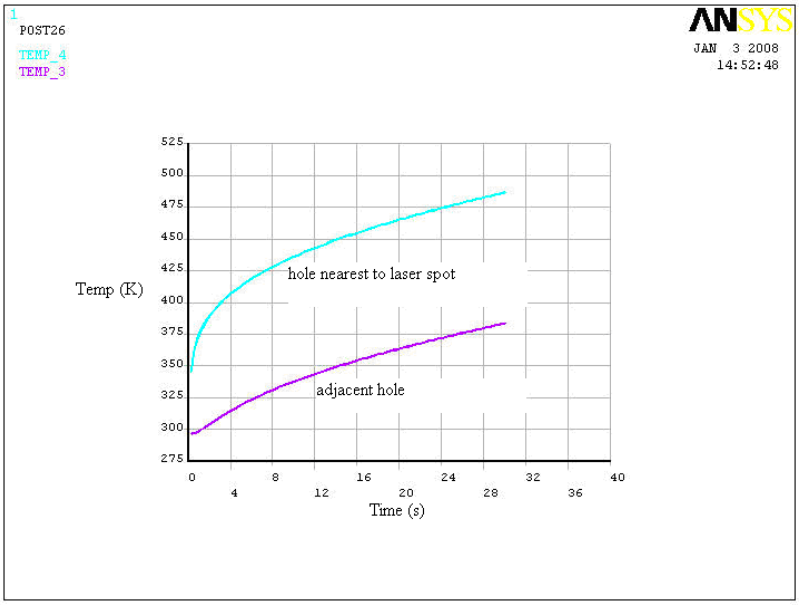

Figure 7.11 Effect of laser heating on adjacent carrier solder feed hole. Simulation condition is for 20W laser power, 1mm diameter spot size, and 35% laser absorption on carrier surface.

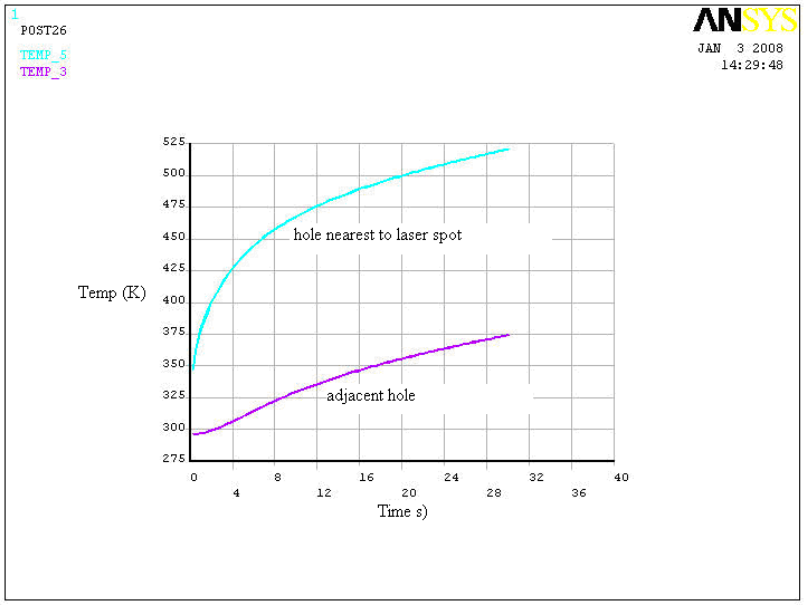

Figure 7.12 Effect of laser heating on adjacent carrier solder feed hole. Simulation condition is for 20W laser power, 1mm diameter spot size, and 35% laser absorption on carrier with geometry modification.

We observe in both cases that the temperatures obtained at the solder feed holes are well above the 429K (156 ^{o}C) liquidus temperature of indium, but in the second case, the necessary heating duration is reduced to 10.6 seconds instead of 22.3s. We ran this simulation for 30s in order to ensure that the solder is completed melted. We however note that at the 100 ^{o}C plus temperature of the adjacent solder feed hole, we run the risk of fiber shift due to elevated temperature.

Lastly, simulation results shown in Figure 7.13 also reveal that we cannot reach indium reflow temperature using a 12W laser power on 1 mm spot size diameter without surface and/or geometry modification to the package. Simulation results for these modifications are shown in Figures 7.14 and 7.15. The modifications consist of machining off part of the package in order to create resistance to the heat dissipation

path and increasing the surface absorption from 2.5% to 35% by applying a black paint spot on the surface of the package.

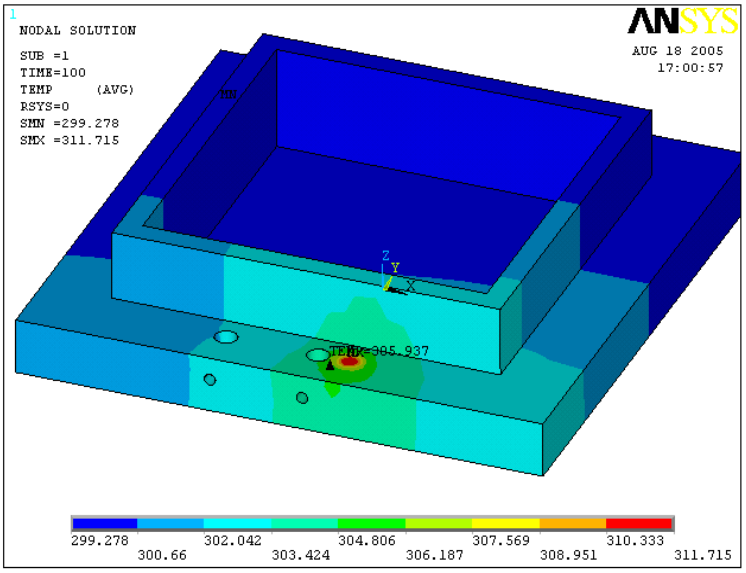

Figure 7.13 Temperature distribution in the kovar carrier. Simulation conditions are 12 W power, 1 mm diameter spot size, 100 seconds heating duration and 2.5%.

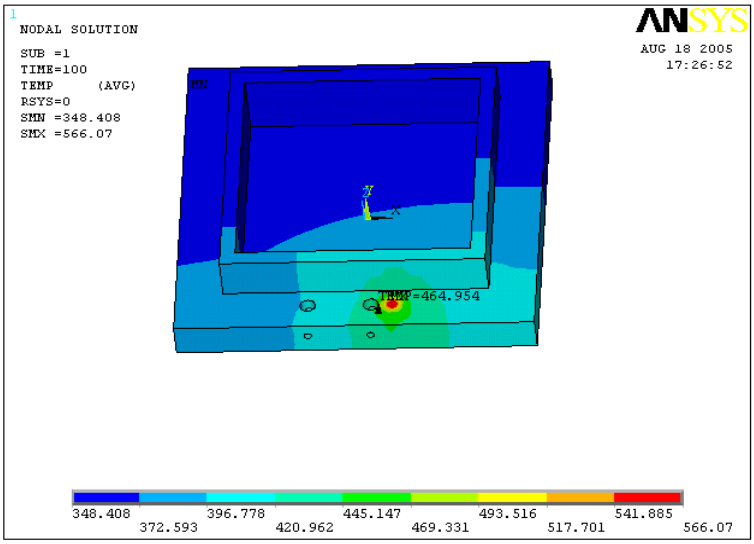

Figure 7.14 Temperature distribution in the Kovar® carrier. Simulation conditions are 12 W power, 1 mm diameter spot size, 100 seconds heating duration and 35% absorptivity.

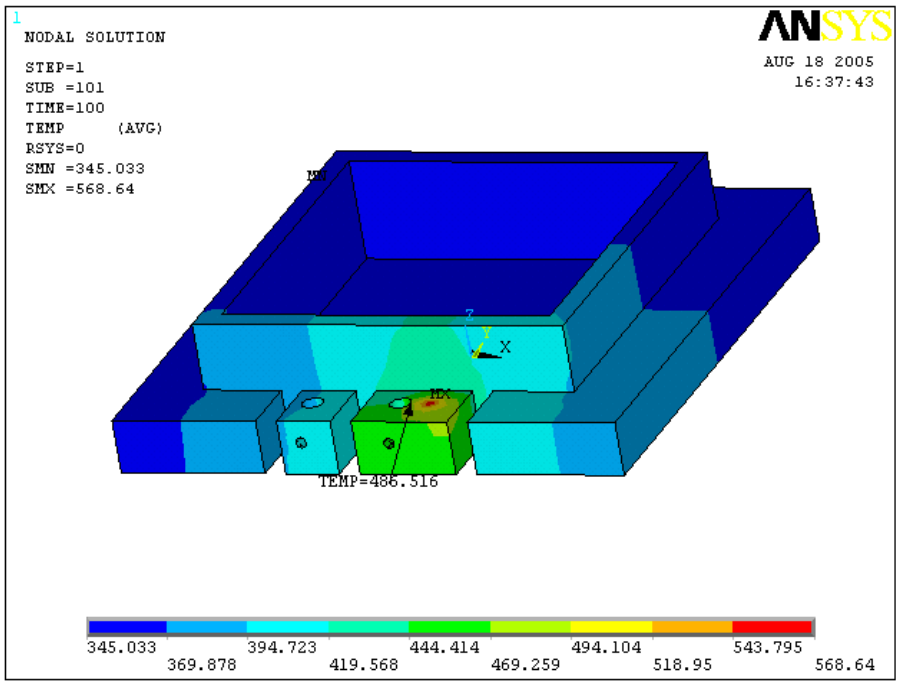

Figure 7.15 Effects of thermal isolation slot and absorptivity increase on temperature distribution in the Kovar® carrier. Simulation conditions are 12 W power, 1 mm diameter spot size, 100 seconds heating duration, and 35% absorptivity.

We note the effects of these modifications for a 12W laser power source as follows:

Effect of surface modification: By modifying only the package surface property, we increase the package temperature near the solder feed hole from 306K (33^{o}C) to 470.1K after 98.3s, and to 471K (198 ^{o}C) after a 100s heating duration. However, the adjacent solder feed hole is subjected to up to 408K (135 ^{o}C) after 98.3s, and 408K (135 ^{o}C) after 100s as shown in Figure 7.16.

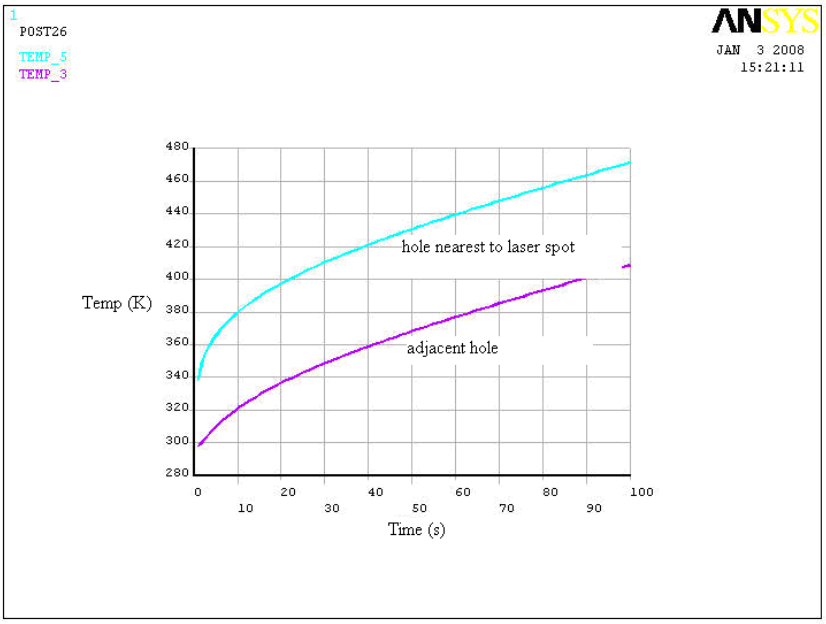

Figure 7.16 Effect of laser heating on adjacent carrier solder feed hole. Simulation condition is for 12W laser power, 1mm diameter spot size, and 35% laser absorption on carrier surface.

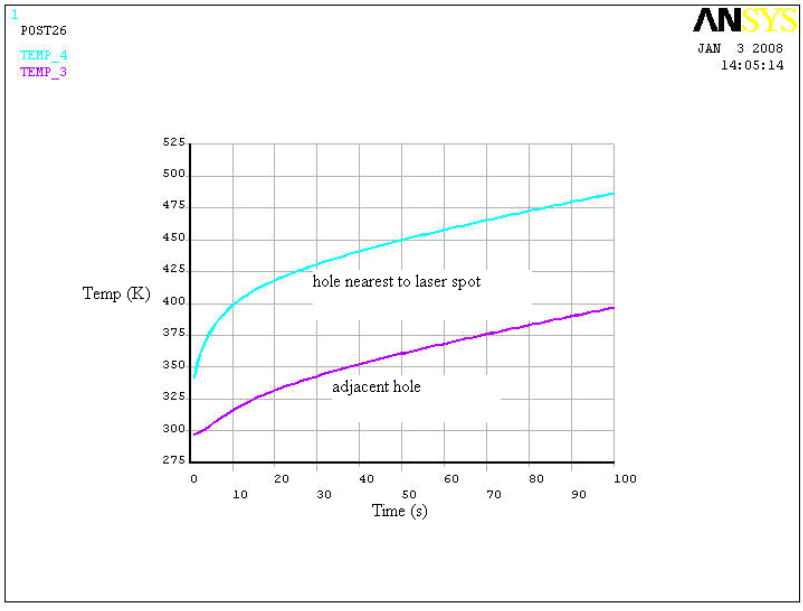

Figure 7.17 Effect of laser heating on adjacent carrier solder feed hole. Simulation condition is for12W laser power, 1mm diameter spot size, and 35% laser absorption on carrier with geometry modification.

Effect of surface and geometry modifications: By modifying both the surface property and the surface geometry, we were able to increase the temperature of the solder feed hole to 470K after about 77.3s, and 486K (213 ^{o}C) after 100s. In this case however, the adjacent solder feed hole is subjected to up to 378K (105 ^{o}C) after 77.3s, and 397K (124 ^{o}C) after 100s as shown in Figure 7.17.

We observe in both cases that the temperatures obtained at the solder feed holes are well above the 429K (156 ^{o}C) liquidus temperature of indium, but in the second case, the necessary heating duration is reduced to 77.3 seconds instead of 98.3s. We ran this simulation for 100s in order to ensure that the solder is completed melted. We however note that at the 120 ^{o}C plus temperature of the adjacent solder feed hole, we run the risk of fiber shift due to elevated temperature.

7.2 Modeling of Packaged Micropump

In this section, we describe the use of FEA and reduced order modeling in the package design of the implantable in-plane micropump introduced in section 6.3. This micropump is fabricated on a SOI wafer by DRIE micromachining, and has several advantages over conventional "out-of-plane" micropumps, including ease of fabrication, consistent geometry, and ease of assembly. Fluid flow is obtained via a pumping chamber displaced by a pair of electrothermal MEMS Chevron actuators. In order to implant this IDDS, an appropriate package must be designed. Numerical simulation has been used to study the influence of package design and materials on the heat dissipation of the micropump. We show that packaging greatly influences the micropump performance, and therefore design optimization of the package is necessary. As an aid

in design, we used reduced-order lumped and FEA model approximation. This model is accurate enough to capture the heat dissipation trends in the IDDS within 6%, however, it only requires fraction of simulation resources when compared to a full fledged FEA analysis. The reduced order model is then used to modify the package materials and geometry in order to ensure a safe operating temperature for an implanted micropump in the human body. This approach can be used for the analysis of packaged electrothermal MEMS actuators in general.

7.2.1 Description of Models

From an electro-thermo-structural-flow standpoint, we describe here several micropump models used to study the thermal dissipation during operation:

- **micro-model:** this model consists of detailed microactuator model with the rest of the SOI device and handle layers, and 2 μm air gap layers beneath and above the microactuator. This is a thermo-structural model.
- **complete model:** this model consists of detailed microactuator model with diaphragm, handle layer, top cap chip, air gap layers below and above the microactuator, Kovar based carrier, and lid. This is a thermo-structural model.
- **macro-model:** this model consists of a simplified approximate geometry of the microactuator with the rest of the device and handle layers, Kovar carrier with lid, a top cap chip above the microactuator, and 2 μm air gap layers beneath and above the microactuator. This is a thermal model.

- **implanted macro-model:** this model is the same as the previous one, but it also contains a model of the surrounding human tissue when the device is implanted. This is a thermal model.
- **lumped flow model:** this model is an approximation of the pumping mechanism in order to estimate the fluid flow generated by the pump. This is a structural-flow model.

7.2.2 Methodology for Package-Level Characterization of Micropump

Analytical solutions to complex thermal and structural problems are often lacking, making numerical approaches to solving these problems very attractive. However, the numerical solution approach to solving near exact or detailed physical models at the package or system level using commercial numerical codes such as ANSYS® is difficult for several reasons. First, there is usually a limitation of large numbers of nodes or elements that can be generated using these codes; and secondly, even if there is no limitation on the nodes/elements, the computational time required to solve multiphysics problems is often prohibitive. In this dissertation, we demonstrate the use of several simplification methods (lumped or compact modeling, model symmetry, and decoupling of physics) in analyzing the electrothermomechanical performance of packaged micropump. A flow chart of the methodology used in this work is presented in Figure 7.18 while the methodology is described fully later in this section.

The method for analyzing this highly complex problem consists of the following steps:

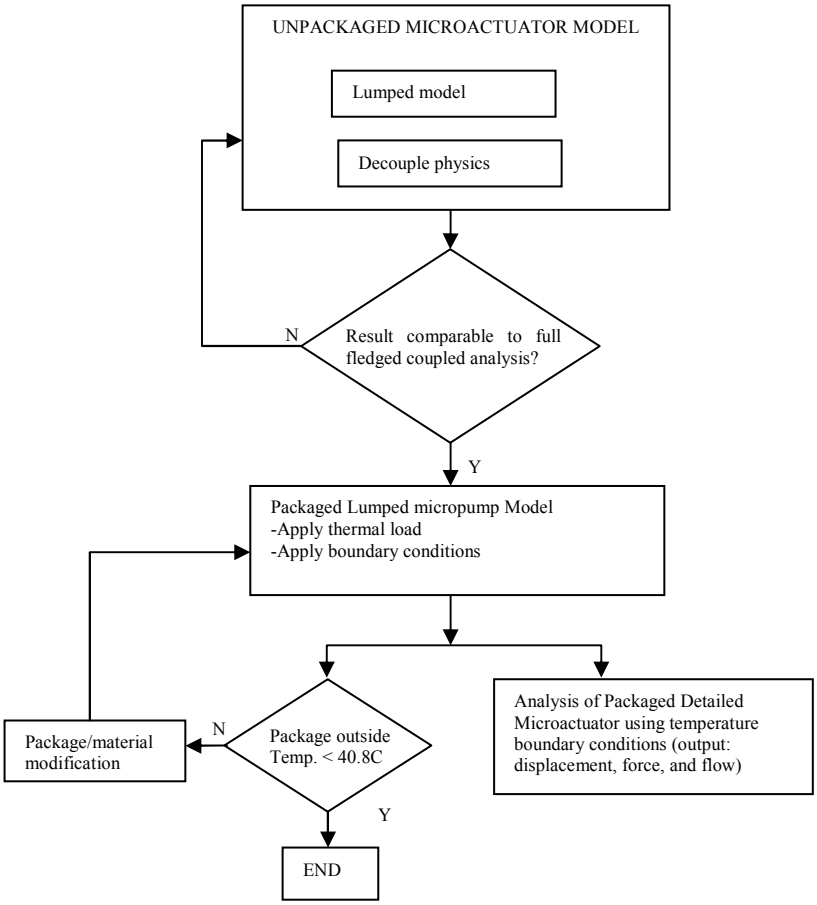

Figure 7.18 Schematic representation of the methodology for micropump thermal, displacement, and flow characterization.

Step 1: Obtain a purely thermal model of the microactuator

We proceeded with the analysis by performing electro-thermal analysis of the micropump's microactuator, including the following steps:

- Simplify micro-actuator model by collapsing chevron beams into a lumped geometry with same resistance as the overall resistance of the detailed microactuator model.

- Simplify model physics by applying heat generation (or heat flux) on actuator beam instead of voltage, thereby decoupling the physics.
- Compare thermal result with full fledged coupled electro-thermal and determine the error.
- Repeat 1-4 using different boundary conditions (BC) combinations to ensure that method yields consistently accurate results.

During this step, we eliminate the need for electro-thermal analysis on a detailed micro-model, by replacing it with a purely thermal load via Joule heating, and a simplified geometry of the micropump.

Step 2: Create a detailed, complete model of the packaged micropump with thermal load and boundary conditions only.

After eliminating the need for electrical boundary conditions, we constructed a detailed thermal and structural model of the packaged micropump, and we used it as a benchmark to compare the accuracy of further approximations, the model complexity reduction, and the computational time savings.

Step 3: Create an approximate macro-model of the packaged micropump and validate against the model in Step 2.

To create a reasonable reduced order model of the packaged lumped model microactuator, we used the heat input of the micromodel and applied it to a macromodel using the following boundary conditions:

- Load: heat generation or heat flux.
- Boundary conditions:

- Convective heat transfer coefficient of 25W/mK on exposed surfaces; and micro-pump diaphragm surface maintained at 36.8^{o}C due to fluid flow.
- Convective heat transfer coefficient of 25W/mK on exposed surfaces, and ignoring heat losses through the fluid.

The second boundary condition represents the case in which heat loss is primarily due to diffusion via conduction into the package and convection to the ambient. We wanted to verify if heat extraction due to the fluid flow of the micropump is small enough and can be neglected. At this point, the package is assumed to have heat convection losses, and is not yet implanted inside the body.

Step 4: Create an approximate implanted macro-model.

We now changed the convection boundary conditions of the macromodel by "implanting" the micropump, e.g. surrounding it with an outer layer that simulates the body. This layer had similar thermal conduction as water (the human body is composed of 90% water), and we apply temperature boundary conditions on the outside layer consistent to that of a constant temperature at 36ºC.

Step 5: Use the detailed micro-model with appropriate boundary conditions to calculate the actuator displacement.

On a micro-model consisting of detailed actuator, wafer handle, and top cap chip we used the following assumptions:

- Load: heat generation or heat flux.
- Boundary conditions:

- Average temperatures on the handle wafer and top cap chip obtained from the macromodel in Step 4.

We then compared the resulting actuator displacement with full fledged thermo-mechanical model to verify accuracy and determine pushing force of the thermal actuator for different input voltages applied.

Step 6: Create a lumped-parameter approximation of the flow model for an unpackaged micropump.

This model will calculate the flow rate generated by the micropump given peristaltic forces applied on the pump chamber diaphragm.

Step 7: Compare the packaged and unpackaged microactuator force on the pump diaphragm.

Here we compared the pumping force of micro-model in Step 5, with the force obtained with the same, but unpackaged micro-model. We then used the estimate in pumping force to calculate the packaged pump flow rate using the model in Step 6.

Step 8: Propose package modifications using macro-model in Step 4 in order to achieve a target implanted outer temperature.

Using the model in Step 4, we performed necessary modifications to package carrier to ensure that the outside temperature on the carrier does not exceed 40.8^{o}C, and can thus be safe to use inside the human body.

7.2.3 Thermal and Flow Analysis of Micropump

In this section, we present the results of thermal and mechanical modeling of the unpackaged electrothermal micro-actuator under steady-state conditions. In order to

reduce the complexity of the analysis and the computational time, a simplified lumped model was created. However, in reducing the complexity, care was taken to ensure that the error introduced by such simplification is consistent and predictable, and within reasonable limits. The model and analysis modifications consist of:

i. Device geometry simplification such that the 6 pairs of chevron beams on either sides of the shuttle are represented by a single structural beam with equivalent electrical resistance. Since the chevron beam dimensions are small compared with other dimensions on the device, the actuator electrical resistance may be approximated by that of the beams. The thermal analysis is then carried out on the simplified device model. Results using both the coupled electrothermal analysis and the thermal analysis are presented in Figure 7.19. This modification is useful for the thermal analysis of the micro-pump actuator but cannot be used for mechanical analysis because of geometry and geometrical constraints between the actual and simplified models.

ii. Further simplification to the analysis is possible by decoupling the multi-physics electro-thermal coupled field to single field (thermal) field problem by applying either volumetric heat generation or heat flux on the actuator beams instead of applying voltage on the pads. It is essential that the overall electrical resistance of the two models (detailed and lumped microactuators) be similar. A simplifying assumption, is that the resistance (more appropriately, the resistivity) of the beams are temperature independent. With the applied voltage and resistance known, the Joule heating on the actuator beams can be determined from:

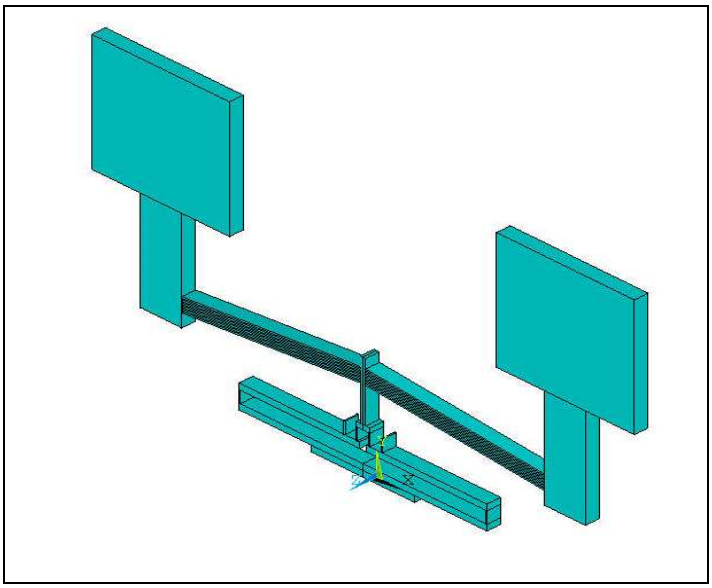

(a)

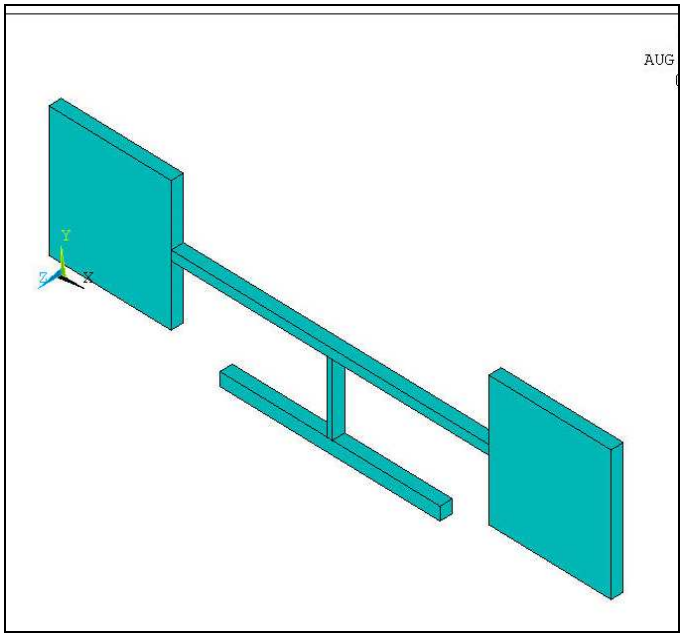

(b)

Figure 7.19 (a) Detailed (actual) device model with six chevron beams on either sides of the shuttle and (b) simplified device models with collapsed beam representing the chevron beams.

$$P = \frac{V^2}{R}, R = \rho \frac{L}{A}, \tag{7.1}$$

where R is the electrical resistance (Ω), V is the applied voltage (V), P is the dissipated power (W), ρ is the resistivity of doped silicon (Ω/m), L is the total length of the chevron beams, and A the equivalent cross-sectional area of all beams.

7.2.3.1 Lumped and Detailed Thermal Analysis of Micro-Actuator

We compared the results of coupled field electrothermal analysis of the detailed microactuator (shown in Figure 7.19a) with that of thermal analysis of the detailed microactuator to ensure that the electrothermal model with applied voltage as input power is equivalent to the thermal model with applied heat generation (or heat flux) as the input power. The results of the steady state analysis at different power level indicated less than 1% error between both models as shown in Figure 7.20. The element Solid98 and Solid87 elements were used for the coupled field electrothermal and single field thermal problems. Each model comprised of 12,574 elements, and the computational time for solving the thermal model is about half of that for the coupled field model. For the coupled field problem, the load was applied as voltage input (loading scenarios of 4, 6, 8, 10 V were considered) while for the case of single field thermal, the load was volumetric heat generation by the microactuator beams. The value of the heat generation was obtained from the voltage input, the resistance of the actuator, and the volume of the microactuator beams. The boundary condition for both cases is convective heat transfer of 25 W/m^2K.

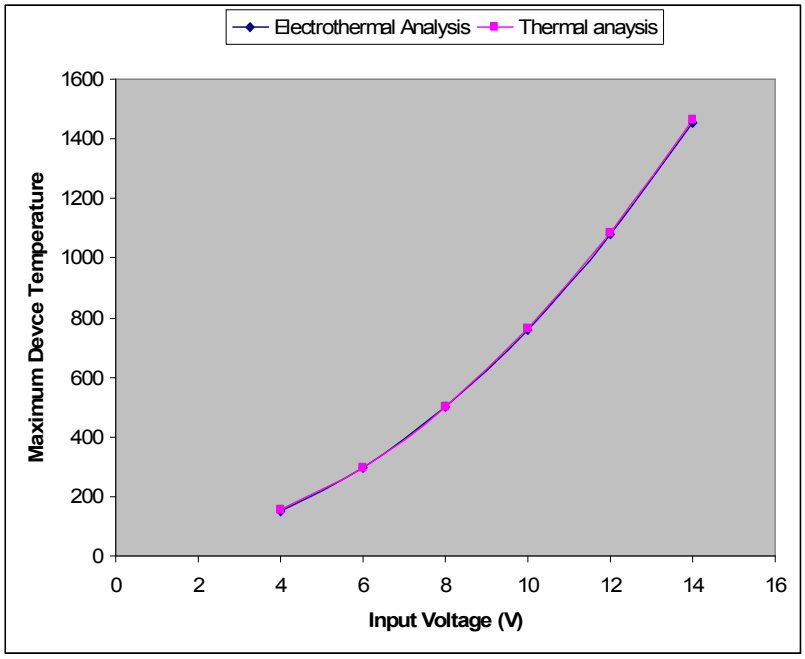

Figure 7.20 Electrothermal analysis of microactuator: detailed model vs. lumped model.

Next, we compared the results of electrothermal analysis of the detailed microactuator model shown in Figure 7.19a with that of thermal analysis of lumped microactuator model shown in Figure 7.19b to determine if we can replace the full fledged electrothermal analysis of the detailed microactuator with thermal analysis of simplified microactuator model. In this case, the error level was less than 5% as shown in Figure 7.21.

The load and boundary conditions (B.C.) for these analyses were:

Load: 4, 6, 8, 10, 12, and 14 V.

B. C.: 36.8^{o}C on the pad surfaces, and convective heat transfer coefficient of 25 W/m^{2}K on exposed surfaces.

The material properties used in this work are given in Table 7.2. By using this approach, the simulation time was reduced from over 8 minutes to less than 25 seconds (~1/200th reduction in computation time).

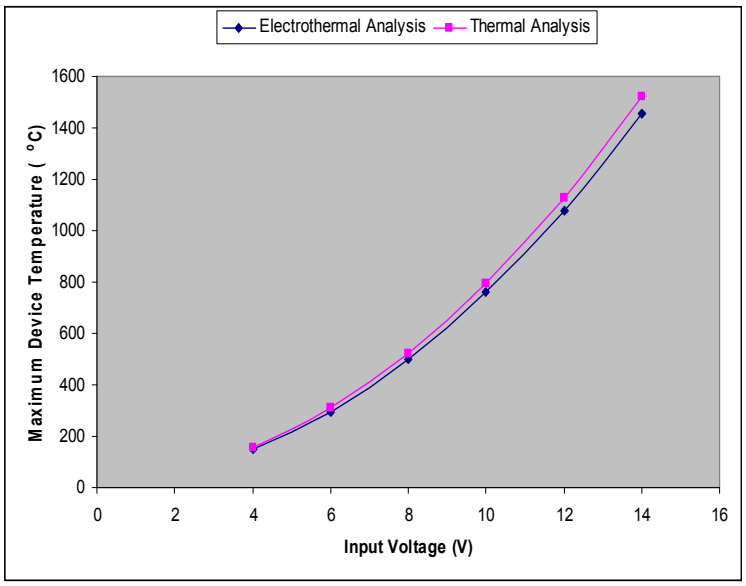

Figure 7.21 Thermal analysis of microactuator: electrothermal analysis vs. thermal analysis.

Table 7.2 Material properties values used for micropump models.

Entity	Density (J/kg^3)	Specific Heat (J/KgC)	Thermal Cond. (W/mC)	ρ (Ω-m)	E (GPa)	P. Ratio
Device Layer	2300	720	150	1.1E-04	169E9	0.22
Oxide Layer	2200	700	1.4	5.05E15	73E9	0.22
Air	0.1239	1006	0.024	2.0E13	1.01E5	0.22
Handle Layer	2300	720	150	2.3E-5	169E9	0.22
Glass	2230	753	110	400E6	63E9	0.2
Kovar	8360	439	17.3	0.49E-6	138E9	0.317

7.2.3.2 Thermal Analysis of Packaged Micropump

From the results of section 7.2.3.1, we gained confidence that by reducing the problem to single field thermal analysis from a coupled field electrothermal analysis, we do not lose much accuracy. In this section, we describe the steady-state analysis of the packaged micropump consisting of lumped microactuator model, the micropump device layer, the top cap chip, Kovar based carrier and lid. The approach here is similar to that of section 7.2.3.1 with the problem reduced to single physics (thermal) analysis of a packaged lumped microactuator. The thermal load was applied as volumetric heat generation. We will discuss results of the instance of the following two boundary conditions: convective heat transfer coefficient of 25W/m^{2}K on exposed surfaces; and micro-pump diaphragm surface is maintained at 36.8^{o}C due to fluid flow.

Simulation results show that boundary condition 2 represents an extreme case in which heat loss is primarily due to diffusion via conduction into the package and convection to the ambient. We further note that the effect of fluid flow across the pump's diaphragm at expected pump working voltage is about ~10% reduction in the peak temperature of the micropump as shown in Figure 7.22.

We also notice the effect of packaging on the maximum device temperature for corresponding power input levels. For instance, at loading condition corresponding to power input level of 4V, the maximum device temperature is reduced from 158^{o}C (for the unpackaged microacuator shown in Figure 7.20) to 79.6^{o}C (for the packaged case shown in Figure 7.22). We further notice the effect of increased thickness of the air gap layer between the device and the top cap chip. The air gap layer is modeled as a thin

conduction layer with almost zero modulus. By increasing the air gap thickness, the thermal resistance offered by air gap increases therefore increasing the maximum device temperature. By increasing the air gap thickness from 2 to 5 µm, the device temperature increased by up to 17% over our input power range of 4 to 14V as illustrated in Figure 7.23. Similar work [124], recently reported that increasing the air gap between the device and the top cap chip from 2 µm to 3 µm resulted in 10% increase in device temperature.

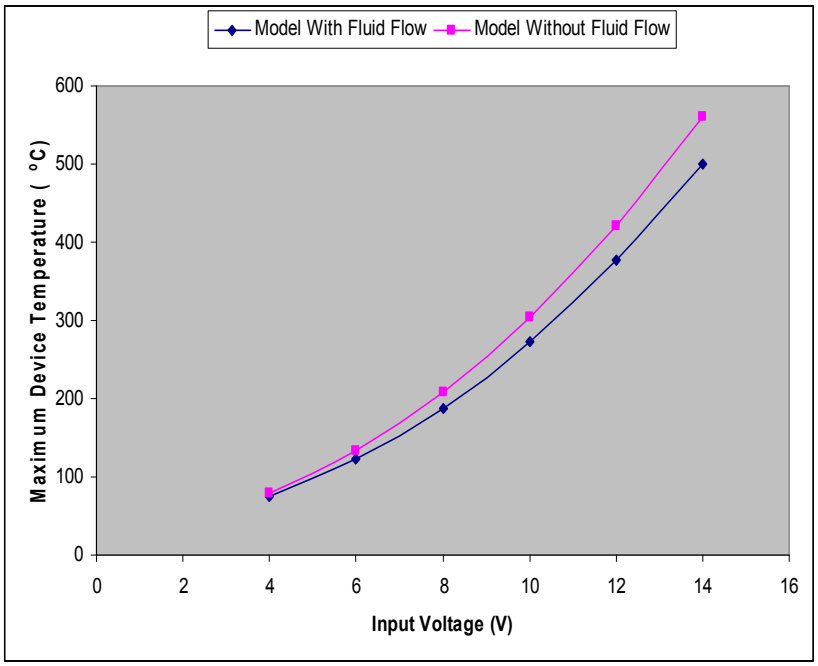

Figure 7.22 Thermal analysis of micropump: model with fluid flow vs. model without fluid flow.

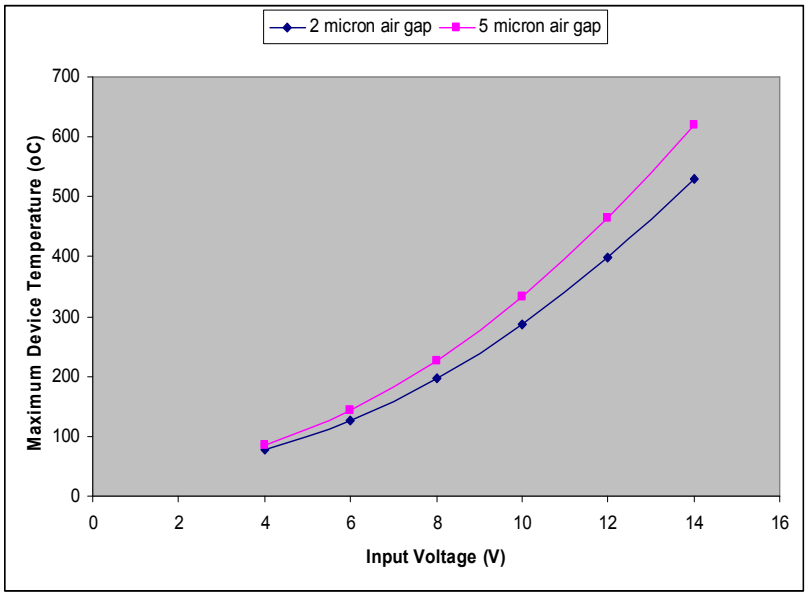

Figure 7.23 Effect of air gap on device temperature.

7.2.3.3 Actuator Displacement and Force

It is computationally intensive to solve the coupled field (thermal-structural) problem for the complete package. The micro-actuator deflection analysis was solved using sequential coupled method whereby the result of the thermal problem is used as the input for the structural problem to obtain the microactuator deflection. A simplifying assumption was that the structural problem does not significantly impact the thermal state of the device. This problem was solved using heat flux as the thermal load and the results obtained were compared with that of using volumetric heat generation as the thermal load.

The temperature over each of the pump's surrounding structures (top cap chip and handle layer) from section 7.2.3.2 were used as thermal boundary conditions for the thermal-structural analysis of a model consisting of detailed microactuator structure,

device layer, air gap layers, top cap chip, and handle layer to determined the microactuator displacement. The structural problem is then solved via sequential coupled analysis in which the thermal result from previous step served as input for the structural analysis.

Using heat flux value corresponding to 4, 6, 8, 10, 12, and 14V power input, convective heat transfer coefficient, h of 25W/m^{2}C on all surfaces, and applying the average temperature of both the substrate and the glass cover as boundary conditions, the thermal problem was simulated. The solution obtained from this step served as the input for the structural problem. The results obtained were compared with those obtained in section 7.2.3.2 (packaged lumped microactuator model without fluid flow). The difference in the results is less than 7% as shown in Figure 7.24. At input power level of 8V, the maximum actuator deflection was 10.1 μm as shown in Figure 7.25.

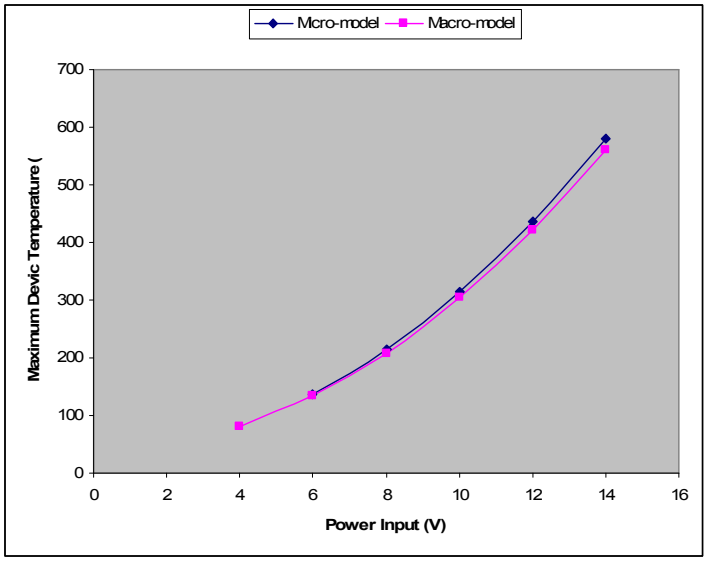

Figure 7.24 Device maximum temperature: macro-model vs. micro-model.

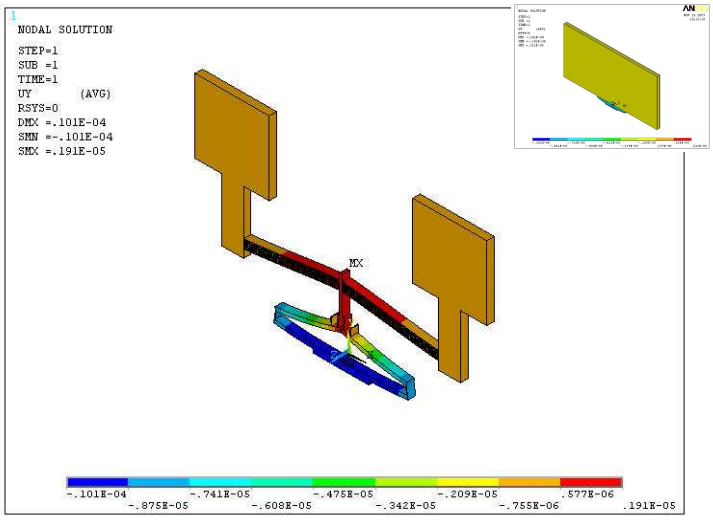

Figure 7.25 Illustration of microactuator displacements at 8V input.

The displacement values obtained for the packaged micropump are shown in Table 7.3. In this table, X_i is actuator displacement using temperature boundary conditions on the substrate and the cap chip, while X_f is actuator displacement using temperature boundary conditions on the substrate and the cap chip, and also, heat flux corresponding to 4, 6, 8, 10, 12, and 14V on actuator beams. T_i and T_f are the maximum device temperatures at X_i and X_f respectively. The difference between X_f and X_i is the net actuator displacement. The displacement and temperature values for the unpackaged microactuator are presented in Table 7.4. For a given voltage value, packaging results in reduced device temperature and microactuator displacement.

The plot of the difference in displacement between packaged and unpackaged micropumps is shown in Figure 7.26. For example, at 8V, for the packaged device, X_f is 10.1 μm, and T_f is 220.1 ^oC while for the unpackaged device, the maximum device temperature is 487.7 ^oC with displacement of 28.6 μm.

Table 7.3 Microactuator displacement for packaged micropump.

Voltage V	X_i (μm)	X_f (μm)	T_i (^oC)	T_f (^oC)
4	1.96	3.3	51.21	82.6
6	3.08	6.1	69.2	139.9
8	4.65	10.1	94.5	220.1
10	6.67	15.1	126.79	323.2
12	9.14	21.4	166.41	449.2
14	12.1	28.7	213.5	598.3

Table 7.4 Microactuator displacement for unpackaged micropump.

Voltage V	Displacement (μm)	Temperature (^oC)
4	7.52	140.7
6	16.3	285.3
8	28.6	487.7
10	44.4	747.9

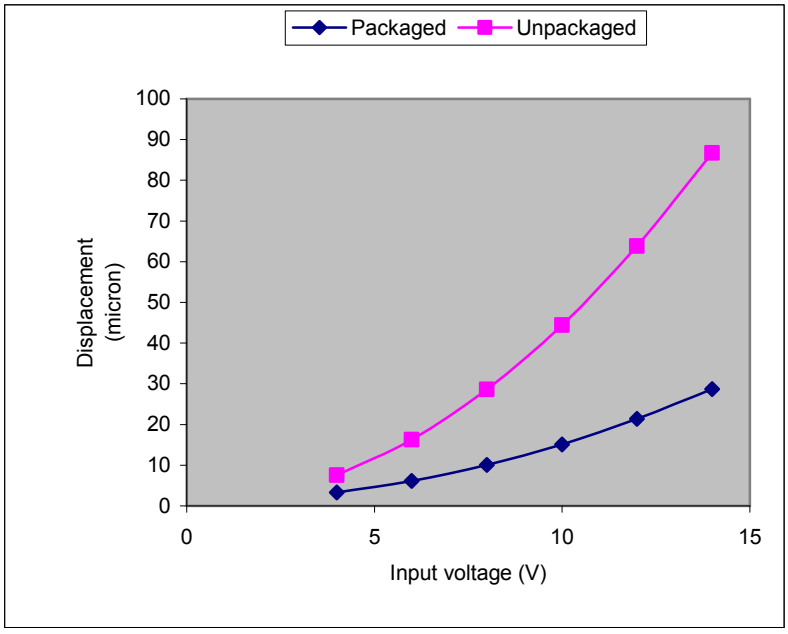

Figure 7.26 Difference in displacement between packaged and unpackaged micropumps.

The actuation force may be determined experimentally by measuring the deflection of a cantilever beam of known stiffness. Using simulation, we determined the actuation force by estimating the counterbalancing force F needed to establish equilibrium (zero displacement) of the device as shown in Figure 7.27. This force is a function of the thermal strain caused by current flow in the actuator beams. This force is obtained by calculating the stiffness of the microactuator before the incidence of buckling takes place (within the elastic range) from the force and displacement values. The force/displacement values obtained for the case of 8 V input power are given in Tables 7.5 and 7.6 for both the packaged and unpackaged microactuators.

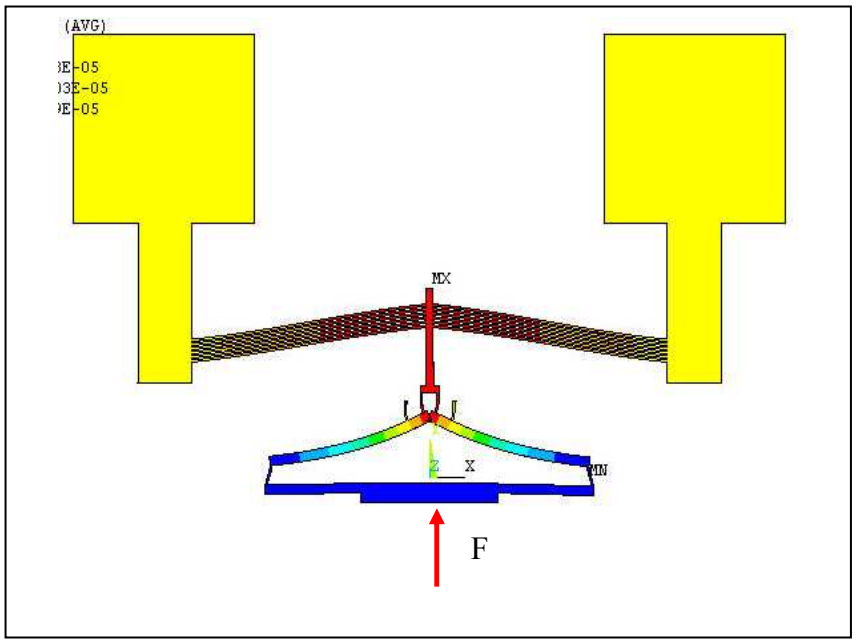

Figure 7.27 Counterbalancing force F needed to establish equilibrium (zero displacement) of the micropump.

Table 7.5 Microactuator force/displacement values at 8 V for packaged device.

Force (mN)	Displacement (m)
0	1.01E-05
0.001875	8.04E-06
0.00375	6.00E-06
0.005625	3.97E-06
0.00675	2.83E-06

Table 7.6 Microactuator force/displacement values at 8 V for unpackaged device.

Force (N)	Displacement (m)
0	2.86E-05
0.001875	2.59E-05
0.00375	2.32E-05
0.005625	2.05E-05
0.0075	1.78E-05
0.01125	1.26E-05

The stiffness values (slope of the force/displacement curve shown in Figure 7.28 and 7.29) for the packaged and unpackaged cases are 925.4 N/m and 701.8 N/m respectively while the actuation force (y-axis intercept of the force/displacement curve shown in Figures 7.28 and 7.29) for the packaged and unpackaged cases are 9.3 mN and 20.1 mN respectively. The difference in stiffness values for the two cases is due to the reduced device temperature as a result of packaging.

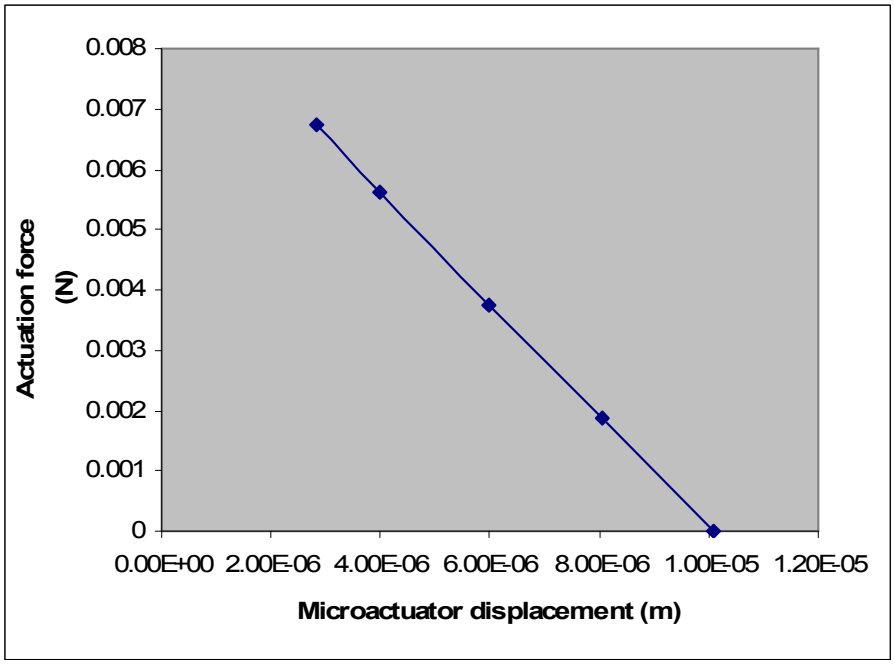

Figure 7.28 Force/displacement plot for packaged device.

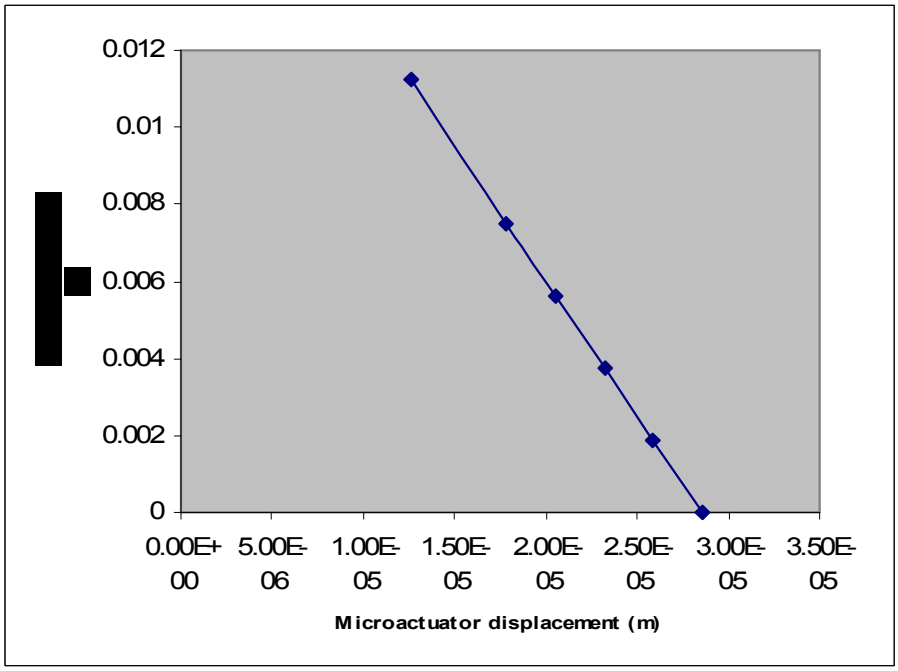

Figure 7.29 Force/displacement plot for unpackaged device.

7.2.4 Fluid Flow

The fluid flow characterization of a similar micropump can be found in [1114,115,125], where it was carried out on an unpackaged micropump. We are interested in knowing how the fluid flow is affected by the packaging the micropump. In these previous works involving the unpackaged micropump, the pumping flow was estimated using a simple lumped parameter model consisting of a flexible membrane, and a discharge catheter against vein pressure, shown in Figure 30.

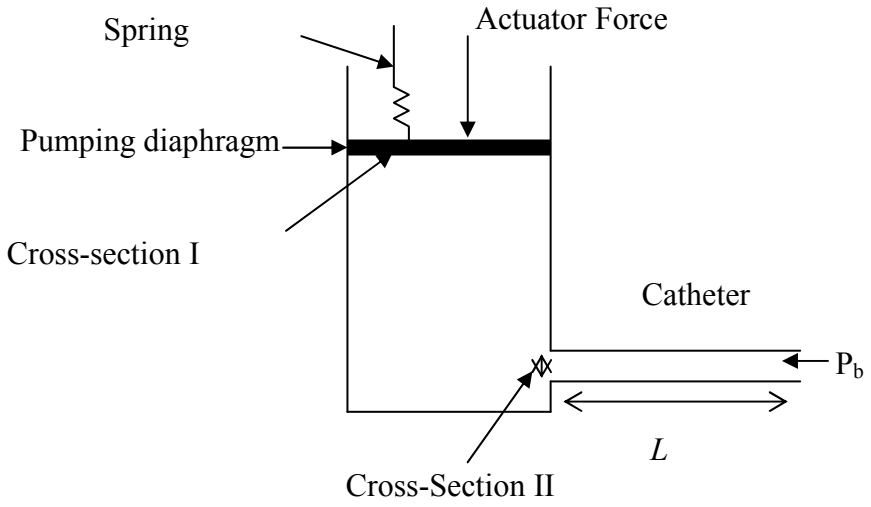

Figure 7.30 Lumped parameter model used to estimate flow rate of the micropump [126].

In Mhatre [126], the motion obtained by flexing the microactuator on the micropump's diaphragm is simplified to the motion of a piston of mass m = 3 μg. Based on the finite element model of the actuator and diaphragm [114, 114], the stiffness is k

= 200 N/m. Flow simulations for a micropump/check-valve/catheter system were carried out in *MATLAB*. Assuming a sinusoidal signal to the MEMS actuator with frequency f = 50Hz (close to the thermal bandwidth of the MEMS actuator), and amplitude F = 6mN. The output flow rate of the pump is as shown in Figure 7.31 and the simulation results indicate that an average flow rate of 85 µl/min can be achieved against a venous pressure of 8 mmHg [126].

Finally, we make a simplifying assumption on scaling of the flow with respect to the pumping membrane force: if pumping force F is scaled up by a factor of α, the pumping rate will also scale up by the same factor. We will then estimate the scaling factor α obtained by packaging the micropump, in order to obtain an estimate of the fluid flow change due to packaging. This scaling factor obtained was $\alpha = \frac{20.1}{9.3} = 2.16$. In Mhatre [126], 6mN force (unpackaged micropump of a slightly different design) yielded an average flow rate of 85 µl/min. We then expect a flow rate of $\frac{85}{\alpha} = 39.33 \mu L / \min$ for the packaged micropump.

7.2.5 Approximate Implanted Macro-model

In this section, we use the macro-model to prepare an approximate implanted model of the micropump. The implanting environment is assumed to have similar thermophysical properties as water (the human body is 90% water). The steady state results for heat flux inputs equivalent to 8 and 10 V input power are presented in Figures 7.32 and 7.33 respectively. The outer layer of the body simulating the water volume is maintained at 36.8C. Figure 7.32(a) presents the result of steady state thermal

analysis of approximate an implanted micropump model (complete package including the implant environment), while Figure 7.32(b) shows the temperature distribution for the implant environment alone. The input heat flux for the results presented in Figure 7.32 is equivalent to 8 V input voltage.

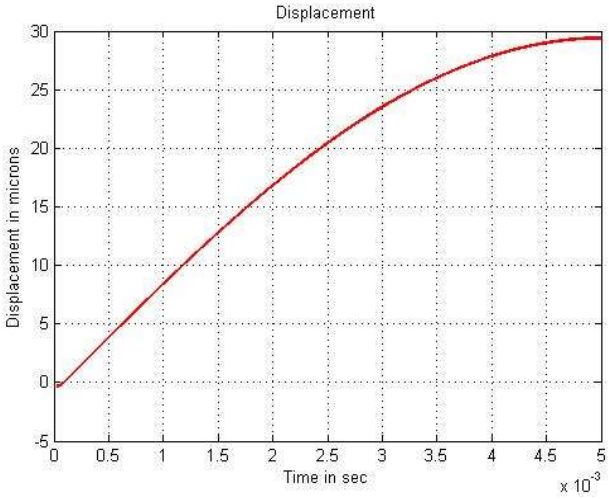

(a)

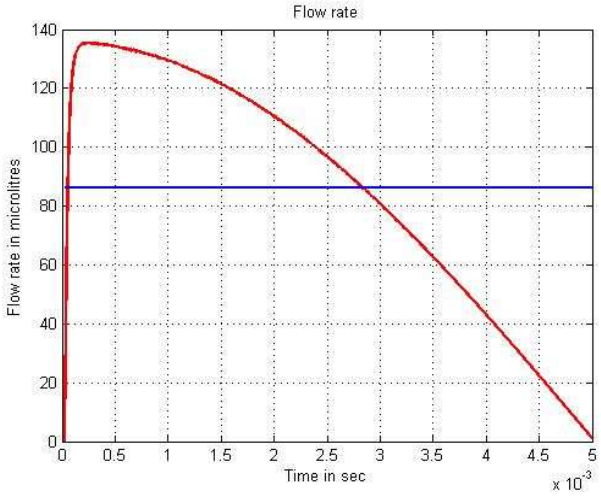

(b)

Figure 7.31 (a) The displacement of the diaphragm in micrometers during the pumping cycle, and (b) the corresponding flow rate at the catheter output in µl/min [126].

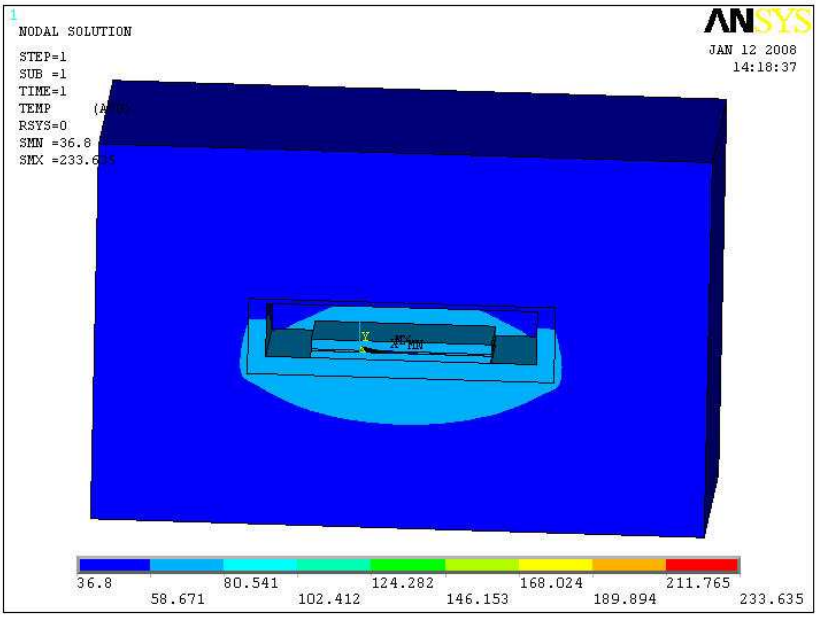

(a)

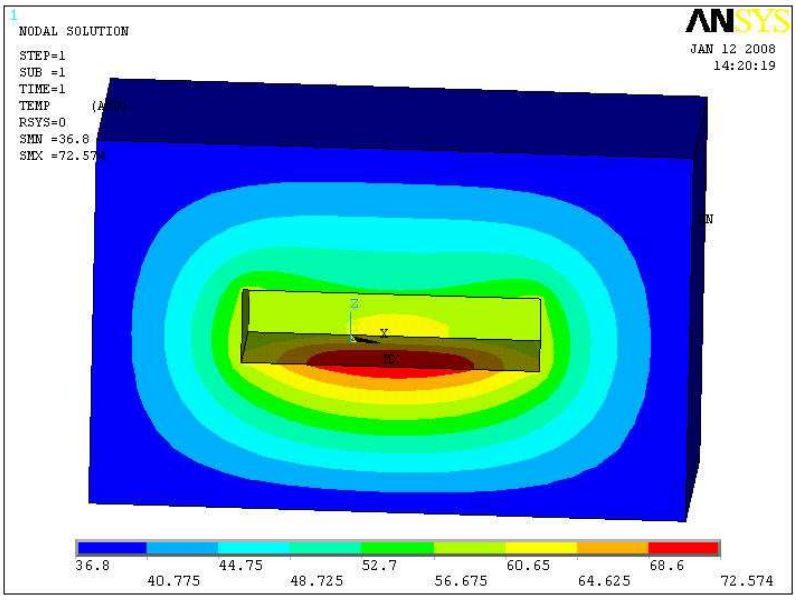

(b)

Figure 7.32 Steady state thermal analysis of approximate implanted micropump model (a) complete package and (b) the implant environment. Input heat flux is equivalent to 8 V input power.

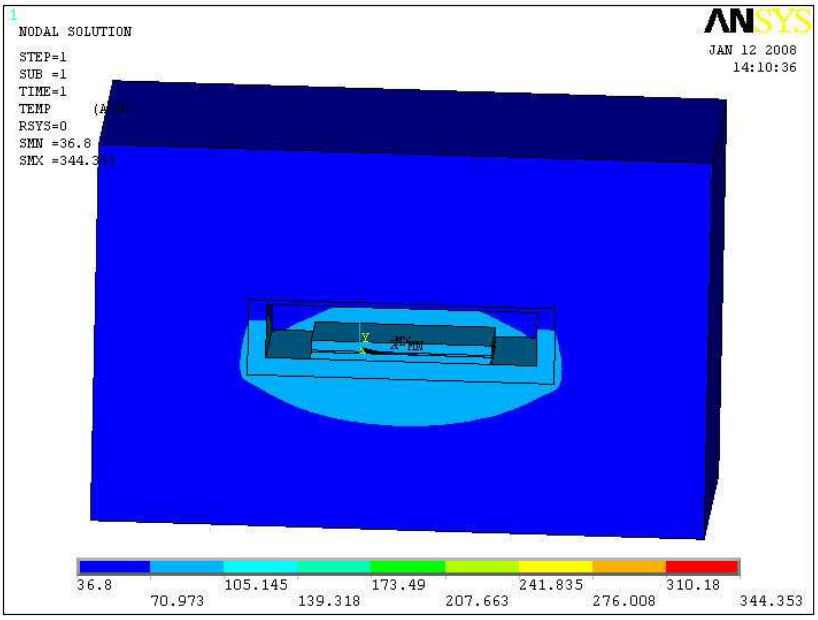

(a)

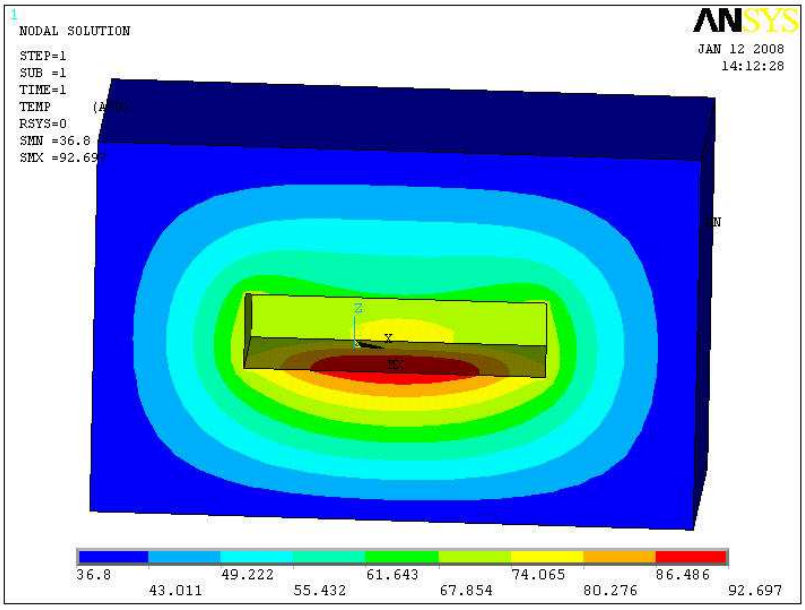

(b)

Figure 7.33 Steady state thermal analysis of approximate implanted micropump model (a) complete package and (b) the implant environment. Input heat flux is equivalent to 10 V input power.

Figure 7.33(a) presents the result of steady-state thermal analysis of an approximate implanted micropump model (complete package including the implant environment), while Figure 7.33(b) shows the temperature distribution for the implant environment alone. The input heat flux for the results presented in Figure 7.33 is equivalent to 10 V input voltage. From these results, we observe that the implant environment is exposed to high temperatures (72.6 and 92.7 C) respectively. These temperature values are in excess of the 40.8 C requirement for implantation inside the human body, hence we need to redesign the package.

7.2.6 Micropump Package Redesign

The initial micropump package was implemented using a Kovar carrier in order to reduce the thermal mismatch between the micropump's SOI die and the carrier. This package was found to be inadequate in the previous section since the steady-state temperature distribution on the outside of the carrier exceeds 40 ^{o}C. The temperature obtained is 106 ^{o}C as shown in Figure 7.34.

We propose a package modification consisting of polybutylene terephthalate (PBT) outer package with locating pins that constricts the movement of the inner Kovar carrier as shown in Figure 7.35. With this modification, we simulated a maximum outer temperature of about 40 ^{o}C on the micropump's outer surface. The analysis of this complex system was greatly simplified by using lumped models that essentially reduces the problem to single physics. This resulted in reduced computational effort without appreciable loss of accuracy.

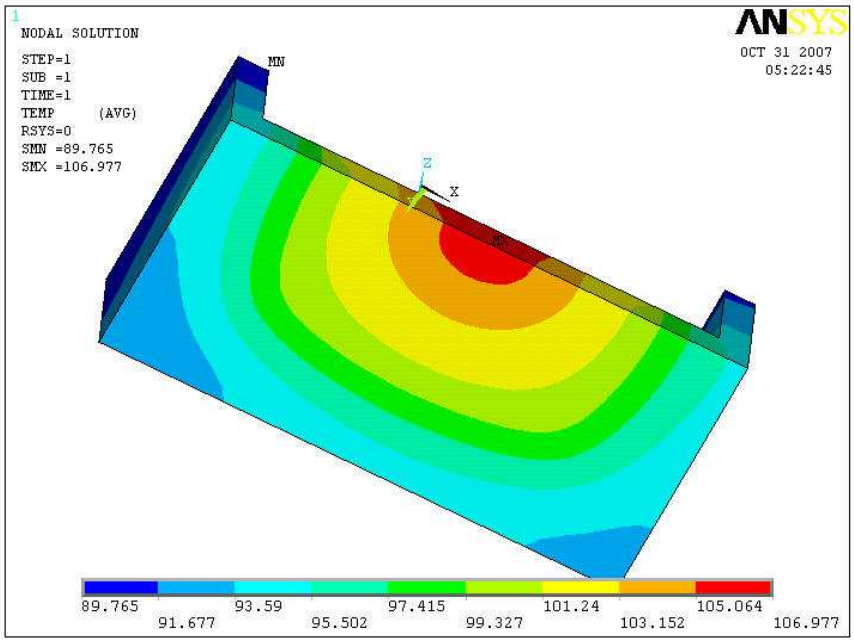

Figure 7.34 Temperature distributions on the original Kovar carrier.

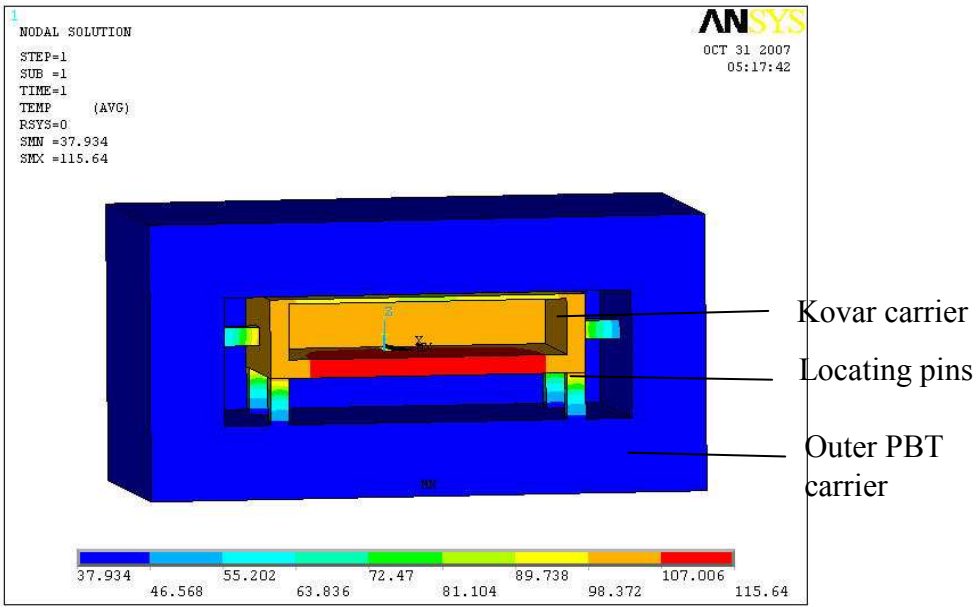

Figure 7.35 Temperature distributions on the modified micropump package.

While a full fledged model for this package would have taken hours to solve, we were able to solve this problem in less than 2 hours. For this work, solving the full fledge model was not an option because we required more than the 126,000 nodes provided by our version of ANSYS®. In addition, the computational resources would have been exorbitant. While the new design may not be optimal, our analysis approach provides a fast and efficient way for implementing parametric design to optimizing the package using the lumped model

7.3 Conclusions

We used numerical simulation to investigate the effect of different laser power ratings on the carrier temperature distributions. The results show that carrier geometry /or surface property modifications are necessary in order to provide adequate heat for the reflow of the indium solder attachment metal. We investigated the use of 12, 20, and 40W laser soldering for our package. While theoretically, any of these power levels may deliver sufficient energy for the soldering process (provided we chose appropriate heating duration), the use of an optimal power level and heating duration combination is desirable. We observed for instance that while a 12W laser provides adequate heating to the carrier, the prolonged heating required to deliver adequate heating results in heat diffusion throughout the package, causing the adjacent fiber to shift due to elevated temperatures. At higher laser powers (20W, 40W), we observed that the temperatures of the adjacent solder holes are substantially lower than that of the hole nearest to the laser heating spot due to reduced heating duration necessary to deliver adequate energy for the soldering process. The need for rapid heating that prevents appreciable thermal

diffusion throughout the package requires the use of high laser power levels that resulting in large thermal gradients and hot spots at laser spots.

We also presented results based on reduced-order lumped model approximation for a micropump. The error obtained is less than 6% (for the electrothermal analysis of the packaged micropump) with computational time reduction from about 8 hours (using ANSYS® solid98 coupled field elements to a few minutes (using solid87 thermal elements). Based on the results from the thermal analysis, package modification was deemed necessary in order to maintain package outside temperature no more than 40.6^{o}C. Our approach was both sufficiently accurate and computationally efficient and can be used for parametric analysis of packaged electrothermal MEMS actuators in general.

CHAPTER 8

RELIABILITY TESTS AND RESULTS

8.1 Die Attachment

Die shear reliability assessment was carried out to qualify the solder joint strength by applying a pure shear force on the solder layer between the bonded parts until it yields. Due to space constraint in the carrier, it was difficult to introduce a shearing tool within the clearance space between the carrier wall and the silicon MEMS die. We therefore investigated the solder shear strength by bonding a silicon die with 80%Au-20%Sn solder to a glass top die with same base metal as the carrier (i.e., nickel and gold), and also to a Au-coated Kovar carrier plate.

The bonded dice are attached to a gold coated Kovar® plate using 80%Au-20%Sn solder preforms and the Kovar® plate is attached to a die shear fixture as shown in Figure 8.1. For the glass die-to-Si die shear test, the die shear fixture was designed such that the shearing tool makes contact with an edge of the top glass die and does not touch the bottom silicon die or the supporting Kovar® plate test. Likewise, for the Si die-to-carrier die shear test, the shearing tool does not touch the Kovar® plate. This assembly is then mounted on an Instron MicroTester® for the die shear test.

For our solder type (80%Au-20%Sn), experiments suggests no significant difference in the strength of MEMS die-to-carrier attachment bonded in air ambience and those bonded in controlled ambience of nitrogen gas, or nitrogen-hydrogen gas. This can be explained by the high gold content in the solder material making it less prone to surface oxide formation, and also the use of bonding pressure for breaking surface oxides on the solder surface. However, for indium solder (used for the fiber-to-carrier attachment), we found out that the soldering ambience has a significant impact on the flow of the molten solder metal.

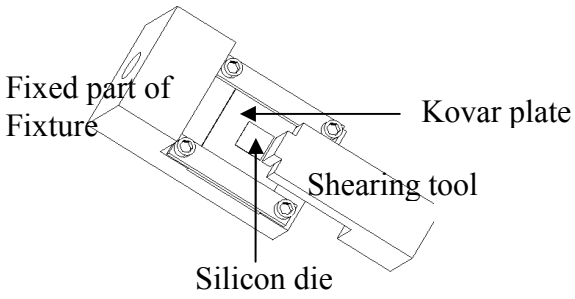

Figure 8.1 Test fixture for die shear test.

Figure 8.2 Instron MicroTester® used for shear and fiber pull tests.

The shear force is applied until a sudden drop in load occurs, at which point the test ends. The results obtained after the die shear of seven MEMS chip to carrier attachments indicate a bond strength of over 13.8 MPa on a 6mm x 6mm bond area with a 25 micron thick 80%Au-20%Sn solder preform. All seven samples subjected to die shear test passed the test with no sign of delamination. Since the die bonds did not fail at the maximum machine load (500N), we conclude that the bond strength exceeds the 13.8 MPa value, therefore, the bonded dies passed the MIL-STD requirement for the die shear test (2.5kg on the bond area). A typical result obtained from a die shear test performed using an Instron® pull tester is shown in Figure 8.3, and indicates that the joint is able to withstand 500N (or 51.02 kg) shear load on the bond area.

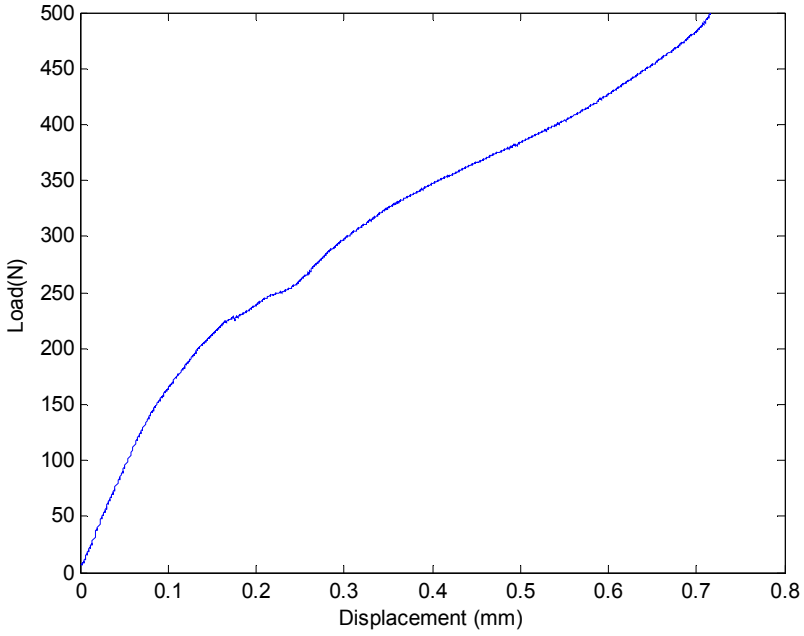

Figure 8.3 Sample die shear test result from Instron® instrument.

The silicon die-to-Pyrex cap chip shear test is similar to that of the die-to-carrier test described earlier. The results obtained from the Silicon die-to-Pyrex cap chip shear test gave shear values ranging from 1.39 to 7.10 MPa as indicated in Table 8.1. The regression method was used to relate the process parameters to the die shear strength and the regression equation is as follows:

$$Y = -5.65 + 0.0154\,X_1 + 0.0195\,X_2 + 0.0536\,X_3 \qquad (8.1)$$

Where Y is the shear load at failure, X_1 is the bonding pressure, X_2 is the bonding temperature, and X_3 is the dwell time.

Table 8.1 Die shear test results.

Set No.	Ring Width (mm)	Pressure (Psi)	Temp (C)	Dwell Time (min)	Shear Load (Y) at failure (MPa)
1	2.0	50	320	10	2.03
2	2.0	75	320	5	1.56
3	2.0	75	340	10	2.34
4	1.75	100	320	10	1.39
5	1.75	150	320	10	7.10
6	1.5	150	340	20	4.12
7	1.5	200	340	5	4.90
8	1.25	200	320	20	5.49
9	1.25	250	340	20	5.03
10	1.0	300	320	10	5.28
11	1.25	150	340	15	4.00
12	0.75	200	340	15	5.77

A single replicate experiment was performed, hence the need to examine the half normal probability plot of the effects estimates [96]. The half normal probability plot and the Pareto plots provide effective means of determining important variables.

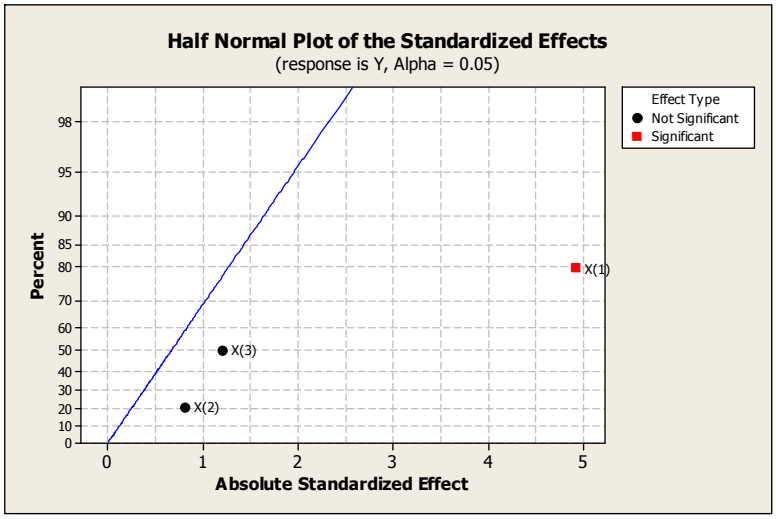

Figure 8.4 Half normal plot of the standardized effects.

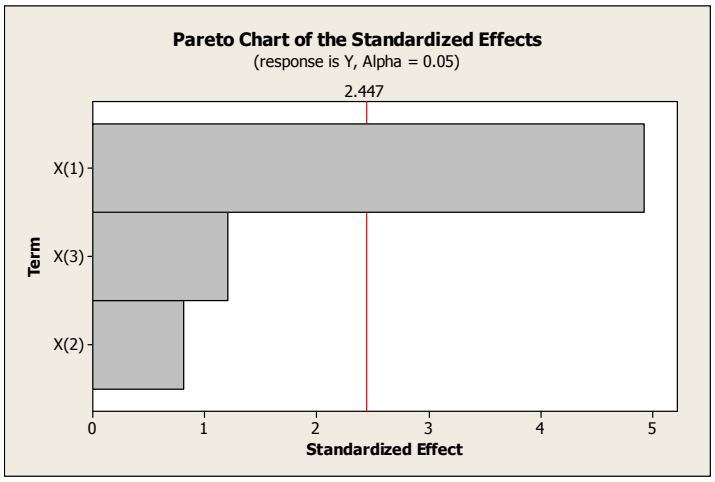

Figure 8.5 Pareto chart of the standardized effects.

We see from both the half normal plots (Figure 8.4), the Pareto plots (Figure 8.5) and the P-values in Table 8.2 that the die bonding pressure (X_1) has the most significant effect on the die shear strength.

Table 8.2 Effects of variables from the die-shear DOE.

Predictor	Coef	SE Coef	T	P	
Constant	-5.651	7.820	-0.72	0.497	
X_1	0.015	0. 003	4.93	0.003	
X_2	0.019	0. 024	0.81	0.446	
X_3	0.054	0. 0444	1.21	0.273	
S = 0.715731	R-Sq = 85.6%	R-Sq(adj) = 78.4%			
Analysis of Variance					
Source	DF	SS	MS	F	P
Regression	3	18.30	6.10	11.91	0.006
Residual Error	8	3.07	0.51		
Total	11	21.38			

8.2 Fiber Attachment

The fiber pull test was used to assess the bond strength of the fiber-to-carrier attachment. This was performed on an Instron MicroTester® machine using a set up similar to that shown in Figure 8.6. The carrier is fixed rigidly to the lower gripper of the MicroTester® while the optical fiber is attached to the upper gripper. In order to prevent damage to the fiber as a result of the machine's clamping force, the free end of the fiber was inserted into a 280 μm internal diameter Peek® tubing and then clamped to the machine's upper gripper. The test commences with a slow, steady upward pulling (tensile) force. The test concludes when there is a sudden drop in load signifying that the solder joint has failed.

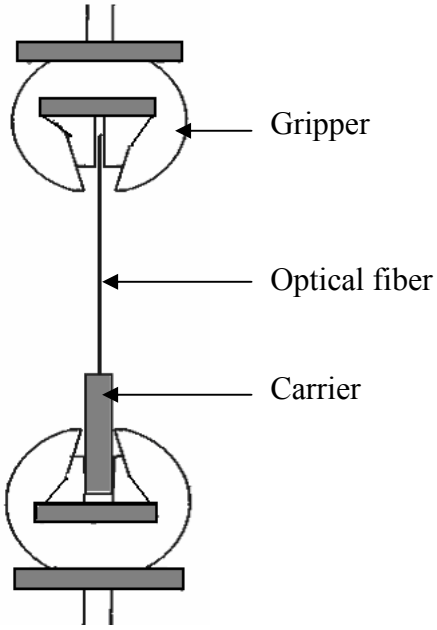

Figure 8.6 Experimental setup for fiber pull test.

Initially, 4 samples were tested and the results of the fiber pull test from these 4 sampled are as follows {8.85N, 9.36N, 9.89N, 9.84N}. This first round of experiments is used to estimate the minimum number of samples needed. We obtain the mean fiber pull strength, variance, and standard deviation as:

Mean, $\bar{X}$ = 9.485N, (8.2)

Variance, $s^2 = (0.2363)N^2$, (8.3)

Standard deviation, s = 0.486106984N. (8.4)

From the fiber pull test, we obtain the confidence interval. The confidence interval is a range of values which contains a population parameter with a certain degree of

confidence. The risk assumed in making this assertion is represented as alpha, α, where $0<\alpha<1$.

The confidence level is defined as 1-α. This can be expressed as a percentage as 100(1-α).

The 90% confidence interval for the sustained load is (1-α) = 0.9 or α = 0.10

$$\bar{X} = 9.485\text{N}, \tag{8.5}$$

$$s = 0.486106984\text{N}, \tag{8.6}$$

$$t = 2.353. \tag{8.7}$$

$$X_u = \bar{X} + ts\sqrt{n} = 9.485 + 2.353 * 0.486 / \sqrt{4} = 10.06N, \tag{8.8}$$

$$X_l = \bar{X} - ts\sqrt{n} = 9.485 - 2.353 * 0.486 / \sqrt{4} = 8.91N. \tag{8.9}$$

where n is the sample size.

We may conclude that we are 90% confident that the sustained load lies between

$$8.91\text{N}<\mu<10.06\text{N}. \tag{8.10}$$

To determine the lower 95% confidence bound for the sustained load

$$1-\alpha = 0.95 \text{ or } \alpha = 0.05, \tag{8.11}$$

$$\bar{X} = 9.485\text{N}, \tag{8.12}$$

$$s = 0.486\text{N}, \tag{8.13}$$

t = 2.353 (from a one-sided student's t statistics).

$$X_l = \bar{X} - ts\sqrt{n} = 9.485 - 2.353 * 0.486 / \sqrt{4} = 8.91N. \tag{8.14}$$

We are 95% confident that the sustained load is not less than 8.91N

Sample size

When planning an experiment we need to decide how many repeats to carry out to obtain a certain level of precision in the estimate. The sample size is a function of the confidence interval/level of precision, the confidence/risk level imposed, and the sample deviation/degree of variability.

The confidence interval/level of precision:

The level of precision is the range in which the true value of the population is estimated to be. It is often expressed in percentage points.

For Normal data, confidence interval for the mean, μ is: $\overline{X} - t_{n-1}\sqrt{\frac{s^2}{n}}$ to $\overline{X} + t_{n-1}\sqrt{\frac{s^2}{n}}$

i.e. $\overline{X} \pm t_{n-1}\sqrt{\frac{s^2}{n}}$. (8.15)

The confidence/risk level imposed

The confidence/risk level imposed is the risk taken in making an assertion. The normal distribution curve extends from -∞ to +∞. Therefore, we cannot guarantee that $\bar{X}$ lies within the limits μ-δ and μ+δ but we can determine the probability that $\bar{X}$ lies within these limits. In practice, this probability is usually established as 95% or 99%.

Sample Size Estimation

We can use the confidence interval formula to estimate the number of repeat experiments (sample size) to use in order to obtain a certain level of precision in our estimate.

For normal data, the confidence interval for μ is: $\overline{X} - t_{n-1}\sqrt{\frac{s^2}{n}}$ to $\overline{X} + t_{n-1}\sqrt{\frac{s^2}{n}}$.

$$\text{i.e. } \overline{X} \pm t_{n-1}\sqrt{\frac{s^2}{n}}. \qquad (8.16)$$

Suppose we want to estimate μ to within $\pm\delta$, where δ is given, we must choose the sample size, *n*, satisfying:

$$\delta = t_{n-1}\sqrt{\frac{s^2}{n}}, \qquad (8.17)$$

$$\therefore n = \frac{t_{n-1}^2 s^2}{\delta^2}. \qquad (8.18)$$

To use this, we need:

(i) an estimate of s^2 (e.g. results from previous experiments);

ii) an estimate of t_{n-1}. This depends on *n*, but not very strongly. One will not go far wrong, in general, if you take $t_{n-1} = 2.1$ for 95% confidence. Its value can be read off a Two-Sided Student's t Statistics chart.

95% confidence,

Take estimate of variance as: $s^2 = 0.2363\text{N}^2$, (8.19)

$\delta = 0.5\text{N}$, (8.20)

$t_n^2 = 3.182$ (for 95%confidence level, 3 d.o.f.), (8.21)

Therefore, $n = (3.182^2 \times 0.2363)/0.5^2 \approx 9.6$ (8.22)

i.e. at least 6 more samples.

In the next set of experiments, we conducted 10 additional fiber attachments. Therefore, a total of 14 tests were carried out to assess the optical fiber-to-carrier joint and the test results are presented in Table 8.3.

Table 8.3 Fiber joint failure load.

Sample	Load at failure (N)
1	8.85
2	9.36
3	9.89
4	9.84
5	9.02
6	7.37
7	6.43
8	7.68
9	9.65
10	9.38
11	9.14
12	6.81
13	6.94
14	7.38

Results obtained from the fiber pull test indicate that the solder joint strength ranged from 6.4N to 9.7N while the mean joint strength is 8.41N, corresponding to 5.02 MPa. Using simple statistical analysis on the fiber joint strength values obtained, we obtained a mean attachment strength exceeding 7N with a 99% confidence. We should point out that the average joint strength obtained (5.02MPa) is greater than the 4.05MPa [123] for the ultimate tensile strength of indium. The higher value obtained is probably due to the increased strength as a result on intermetallics formed between the fiber metallization and the indium solder. We further note that fiber failure appeared to be

due to bulk solder failure rather than delamination at the fiber-solder interface as revealed from the image shown in Figure 8.7, indicating good bond.

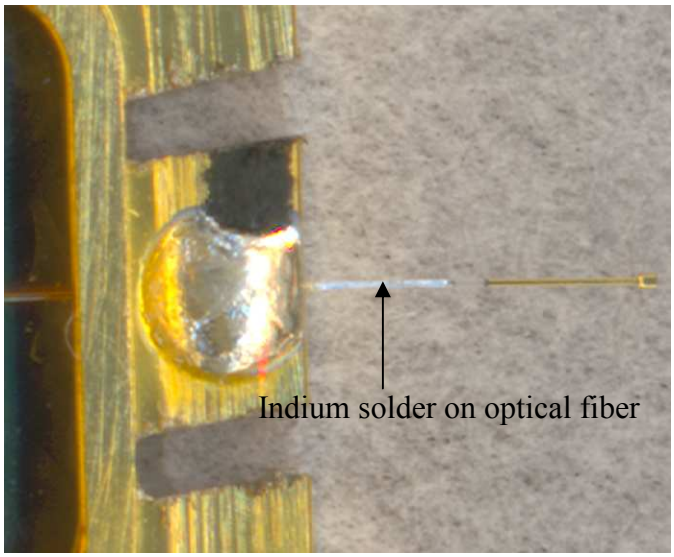

Figure 8.7 Optical fiber with indium solder illustrating bulk solder failure at the fiber-to-carrier joint.

8.3 Leak Test

The sealed package hermeticity (gross and fine leak) was verified using the NorCom® optical leak tester shown in Figure 8.8 in accordance with the MIL-STD 883E TM-1014 C4/C5. This leak tester measures the leak rate by observing the package lid deflection in response to changes in the package ambient pressure. Each sealed package to be tested was placed in a chamber with a laser interferometer capable of measuring out of plane deflections of a package lid. The test chamber pressure was 30 psi and the test duration, 40 minutes.

To start the test, vacuum is introduced into the chamber followed by chamber pressurization with helium gas. The chamber pressure is slightly modulated sinusoidally about a mean value and the observed lid deflection from sealed packages used to obtain the package internal pressure which is then used to obtain the package leak rate. Leak rates less than 5.2e-08 was observed for the two sealed packages tested using this procedure. Figure 8.9 shows sample images of the package lid during the test.

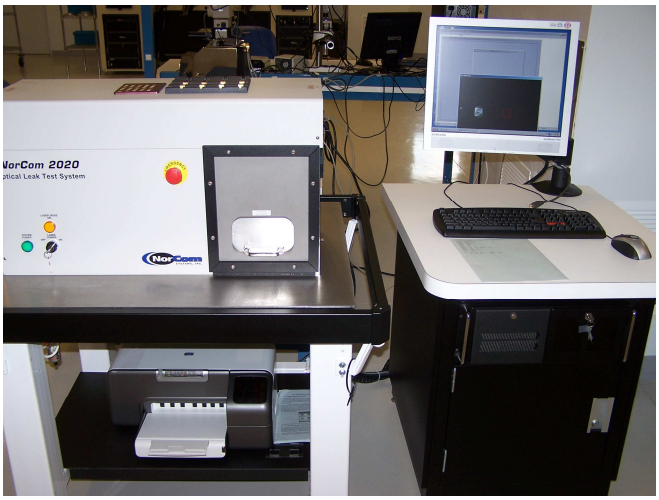

Figure 8.8 NorCom® optical leak tester for hermetic seal testing at the Bennington Microtechnology Center (BMC) in Vermont, USA.

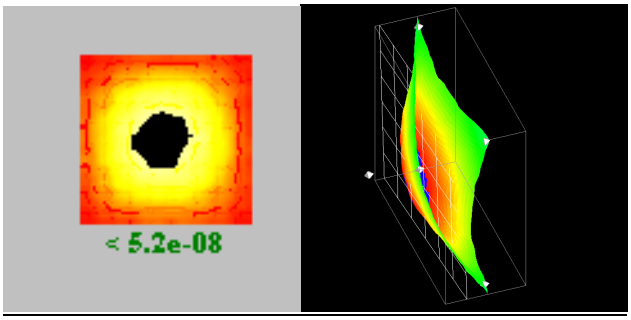

Figure 8.9 Images of the lid fringes during leak test.

8.4 Visual and SEM Examination

All attached components were visually inspected for defects such as inadequate solder flow. We reflowed indium solder at different oxygen levels using both the hot plate and the diode laser as the heating source. We were able to melt the solder at about its melting temperature of 156^{o}C in air but because of the oxide film formed on the solder, the solder remained in its cylindrical shape and did not wet the metallization. At oxygen levels below 250 ppm, the solder flows and wets the gold metallization. Figure 8.10a shows the top view of a carrier with attached optical fiber. Indium solder used for the attachment flowed through the side hole through which fiber is inserted to the MEMS die, as shown in Figure 8.10b. Figures 8.11 (a) and (b) are micrographs of the optical fiber-to-carrier joint at low and high magnifications (x86 and x1500) obtained from a scanning electron microscope. We did not detect interfacial delamination between either the carrier/solder or solder/fiber interfaces.

8.5 Conclusions

In this chapter, the results of the mechanical reliability tests for carrier-level and die level MOEMS were presented. The results obtained from the die-to-carrier and die-to-cap-chip shear and the fiber-to-carrier pull tests indicate adequate joint strengths in all cases, passing the MIL-STD standard. Hermetic package sealing was also an important reliability requirement for our MEMS switch. Carrier lid hermetic sealing was obtained using a combination of seam sealing and fluxless solder reflow. Measured package leak rates less than 5.2e-8 atm. cc/s, passing the MIL-STD leak test, were obtained using an optical leak tester.

Using process modeling, the relationship between process input parameters and output response was obtained using linear regression, showing that the bonding pressure is the most important process parameter affecting the bond strength. We also note that all joining processes presented in this dissertation were carried out without the use of flux or other organic compounds.

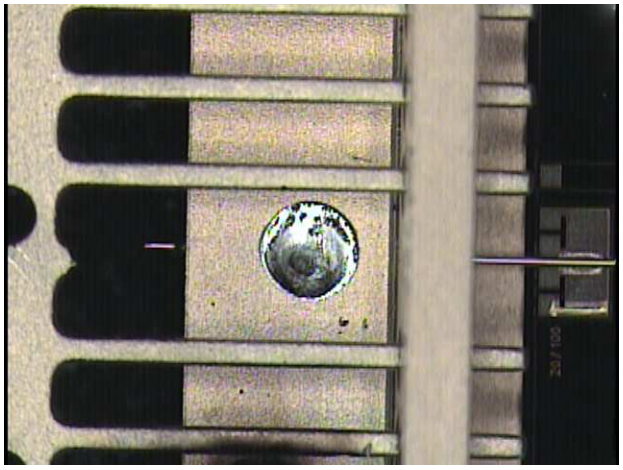

(a)

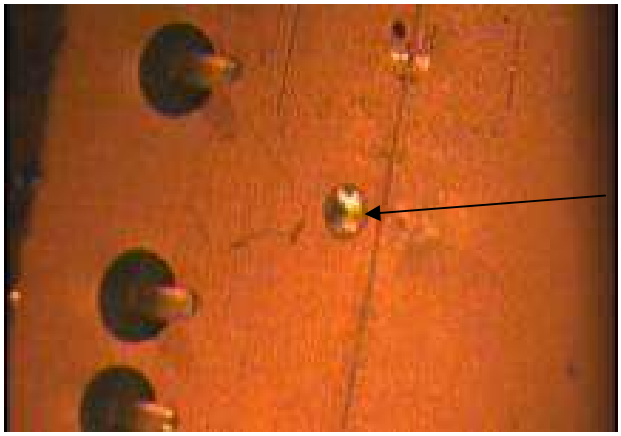

(b)

Figure 8.10 Indium solder flow in nitrogen gas environment
(a) top view (b) and side view.

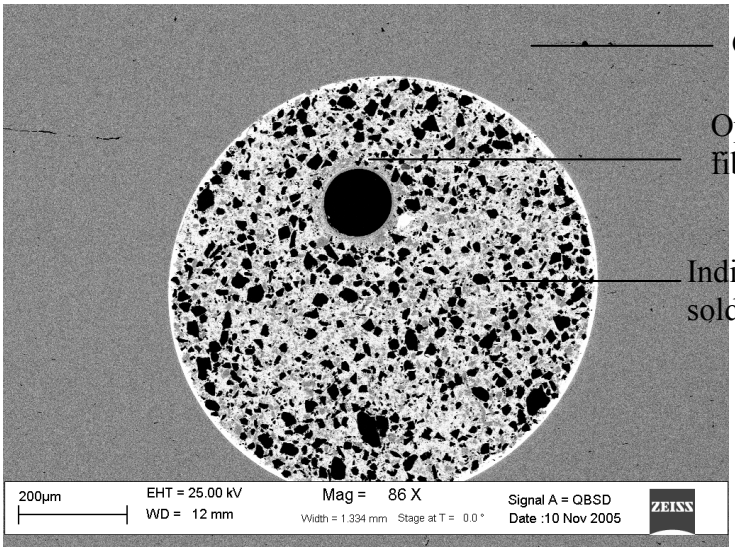

(a)

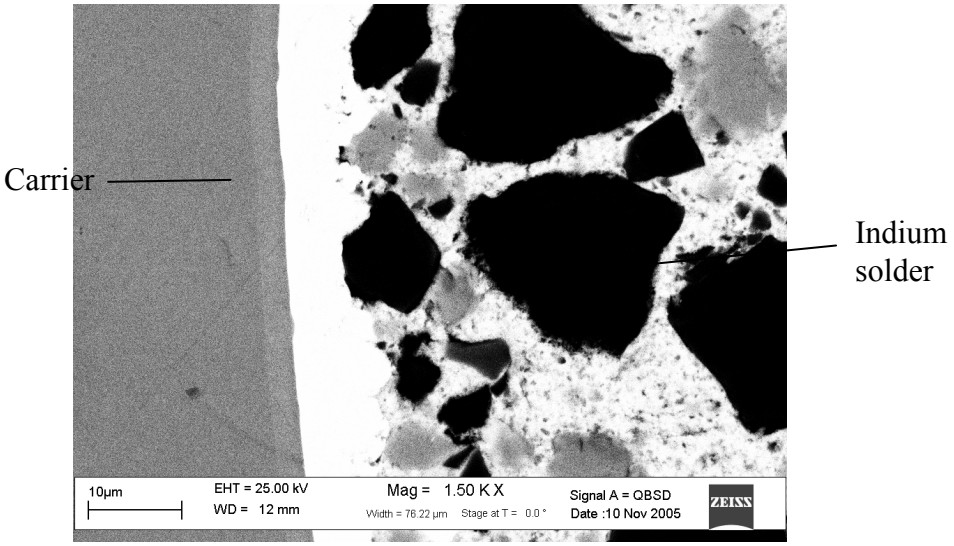

Figure 8.11 SEM micrographs of optical fiber-to-carrier joint at (a) x86 and (b) x1500 magnification.

CHAPTER 9

CONCLUSIONS AND FUTURE WORK

9.1 Summary and Conclusions

Carrier level and die level hermetic packaging solutions for optical MEMS switches have been presented. Electrical and optical interconnections are obtained via wire bonding, through-wafer vertical vias and optical fibers. A design for reliability *(DfR)* framework suitable for MEMS packaging was applied to find appropriate package designs, process windows, and evaluate preliminary package reliability. This framework is depicted in Figure 5.1, and in this dissertation, we have focused on verification of package design and reliability before the manufacture step. By applying *DfR* to MEMS packaging, reliability is considered a design factor in starting from the idea stage and throughout product life.

We showed via numerical simulations that carrier package temperature distribution may be enhanced through carrier redesign and surface property modifications. These modifications were described in section 7 and they consists of:

i. Thermally isolating laser heating areas so as to impede thermal diffusion within the carrier, and

ii. Modifying the surface property of the carrier so as to increase its thermal absorptivity within the operating wavelength range of the diode laser.

The results obtained from the die-to-carrier die shear and the fiber-to-carrier tests indicate adequate joint strengths in both cases, passing the MIL-STD standard destructive tests. Using process modeling, the relationship between process input parameters and output response for die level hermetic sealing was obtained using linear regression, showing that the bonding pressure is an important process parameter affecting the die bond strength. Die shear bond strengths up to 7.10 MPa were obtained. For the die-to-carrier die shear tests performed, bond strengths exceeding 13.8 MPa were obtained. The actual strength values could not be measured because the maximum load cell available for the test equipment was not sufficient to cause die shear. The shear values obtained for all shear tests meets the MIL-STD requirement of 2.5 kg.

Hermetic package sealing is also important for MEMS reliability. Carrier lid hermetic sealing was obtained using a combination of seam sealing and solder reflow for the carrier level MOEMS switch, and by solder reflow for the die level MOEMS switch. Measured package leak rates less than 5.2e-8 atm. cc/s, passing the MILSTD leak test, were obtained using an optical leak tester.

A fluxless fiber-to-carrier attachment process via laser soldering was also developed. Numerical simulation was used to determine laser power and heating duration requirements for the soldering operation. Additionally, we established experimentally that 99.999% indium solder requires inert gas environment which can be obtained using nitrogen gas with oxygen level less than 250 ppm for this operation. We observed that for the carrier level MOEMS switch packaging, the carrier geometry and surface property can be modified to improve package heat distribution near the solder

melting spots. We also observed that solder material cleaning using wet chemistry or plasma is necessary for indium solder flow. Adequate bond strengths (bond strength assessment was determined using fiber pull test) with mean strengths of 5.02 MPa was obtained.

Our DFR approach to MEMS packaging provides a basis for process development and MEMS packaging that maximizing development efforts and resources. This is accomplished by applying concurrent package design, simulation, and reliability testing at various stages of the packaging process. This approach is more suitable for MEMS packaging than IC packaging because of the low- to medium order requirement typical for MEMS. This makes it difficult to devote much resource to MEMS packaging process development.

This dissertation also presented data on *DfR* using a small number of experiments, leading to a package design and a process flow that can pass the MIL-STD acceptance tests. This approach is useful in cases where limited resources are devoted to process development such as MOEMS packaging.

We also discussed the use of numerical simulation in the packaging of an Implantable Drug Delivery System (IDDS) that includes an electrothermal microactuator. The IDDS requires multiple interconnection types (fluidic and electrical). It has to be bio-compatible with the host environment (human body) and should not dissipate too much heat to the surrounding environment. In particular, the requirements of this device for implantation include a temperature increase outside the package by no more than 4ºC. The device should dispense precise amount of

medication at expected times and there must be no leakages, hence the need for hermetic sealing. The packaged device must be small and not cause much discomfort to the user. As an aid for package design, we demonstrated the use of reduced-order lumped and FEA model approximations for multiphysics analysis involving multiple length scale structures. Our models are accurate to within 10% with one to two order of magnitude reductions in computational time. Simulation results show that packaging significantly affects the micropump flow rate, reducing it by a factor of 2.

9.2 Recommendations for Future Work

Certain aspects the proposed framework for applying DfR to MOEMS packaging were not carried out in this dissertation. We therefore propose that following work be performed in the future:

- Time dependent accelerated testing such as temperature cycling, vibration testing, creep testing, etc.
- Repeat experiments should be performed in order to obtain better error estimates.
- Characterizing the joint qualities in terms of the metallurgical bond formed between the solder and the substrate to determine what kinds of intermetallics are formed.
- Wire bond pull tests.
- Optimization based on parametric design of simulations studies will be carried out using the micropump's macro and micro-models.
- Experimental validation of micropump operation and packaging.

REFERENCES

[1] R. Bogue, “MEMS Sensors: Past, Present and Future,” Sensor Review, vol. 27, no 1, pp. 7-13, 2007.

[2] C. S. Smith, "Piezoresistance Effect in Germanium and Silicon," Phys. Rev., vol. 94, no. 1, pp. 42-49, 1954.

[3] Wikipedia, Internet: http://en.wikipedia.org/wiki/Piezoresistive_effect, Oct. 6, 2007 [Nov. 5 2007].

[4] B. Frazier, R. O. Warrington, and C. Friedrich, “The Miniaturization Technologies: Past, Present, and Future,” IEEE Transactions on Industrial Electronics, vol. 42, no. 5, pp 423-430 1995.

[5] N. Maluf, *An Introduction to Microelectromechanical Systems Engineering*. Norwood, MA: Artech House Publishers, 1999.

[6] C. Ho, and Y. Tai, “Microelectromechanical systems (MEMS) and Fluid Flows,” Annual Review of Fluid Mechanics, vol. 30, pp. 579-612, 1998.

[7] M. Mehregany, and C. A. Zorman, “SiC MEMS: opportunities and challenges for applications in harsh environments,” Thin Solid Films vol. 355-356, pp. 518-524, 1999.

[8] A. Neukermans, and R. Ramaswami, “MEMS Technology for Optical Networking Applications,” IEEE Communications Magazine, vol. 39, no. 1, pp. 62-69, 2001.

[9] S. D. Robinson, “MEMS Technology-Micromachines Enabling the “All Optical Network”,” Proc. Electronic Components and Technology Conf., Orlando, FL., pp. 423-428, 2001.

[10] S. M. Spearing, “Materials Issues in Microelectromechanical Systems (MEMS),” Acta Materialia, vol. 48, no. 1, pp. 179-196, 2000.

[11] A. B. Frazier, R. O. Warrington, and C. Friedrich, “The Miniaturization Technologies: Past, Present, and Future,” IEEE Transactions on Industrial Electronics, vol. 42, no. 5, pp. 423-430, 1995.

[12] J. Gau, E. H. Lan, B. Dunn, C. Ho, and J. C. S Woo, “A MEMS Based Amperometric Detector for E. Coli Bacteria using Self-assembled Monolayers,” Biosensors & Bioelectronics vol. 16, no. 9, pp. 745-755, 2001.

[13] B. A. Warneke, and K. S. J. Pester, “MEMS for Distributed Wireless Sensor Networks,” Proceedings of the 9th International Conference on Electronics, Circuits and Systems, Dubrovnik, Croatia, vol. 1, pp. 291-294, 2002.

[14] H. A. C. Tilmans, W. De Raedt, and E. Beyne, “MEMS for wireless communications: from RF-MEMS components to RF-MEMS-SiP,” J. Micromech. Microeng. Vol. 13, pp. 139-163, 2003.

[15] L. J. Hornbeck, “Digital Light Processing™ for High-Brightness, High-Resolution Applications,” Proc. SPIE Projection Displays III, Invited paper, vol. 3013, pp. 27-40, 1997.

[16] M. R. Douglass, “Lifetime Estimates and Unique Failure Mechanisms of the Digital Micromirror Device (DMD),” presented at the IEEE International Reliability Physics Symposium, 1998.

[17] L. Yoder, An introduction to the digital light processing (DLP) technology, 1997. Available:http://www.dlp.com/downloads/default.aspx?&ref=/downloads/white_papers/119_Intro_Digital_Light_Processing.pdf, [April 5, 2007]

[18] B. D. Staple, and J. Jakubczak, “The Impact of MEMS based Microsystems on US Defense Applications,” Available: http://www.osti.gov/bridge/servlets/purl/750328-AQBVQ9/webviewable/750328.pdf, [June 3, 2007].

[19] M. C. Wu, “Micromachining for Optical and Optoelectronic Systems,” Proceedings of the IEEE, vol. 85, no. 11, pp. 1833-1856, 1997.

[20] S. G. Kim, G. Barbastathis and H. L. Tuller, “MEMS for Optical Functionality,” Journal of Electroceramics, vol. 12, pp. 133-144, 2004.

[21] www.vigortechnology.com

[22] Research Horizons Magazine, “Measuring Up: CardioMEMS’ New Medical Device Combines Wireless and MEMS Technology to Monitor Blood Pressure of Aneurysm Patients,” Available: http://gtresearchnews.gatech.edu/newsrelease/endosure.htm, [Nov. 2, 2007]

[23] N. I. Maluf, D. A. Gee, K. E. Petersen, and G. T. A. Kovacs, “Medical Applications of MEMS,” IEEE WESCON Conference on Microelectronics Communications Technology Producing Quality Products Mobile and Portable Power Emerging Technologies, San Francisco, CA, USA, pp. 300-3.6, Nov 1995.

[24] The Aerospace Corporation, “Microengineering Aerospace Systems,” Available: http://www.aero.org/publications/helvajian/helvajian-3.html, April 14, 2006, [Nov. 3, 2007].

[25] T. Numazawa, K. Miura, K. Kawase, and Y. Hirata, “Development of a MEMS Optical Switch Composed of Ribbon-Like Actuator,” SEI Technical Review, n 56, June, 2003, p 37-40.

[26] Y. C. Lee, “Group Position Paper: MEMS Packaging and Reliability,” NSF 2000 Workshop on Manufacturing of MEMS, Orlando, Florida, November 7, 2000.

[27] T. Hsu, “Reliability in MEMS Packaging,” Proceedings of the 44th International Reliability Physics Symposium, pp. 398-402, 2006.

[28] R. Tummala, Fundamentals of Microsystems Packaging, New York: McGraw-Hill, 2001.

[29] www.ieee.org

[30] T. R. Moss, “The Reliability Data Handbook,” ASME Press: New York, 2005.

[31] K. Crow, DRM Associates, “Design for the Life Cycle,” Available: http://www.npd-solutions.com/lifecycle.html, [April 2, 2007].

[32] D. Crowe, and A. Feinberg, (Ed.), “Design for Reliability,” Boca Raton: CRC Press, 2001.

[33] Z. F. Wang, W. Cao, and Z. Lu, “MOEMS: packaging and testing,” Microsyst Technol., vol. 12, pp. 52–58, 2005.

[34] L. Liwei, “MEMS Post-Packaging by Localized Heating and Bonding,” IEEE Transactions on Advanced Packaging, vol. 23, pp. 608-616, 2000.

[35] M. Da Silva, “Standard Open Tool Packages for MEMS-enabled Products,” Advanced Packaging, vol. 13, no. 9, 2004.

[36] Y. C. Lee, B. A. Parviz, J. A. Chiou, and S. Chen, “Packaging for Microelectromechanical and Nanoelectromechanical Systems,” IEEE Transactions on Advanced Packaging,” vol. 26, no. 3 pp. 217-226, 2003.

[37] J. A. Walker, “The future of MEMS in Telecommunications Networks,” J. Micromech. Microeng. Vol. 10**,** pp. R1-R7, 2000.

[38] R. Ramesham and R. Ghaffarian, “Challenges in interconnection and packaging of microelectromechanical systems (MEMS),” Proceedings of Electronic Components and Technology Conference, pp. 666-675, 2000.

[39] P. V. Dressendorfer, D. A. Peterson and C. A. Reber, "MEMS Packaging – Current Issues and Approaches," International Conference on High Density Interconnect and Systems Packaging, Denver, CO, pp. 208-213, April 2000.

[40] K. Gilleo, “MEMS Packaging Issues and Materials,” 2000 IMAPS International Symposium on Microelectronics, pp 598-604, 2000.

[41] M. Datta, T. Ōsaka, and J. W. Schultze, Microelectronic Packaging, CRC Press, 2004

[42] T. Hsu, MEMS & Microsystems: Design and Manufacture, 1st Edition, New York, USA: McGraw-Hill, pp. 391, 2002.

[43] C. T Hsieh, J. M. Ting, C. Yang, and C. K. Chung, “The Introduction of MEMS Packaging Technology,” IEEE International Symposium on Electronics Materials and Packaging, pp. 300-306, 2002.

[44] M. Mignardi, “From ICs to DMDs,” TI Tech. Journal, pp. 56 – 63, July - Sept. 1998.

[45] Y. L. Low, R. E. Scotti, D. A. Ramsey, C. A. Bolle, S. P. O’Neill and K. C. Nguyen, “Packaging of Optical MEMS Devices,” Journal of Electronic Packaging, vol. 125, September 2003.

[46] K. Gilleo, “MEMS Packaging Issues and Materials,” 2000 IMAPS International Symposium on Microelectronics, pp 598-604, September 2000.

[47] K. Gilleo, M. Witt, D. Blumel and P. Ongley, “Towards a better understanding of underfill encapsulation for flip chip technology: proposed developments for the future,” Microelectronics International, vol. 16, no. 2, pp. 39-43, 1999.

[48] C. P. Wong, S. H. Shi and G. Jefferson, “High Performance No-Flow Underfills for Low-Cost Flip-Chip Applications: Material Characterization,” IEEE Transactions on Components, Packaging, and Manufacturing Technology—Part A, vol. 21, no. 3, pp. 450-458, 1998.

[49] T. Y. Wu, Y. Tsukada and W. T. Chen, “Materials and Mechanics Issues in Flip-Chip Organic Packaging,” Electronic Components and Technology Conference, pp. 524-534, 1996.

[50] HCC Industries, Metal Platform Plug-Ins, Available: http://www.hccindustries.com/products/microelectronic-packages/metal-platforms/default.asp, [Sept. 28, 2007].

[51] K. Gilleo, “MEMS/MOEMS Packaging: Concepts, Designs, Materials, and Processes,” McGraw-Hill: New York, pp.77, 2005.

[52] K. Gilleo, “MEMS/MOEMS Packaging: Concepts, Designs, Materials, and Processes,” McGraw-Hill: New York, pp.86-90, 2005.

[53] Amkor® Technology, “Hermetic Packaging Services,” Available: http://www.amkor.com/products/all_datasheets/flatpack.pdf and http://www.amkor.com/products/all_datasheets/CBGA.pdf, Aug. 2002, [Nov. 7, 2007].

[54] K. Gilleo, “MEMS/MOEMS Packaging: Concepts, Designs, Materials, and Processes,” McGraw-Hill: New York, pp.90, 2005.

[55] Amkor® Technology, “Packaging the Micro-machine,” Available: http://www.amkor.com/products/notes_papers/Micro-machine3.PDF, [Sept. 12, 2007].

[56] T. Hsu, “MEMS & Microsystems Design and Manufacture,” McGraw-Hill: New York, pp. 411-414, 2002.

[57] I. W. Qin, “Wire Bonding Tutorial,” Advanced Packaging, vol. 14, no. 7, July 2005.

[58] L. Liwei, “MEMS Post-Packaging by Localized Heating and Bonding,” *IEEE Transactions on Advanced Packaging,* vol 23, pp. 608-616, November 2000

[59] R. Ramesham and R. Ghaffarian, “Challenges in Interconnection and Packaging of Microelectromechanical Systems (MEMS),” *Electronic Components and Technology Conference,* 2000 Proceedings, pp 666 – 675, May 2000.

[60] M. Finot et al, “Automated Optical Packaging Technology for 10 Gb/s Transceivers and its Application to a Low-Cost Full C-Band Tunable Transmitter,” *Intel Technology Journal,* vol 8, Issue 2, 2004.

[61] K. Gilleo, "MEMS Packaging Solutions," *Electronic Packaging & Production,* pp. 49-50, 52-56, June 2000.

[62] K. Gilleo, "MEMS Packaging Issues and Materials," *2000 IMAPS International Symposium on Microelectronics,* pp 598-604, September 2000.

[63] J. W. Soucy, J. F. Haley, and T. F. Marinis, "An Approach to MEMS Sensor Array Packaging," *2000 IMAPS International Symposium on Microelectronics,* pp 768-771, September 2000.

[64] R. Tummala, Fundamentals of Microsystems Packaging, New York: McGraw-Hill Publishers, 2001.

[65] N. Koopman, S. Bobbio and J. Bousaba, "Fluxless soldering in air and nitrogen," *Electronic Components and Technology Conference*, 1993. Proceedings, pp 595 – 605, 1-4 June 1993..

[66] M. Deeds, "Qualification of Metallized Optical Fiber Connections for Chip-Level MEMS Packaging," Ph.D Thesis, University of Maryland, College Park, 2004.

[67] F. M. Hosking, "Reduction Of Solvent Use Through Fluxless Soldering," Proceedings/Compendium of Papers Solvent Substitution Based on The First Annual International Workshop on Solvent Substitution December 4-7, 1990.

[68] B. E. Noltingk and E. A. Neppiras, "Ultrasonic soldering irons," J. Sci. Instrum. vol. 28, no 2, 50-52.

[69] Z. Sun, D. Pan, J. Wei, and C. K. Wong, "Ceramics Bonding Using Solder Glass Frit." *Journal of Electronic Materials,* vol. 33, no. 12, 2004.

[70] MACOR® Technical Bulletin - Sealing with Macor Machinable Glass Ceramic

[71] MACOR® Technical Data Sheet - "Machinable Glass Ceramics." Morgan Advanced Ceramics, 2002.

[72] H. Hanko, Soldering Handbook for Printed Circuits and Surface Mounting, Massachusetts: Kluwer Academic Publishers, 1995.

[73] K. G. Frase, and D. E. Seeger, Preface in IBM J. Res. & Dev. Vol.49, issue 4/5, pp 606, 2005.

[74] B. Gogoi, M. Vujosevic, and S. Petrovic, "Challenges in Packaging for MEMS devices," Proceedings of 2000 SMTA International.

[75] K. Gilleo, "MEMS/MOEMS Packaging: Concepts, Designs, Materials, and Processes," McGraw-Hill: New York, 2005.

[76] R. Guerre, F. Fahrni, and P. Renaud, "Fast 10-μs Microelectromechanical Optical Switch Inside a Planar Hollow Waveguide (PHW)," J. of Lightwave Technology, vol. 24, no. 3, March 2006.

[77] T. Numazawa, K. Miura, K. Kawase and Y. Hirata, "Development of a MEMS Optical Switch Composed of Ribbon-Like Actuator," SEI Technical Review Number 56, June 2003.

[78] S. Kim, G. Barbastathis, and H. L. Tuller, "MEMS for Optical Functionality," Journal of Electroceramics, vol. 12, pp. 133–144, 2004.

[79] B. H. Stark and K. Najafi, "A Low-Temperature Thin-Film Electroplated Metal Vacuum Package," Journal of Microelectromechanical Systems, vol. 13, no. 2, 2004.

[80] C. T.-C. Nguyen and R. T. Howe, “Quality factor control for micromechanical resonators,” Technical Digest, IEEE International Electron Devices Meeting, San Francisco, California, December 14-16, pp. 505-508, 1992.

[81] F. Ayazi and K. Najafi, “A HARPSS polysilicon vibrating ring gyroscope,” J. Microelectromech. Syst., vol. 10, no. 2 pp. 169–179, 2001.

[82] M. Abe, E. Shinohara, K. Hasegawa, S. Murata, and M. Esashi, “Trident-type tuning fork silicon gyroscope by the phase difference detection,” in Proc. 13th IEEE International Conference on Microelectromechanical Systems, Miyazaki, Japan, pp. 508–513, 2000.

[83] B.-L. Lee, C.-H. Oh, S. Lee, Y.-S. Oh, and K.-J. Chun, “Vacuum packaged differential resonant accelerometer using gap sensitive electrostatic stiffness changing effect,” in Proc. 13th IEEE International Conference on Microelectromechanical Systems, Miyazaki, Japan, pp. 352–357, 2000.

[84] H. van Heeren, “Evolution and trends in high volume production of MEMS,” Available: http://www.enablingmnt.com/MEMS_sensors_evolution_and_trends_-_Henne_van_Heeren_Jan2007.pdf, [Nov. 20, 2007].

[85] S. M. Spearing, “Materials Issues in Microelectromechanical Systems (MEMS),” Acta Mater. Vol. 48 pp. 179-196, 2000.

[86] T. Hsu, MEMS & Microsystems: Design and Manufacture, 1st Edition, McGraw-Hill, New York, USA, p 310, 2002.

[87] T. Hsu, MEMS & Microsystems: Design and Manufacture, 1st Edition, McGraw-Hill, New York, USA, pp. 301-303, 2002.

[88] MEMS and Nanotechnology Clearinghouse, "Etching Processes," Available: http://www.memsnet.org/mems/processes/etch.html, [April 20, 2007].

[89] G. S. May and C. J. Spanos, "Fundamentals of Semiconductor Manufacturing and Process Control," New Jersey: John Wiley & Sons, 2006

[90] Wikipedia, "Manufacturing," Available: http://en.wikipedia.org/wiki/Manufacturing, [April 20, 2007].

[91] Infrastructure, "The Chip-Making Process, Available: http://www.infras.com/Tutorial/sld001.htm, [Nov. 20, 2007].

[92] National Institute of Standards and Technology, Available: http://www.itl.nist.gov/div898/software/dataplot/refman1/auxillar/gif/ewma.gif, [April 20, 2007].

[93] L. W. Condra, Reliability Improvement with Design of Experiments, 2nd ed., New York: Marcel Dekker, Inc., 2001.

[94] D. C. Montgomery, J. B. Keats, L. A. Perry, J. R. Thompson and W. S. Messina, "Using Statistically Designed Experiments for Process Development and Improvement: An Application in Electronics Manufacturing," Robotics and Computer Integrated Manufacturing vol. 16, pp. 55-63, 2000.

[95] D. C. Montgomery, "Design and Analysis of Experiments," 6th ed., Wiley Publishers, 2005.

[96] C. Daniel, "Use of Half-normal plots in interpreting factorial two-level experiments," Technometrics vol. 1, pp. 311-341, 1959.

[97] R. V. Lenth, “Quick and Easy Analysis of Unreplicated Factorials,” Technometrics, vol. 31, no. 4, pp. 469-473, 1989.

[98] M. Hamada and N. Balakrishnan, “Analyzing Unreplicated Factorial Experiments: A Review With Some New Proposals,” Statistica Sinica vol. 8, pp. 1-41, 1998.

[99] S. Brown, “A little Knowledge,” Mech Eng., October 2003

[100] K. Gilleo, “MEMS/MOEMS Packaging: Concepts, Designs, Materials, and Processes,” New York: McGraw-Hill, pp.153, 2005.

[101] A.B. Sontheimer, “Digital Micromirror Device (DMD) Hinge Memory Lifetime Reliability Modeling”, 2002 IEEE International Reliabiliy Physics Symposium Proceedings, pp. 1 18-121, 2002.

[102] B.D. Jensen, J.L. Volakis, K. Saitou, K., Kurabayashi, “Impact of skin effect on thermal behavior of RF-MEMS switches,” 6th ASME-JSME Thermal Engineering Joint Conference, 2003.

[103] R. Modlinski, et. al, “Creep as a reliability problem in MEMS,” Microelectronics Reliability, vol. 44, pp 1733-1738, 2002.

[104] R. Modlinski et al. “Creep characterization of Al alloy thin films for use in MEMS applications,” Microelectronic Engineering vol. 76, pp. 272–278, 2004.

[105] R. Modlinski, P. Ratchev, A. Witvrouw, R. Puers and I. DeWolf, “Creep-resistant aluminum alloys for use in MEMS,” J. Micromech. Microeng. Vol. 15, no. S165–S170, 2005.

[106] R. Feynman, “There’s plenty of room at the bottom,” J. Microelectromech. Syst. Vol. 1, pp. 60-66, 1992.

[107] Military Standard 883F

[108] M. W. Beranek, M. Rassaian, C.-H. Tang, C. L. St. John, and V. A. Loebs, "Characterization of 63Sn37Pb and 80Au20Sn Solder Sealed Optical Fiber Feedthroughs Subjected to Repetitive Thermal Cycling," IEEE Transactions on Advanced Packaging, vol. 24, no. 4, November 2001.

[109] D. R. Olsen and H. M. Berg, "Properties of Die Bond Alloys Relating to Thermal Fatigue," lEEE Transactions on Components,Hybrids,and Manufacturing Technology, vol. CHMT-2, no. 2, pp. 257-263, June 1979.

[110] K. R. Cochran, L. Fan, and D. L. DeVoe, "High-power optical microswitch based on direct fiber actuation," Sensors and Actuators A: Physical, vol. 119, Issue 2, pp 512-519, 2005.

[111] J. Li , Q. X. Zhang, and A. Q. Liu, "Advanced fiber optical switches using deep RIE (DRIE) fabrication," Sensors and Actuators A: vol. 102, Issue 3, pp 286-295, 2003.

[112] K. Rebak and M. Shaikh, Statistical Design of Experiments with Engineering Applications, Boca Raton, Florida, CRC Press, 2005.

[113] L. Wood, C. Fairfield, and K. Wang, "Plasma Cleaning of Chip Scale Packages for Improvement of Wire Bond Strength," 2000 Int'l. Symp. on Electronic Materials & Packaging, pp 406-408, 2000.

[114] A. Kole, J. Sin, W. H. Lee, D. O. Popa, D. Agonafer, and H. Stephanou, "Design of polymer tube embedded in-plane micropump," in Proc. of Thermal and Thermomechanical Phenomena in Electronics Systems, 2006. ITHERM '06. pp. 1324 – 1329, 2006.

[115] A. Kole, J. Sin, W. H. Lee, D. Popa, D. Agonafer, and H. Stephanou, " Polymer tube embedded in-plane micropump for low flow rate," Digital Avionics Systems Conference, vol. 2, 2005.

[116] J. Sin, W. H. Lee, and H. E. Stephanou, "In-plane micropump: design optimization," in Technical proceedings of the 2004 NSTI Nanotechnology conference and Trade show, vol. 1, 2004.

[117] S. M. N. Rao, S. Karajgikar, A. Fasoro and D. O. Popa, "Implantable Drug Delivery Mcropump," ARRI-UTA Report, December 2007.

[118] S. Paruchuri, "Flexible Microfluidic Circuit with Embedded In-Plane Valve." MS Thesis, The University of Texas at Arlington, 2007.

[119] A. Kole, "Polymer tube embedded in-plane micropump: Design, analysis and fabrication," MS Thesis, The University of Texas at Arlington, 2005.

[120] M. Greenstein, "Optical Absorption Aspects of Laser Soldering for High Density Interconnects," Applied Optics, Vol. 28, No. 21, 2000.

[121] K. Kurpisz and A. J. Nowak, Inverse Thermal Problems. Southampton, UK: Computational Mechanics Publications, 1995.

[122] M. N Ozisik and H. Orlande, Inverse Heat Transfer. New York: Taylor & Francis, 2000.

[123] http://www.matweb.com

[124] H. Machiraju, B. Infantolino, B. Sammakia, and M. Deeds, "Thermal Analysis of MEMS Microactator Performance," 2007 ASME International Mechanical Engineering Congress and Exposition, November 11-15, 2007, Seattle, Washington, USA.

[125] S.M. Rao, A. Mhatre, D. O. Popa, J.-C. Chiao, T. Ativanichayaphong, J. Sin, and H.E. Stephanou, "MEMS based Implantable Drug Delivery System," in Proc. of TEXMEMS VII, El Paso, Texas, USA, 2005.

[126] A Mhatre, "Implantable Drug Delivery System With an In-Plane Micropump." MS Thesis, The University of Texas at Arlington, 2005.

BIOGRAPHICAL INFORMATION

Abiodun (Abbey) was born in Ibadan, the largest indigenous city in Africa, south of the Sahara to Pa Timothy Adewale and Madam Monilola Olatoun Fasoro of the Olawole Compound, Oke-Oja, Iloro, Igbajo, Nigeria in 1969. In 1986, he became a freshman in Mechanical Engineering, Obafemi Awolowo University (formerly University of Ife), Nigeria. He graduated with a MS degree from the University of Lagos in 1996 and in 1997, he started his Master of Philosophy degree program at the School of Metallurgy & Materials, Interdisciplinary Research Center (IRC) of the University of Birmingham, UK. At Birmingham, he worked under the advisement of John Campbell. John is considered the originator of the cosworth casting process. At Birmingham, he researched into the effects of the lustrous carbon defects in grey cast iron. He graduated from Birmingham in 2000.

Abbey started his Ph D. program in Mechanical Engineering in the Spring of 2003 at the University of Texas, Arlington, TX and has been working at the Automation & Robotics Research Institute (ARRI) since Fall of 2004. At ARRI, Abbey worked on several government and industry funded projects in the areas of MEMS and MOEMS packaging, reliability, and process development.